Uncovering design rules in small-molecule organic semiconductors

By

Makena Austin Dettmann

Dissertation

Submitted in partial satisfaction of the requirements for the degree of

Doctor of Philosophy

in

Materials Science and Engineering

in the

Office of Graduate Studies

of the

University of California

Davis

Approved:

Adam Moulé, Chair

Tonya Kuhl

Ambarish Kulkarni

Committee in Charge

2022

To my partner Katie. For being by my side through it all.

Contents

List of Figures

List of Tables

Abstract

Uncovering design rules in small-molecule organic semiconductors

Organic semiconductors have the potential to create flexible, transparent electronic devices. Unfortunately, these materials suffer from low mobilities because atomic vibrations, known as phonons, localize charge carriers. In order to improve mobility in these materials, it is essential to understand which types of phonons are present and how they affect charge transport. Inelastic neutron scattering (INS) can measure these motions directly, but the results cannot be interpreted without computing the phonon modes from an experimental structure. These calculations typically rely on density functional theory (DFT) which is highly accurate but computationally costly. This limits calculations to highly-ordered small molecules. To try and push past these limits, we used six different computational methods to compute the phonon modes ranging from DFT to molecular dynamics (MD) and machine learning (ML). We find that while nothing can compete with DFT, density functional tight binding (DFTB) and DFTB with a machine learning component produce decent results at a fraction of the cost. Then, we apply INS along with our optimized DFT-based method to a metal-organic framework (MOF) system. These MOFs are known to have defects that play an important role in their catalytic activity, but characterizing these defects remains an ongoing challenge. By measuring the phonons with INS and simulating them with DFT, we are able to identify peaks that correspond to defects in the MOF. By using a variety of structures, we are able to identify the structure of the MOF along with the types of defects present. Finally, we develop a novel workflow, ElPh, which allows us to couple our phonon calculations to the electronic structure in small-molecule organic semiconductors. This allows us to understand how all of the phonons work together to limit charge mobility. In addition, we developed a novel analysis technique that shows how each atom limits charge transport. This novel approach allows us to discover design rules for the first time–making meaningful progress toward designing new, high-performance materials.

Acknowledgments

I would like to thank those who helped me throughout my fulfilling and challenging journey of completing my dissertation. First, I'd like to thank my family–Shawn, Detra, and Hannah Dettmann who supported me throughout with helpful guidance and advice. I would also like to thank my great-uncle and great-aunt Ted and LaVaughn Craig, who were unfailingly supportive during these years. I would like to thank my colleagues, especially Daniel Vong, Meghna Jha, and Lucas Cavalcante, who provided many helpful discussions and often lightened my mood during stressful periods. I would like to thank my undergraduate researchers, particularly Corina Magdaleno and Karina Masalkovaité, who were endlessly curious and helpful. Acting as a mentor for them was one of the highlights of my dissertation. I would like to thank my boss and mentor, Adam Moulé, for many helpful discussions and guidance throughout my dissertation process. Adam often stopped by the office unannounced, and our conversations on those unplanned afternoons were some of the most insightful and helpful. Finally, I'd like to thank my partner, Katie Gerhart, who has made this whole endeavor much easier. She moved across the country with me and her support have made the hard times easier and the good times better.

Chapter 1

Introduction

1.1 Preamble

My dissertation contains three publications that I co-authored. Each publication uses quantum calculations to predict phonon modes in organic semiconductors and works toward the discovery of design rules for these materials. This section will serve as a general introduction to organic semiconductors and each paper will include a more specific introduction to the material of the paper.

1.2 Introduction

Organic semiconductors (OSC) have advantageous properties such as flexibility and transparency which make them useful for unique applications such as wearable sensors or flexible solar panels [1–5]. OSCs occur when alternating double and single bonded carbon chains are formed. These chains form π bonds which allow charges to delocalize along the chain [6]. OSCs typically fall into two groups: polymers and small molecules. While polymers are of great interest in experimental research, their large size and semi-crystallinity make them exceedingly difficult to model accurately. For this reason, small-molecule OSCs are typically studied using theoretical and computational techniques. Unfortunately, OSCs also suffer from low charge mobilities resulting from vibrations called phonons [7–11]. These phonons lower mobility by transiently reducing coupling between nearest-neighbor molecules. Although the synthetic design space for these materials is

enormous, design rules for high-mobility materials remain elusive [9, 11–13].

To compute the phonon modes, an experimental structure is determined from x-ray diffraction (XRD). In XRD, x-rays diffract off of atoms and interfere constructively from repeated units. Thus, XRD is able to measure the average atomic positions in a sample, but because XRD only yields average positions, defects cannot be identified. These positions must be relaxed to the lowest-energy positions. This minimization step is essential to compute the forces. This is done with gradient descent in which the gradient of the potential energy is followed down until the potential energy is minimized. During this step, periodic boundary conditions are employed, which make it possible to simulate an infinite repeating lattice with only the atoms in the unit cell. This also means that only perfectly crystalline models can be used.

Although a method for relaxing is described above, the method for computing the energies and forces is not detailed. There are several ways to compute energies and forces in a modeled system. The most accurate way is to solve the all-electron wavefunction. Unfortunately, this is so computationally demanding that it is impossible for any practical materials [14]. By making a series of assumptions and simplifications, it is possible to cut the computational requirements at the expense of accuracy. A good place to land in terms of expense vs accuracy for these materials is Density Functional Theory (DFT) because it maintains a high level of accuracy with computational requirements within the reach of modern supercomputers [15]. DFT makes the assumption that the all-electron wavefunction can be substituted with a wavefunction based on the electron density [16]. Chapter 2 describes DFT in more detail and explores why it is a good choice for these materials.

Once a relaxed structure is obtained, a finite displacement method is performed. The finite displacement method is equivalent to the finite difference method from basic calculus applied to multiple dimensions. Each atom is moved individually a small amount, typically 0.05 Å, in the positive and negative x, y, and z directions. This gives the force constant on each atom in each direction. Taking the Fourier transform yields the dynamical matrix. The dynamical matrix can be used to compute the atomic displacements and energies

which make up the phonon modes. A supercell is used at this stage if the system is too small to avoid self-interaction. In essence, if a model is used in which one side of the unit cell is smaller than the interaction cutoff, an atom will experience a force as a consequence of its own displacement. Thus, the model must be duplicated in that direction until the model size is longer than the interaction cutoff.

The transfer integral describes how much the wavefunctions of two molecules overlaps. This is directly related to the probability of charge hopping between the molecules [17]. To assess how the phonon modes change the transfer integral, the gradient must be computed. The gradient tells how a change in location for each atom affects the transfer integral. A similar finite displacement technique can be used to compute the gradient of the transfer integral. It is then possible to project each phonon mode onto the gradient and compute the impact of the phonon mode on charge transport. In simpler terms, the phonons describe how the atoms in the material move and the gradient of the transfer integral describes how a motion affects nearest-neighbor coupling. Combining the two explains how each atom in each phonon limits charge mobility.

It is possible to predict phonons and their impact on charge transport, but how do we know that the predictions are correct? These predictions must be validated to experimental data to ensure they are correct. Phonons range in energy from 5-3500 cm^{-1}, which limits the types of techniques that can be used to measure them [18]. Raman spectroscopy and infrared spectroscopy can cover part of this energy range and are readily available. However, both have selection rules which limit which phonons are visible. Moreover, they only measure phonons at the gamma point. To be as rigorous as possible, every mode should be measured, ensuring that every mode is correctly predicted.

Inelastic neutron scattering (INS) can measure phonons without the limitations described above. Neutrons interact with the nuclei of atoms, unlike photons, which interact with the electrons. The amount of interaction between a neutron and a particular atom type in a scattering event is the neutron scattering cross-section. In organic semiconductors, Hydrogen has the largest neutron scattering cross-section of 80 Barns [19]. The next closest is Carbon with a neutron scattering cross-section of 6 Barns [19]. As a result,

INS mostly measures the Hydrogen contributions to the phonon modes.

INS works by firing low-energy, or thermal, neutrons at a sample. When neutrons hit the sample, they exchange energy and/or momentum with the nuclei of atoms in the sample. These nuclei can only exchange energy and momentum if the momentum/energy combination is exactly consistent with a phonon mode allowed by the molecular structure [18]. This means that INS measures the phonon modes directly and gives a cross-section-weighted density of states for the phonon modes. Additionally, INS has several advantages over other techniques. First, INS is free from selection rules because it interacts directly with the nuclei. This means that every mode is measured across the entire Brillouin zone. Second, INS is penetrating, while photon-based techniques are not. Because light scatters so strongly from the electron clouds of atoms, photon-based techniques can only probe the first few atomic layers of a sample. In contrast, neutrons can penetrate deeply and are naturally weighted to measure bulk properties. Finally, INS can cover the entire region of interest for phonon modes (8-8000 cm^{-1}), while photon-based techniques struggle to measure phonons below 400 cm^{-1} [18]. In all, INS is the best option for measuring phonon modes in OSCs and is the best validation for predicted modes.

The work described in chapter 2 came from an attempt to extend standard theoretical techniques described above to larger, more complex systems such as polymers. In the chapter, I compare DFT to five other methods for predicting phonons in a small molecule OSC called rubrene. These methods range from quantum methods to machine learning methods and a classical molecular dynamics method. I also study the impact of training several methods to DFT. In the end, I find that a tight-binding approximation on DFT is the only method which can come close to the accuracy of DFT. We also find that we can improve this prediction with machine learning.

In chapter 3, we apply our DFT-based approach to a metal organic framework (MOF) called UiO-66. These MOFs are made up of metal clusters and organic linkers. They form cages which can hold small clusters of metal atoms which are highly reactive. For this reason, MOFs are studied primarily for catalytical applications. MOFs are known to have defects which affect the catalytic performance. However, these defects are often difficult to

characterize because MOFs are fragile and most techniques destroy them. In this paper, INS was used to probe the phonon modes present in a sample of UiO-66. When modeling a pristine structure of UiO-66, we accurately reproduced the entire spectrum except for a series of peaks at low energy. These peaks, therefore, must correspond to defects in the system. We then prepared a library of potential defect structures and computed the INS spectrum for each defect structure. By comparing the predicted spectrum to the experimental spectrum, we were able to determine which defects were present in the sample.

In chapter 4, I introduce a novel workflow, ElPh, and a new visual analysis technique for the discover of design rules in small-molecule OSCs. ElPh makes it possible to compute the electron-phonon coupling for a given material. The electron-phonon coupling describes the effect each phonon has on the coupling between adjacent molecules. The electron-phonon coupling contains all the information necessary to design better OSCs. The only problem is that the electron-phonon coupling contains the contribution of each atom in each mode. Since there are $3N-6$ phonon modes and N atoms, we find $(3N-6)\times N$ interactions. Since each phonon mode varies with crystal momentum, these modes are often sampled in q-space. I typically sample using an $8\times8\times8$ mesh, which means there are $(3N-6)\times N\times(N_q)^3$ pieces of information. For even a small system with 100 atoms there are 15,052,800 pieces of information which make up the electron-phonon coupling. Thus, it is impossible to extract design rules without reducing the information to something simpler. I do this by summing every contribution to the electron-phonon coupling for each atom. Thus, I have reduced the data to only 100 pieces of information for a system with 100 atoms. Now, it is possible to plot each molecule as a heatmap where the heat of the atom corresponds with the sum of the electron-phonon coupling contribution for that atom. Thus, this novel technique makes it possible to visualize which parts of a molecule limit mobility and therefore which parts should be focused on to improve.

Finally, chapter 5 includes work I've done that was not published elsewhere. This includes software I wrote to help clean an analyze atomic force microscopy (AFM) images, a slew of TTF-TCNQ results, and methods development around isolating the atomic

contributions to INS spectra. Additionally, I'll detail how I created DCS Discover, our open-source repo containing our predicted and measured INS spectra.

Bibliography

(1) Crabtree, G.; Glotzer, S.; McCurdy, B.; Roberto, J. *Computational materials science and chemistry: accelerating discovery and innovation through simulation-based engineering and science*; tech. rep.; USDOE Office of Science (SC)(United States), 2010.

(2) Walzer, K.; Maennig, B.; Pfeiffer, M.; Leo, K. *Chemical reviews* **2007**, *107*, 1233–1271.

(3) Wang, C.; Dong, H.; Jiang, L.; Hu, W. *Chemical Society Reviews* **2018**, *47*, 422–500.

(4) Zhang, X.; Dong, H.; Hu, W. *Advanced Materials* **2018**, *30*, 1801048.

(5) Kuribara, K.; Wang, H.; Uchiyama, N.; Fukuda, K.; Yokota, T.; Zschieschang, U.; Jaye, C.; Fischer, D.; Klauk, H.; Yamamoto, T., et al. *Nature communications* **2012**, *3*, 1–7.

(6) Jaiswal, M.; Menon, R. *Polymer international* **2006**, *55*, 1371–1384.

(7) Ciuchi, S.; Fratini, S.; Mayou, D. *Physical Review B* **2011**, *83*, 081202.

(8) Fratini, S.; Mayou, D.; Ciuchi, S. *Adv. Funct. Mater.* **2016**, *26*, 2292–2315.

(9) Harrelson, T. F. et al. *Mater. Horiz.* **2019**, *6*, 182–191.

(10) Schweicher, G.; Avino, G. D.; Ruggiero, M. T.; Harkin, D. J.; Venkateshvaran, D.; Liu, G.; Richard, A.; Ruzié, C.; Kennedy, A. R.; Shankland, K.; Takimiya, K.; Geerts, Y. H.; Axel, J.; Fratini, S.; Sirringhaus, H. *Adv. Mater.* **2019**, *31*, 1902407.

(11) Nematiaram, T.; Padula, D.; Landi, A.; Troisi, A. *Advanced Functional Materials* **2020**, *30*, 2001906.

(12) Vong, D.; Nematiaram, T.; Dettmann, M. A.; Murrey, T. L.; Cavalcante, L. S.; Gurses, S. M.; Radhakrishnan, D.; Daemen, L. L.; Anthony, J. E.; Koski, K. J., et al. *The Journal of Physical Chemistry Letters* **2022**, *13*, 5530–5537.

(13) Nematiaram, T.; Troisi, A. *Materials Horizons* **2020**, *7*, 2922–2928.

(14) Szabo, A.; Ostlund, N. S., *Modern quantum chemistry: introduction to advanced electronic structure theory*; Courier Corporation: 2012.

(15) Kohn, W.; Sham, L. J. *Physical review* **1965**, *140*, A1133.

(16) Hohenberg, P.; Kohn, W. *Physical review* **1964**, *136*, B864.

(17) Marcus, R. A.; Sutin, N. *Biochimica et Biophysica Acta (BBA)-Reviews on Bioenergetics* **1985**, *811*, 265–322.

(18) Philip, C. H. (; Parker, S. F.; Ramirez-Cuesta, A. J.; Tomkinson, J., *Vibrational spectroscopy with neutrons: With applications in chemistry, biology, materials science and catalysis*; World Scientific Publishing Co.: 2005, pp 1–642.

(19) Sears, V. F. *Thermal-neutron scattering lengths and cross sections for condensed-matter research*; tech. rep.; Atomic Energy of Canada Ltd., 1984.

Chapter 2

Comparing the expense and accuracy of methods to simulate atomic vibrations in rubrene

2.1 Acknowledgement

Lucas Cavalcante and Nir Goldman helped with the DFTB / ChIMES calculations. Luke Daemen is the instrument scientist at Oak Ridge National Lab who collected the INS data for us. Corina Magdaleno, Karina Masalkovaité helped with the DFTB and DFTB / ChIMES calculations. Daniel Vong helped with the DFT calculations. Jordan Dull and Barry Rand produced the Rubrene sample for us. Roland Faller helped with the MD simulations and Adam Moulé was the PI in charge of the project.

2.2 Introduction

Atomic vibrations, or phonons, affect material properties across several fields of scientific research. Improving predictions of phonon modes in complex atomic environments would have major impacts across disciplines.[1] In particular, accurate predictions of phonon modes would significantly improve our understanding of organic semiconductors (OSC)[2–12], polymers[13–15], metal-organic frameworks[16–19], and proteins[20, 21]. There are several methods for simulating phonons in different materials ranging from Density Functional Theory (DFT) to molecular dynamics (MD) and beyond.[11, 12, 22–24] However,

the most accurate method, DFT, is limited to small volumes of perfectly ordered materials due to its extreme conputational expense. In contrast, the methods capable of simulating larger, more complex systems have not been shown to be accurate across a large energy range ($\sim$10 - 10000 cm^{-1})[23]. Thus, an in-depth comparison of phonon predictions across methods is needed. In this article, we examine a wide variety of methods to simulate phonon modes in organic semiconductors. We compare the accuracy and computational expense of each method using the inelastic neutron scattering (INS) spectrum of high charge mobility rubrene.[25]

When validating simulated predictions, it is useful to compare not only to other simulations but also to experimental data. There are several experimental techniques which can offer insight into the phonon modes within organic semiconductors, including Raman scattering,[11] infrared spectroscopy,[26] terahertz spectroscopy,[3] and inelastic neutron scattering (INS).[27] The technique which stands apart is INS because it is capable of probing the largest energy range (5 - 8000 cm^{-1}). Additionally, it has no selection rules, meaning INS can be used to directly probe the density of dynamic states. By comparison, optical techniques only measure gamma point spectra for allowed transitions. Thus, the information density is higher for INS than for other validation techniques. More specifically, the VISION spectrometer at Oak Ridge National Laboratory (ORNL) is ideal for this comparison because it provides high brilliance and resolution over the important energy range of 5-600 cm^{-1}.[27]

Rubrene (Figure 2.1) was chosen as test case for this study for several reasons. First, it has the highest hole mobility (μ_h) of any small-molecule organic semiconductor.[25, 28] Second, it contains a significant number of hydrogen atoms with a large neutron cross-section, meaning it will give a strong signal to the VISION spectrometer.[29] Third, rubrene readily forms relatively large (mm-scale) crystals, ensuring that our measurements are valid for extended crystals.[30, 31] Finally, rubrene has been widely studied and is of interest for many groups.[25, 28, 30–34] In this study, INS spectra for rubrene were simulated using six different computational methods. Each method was optimized to achieve the most quantitatively accurate match between experiment and simulation. The

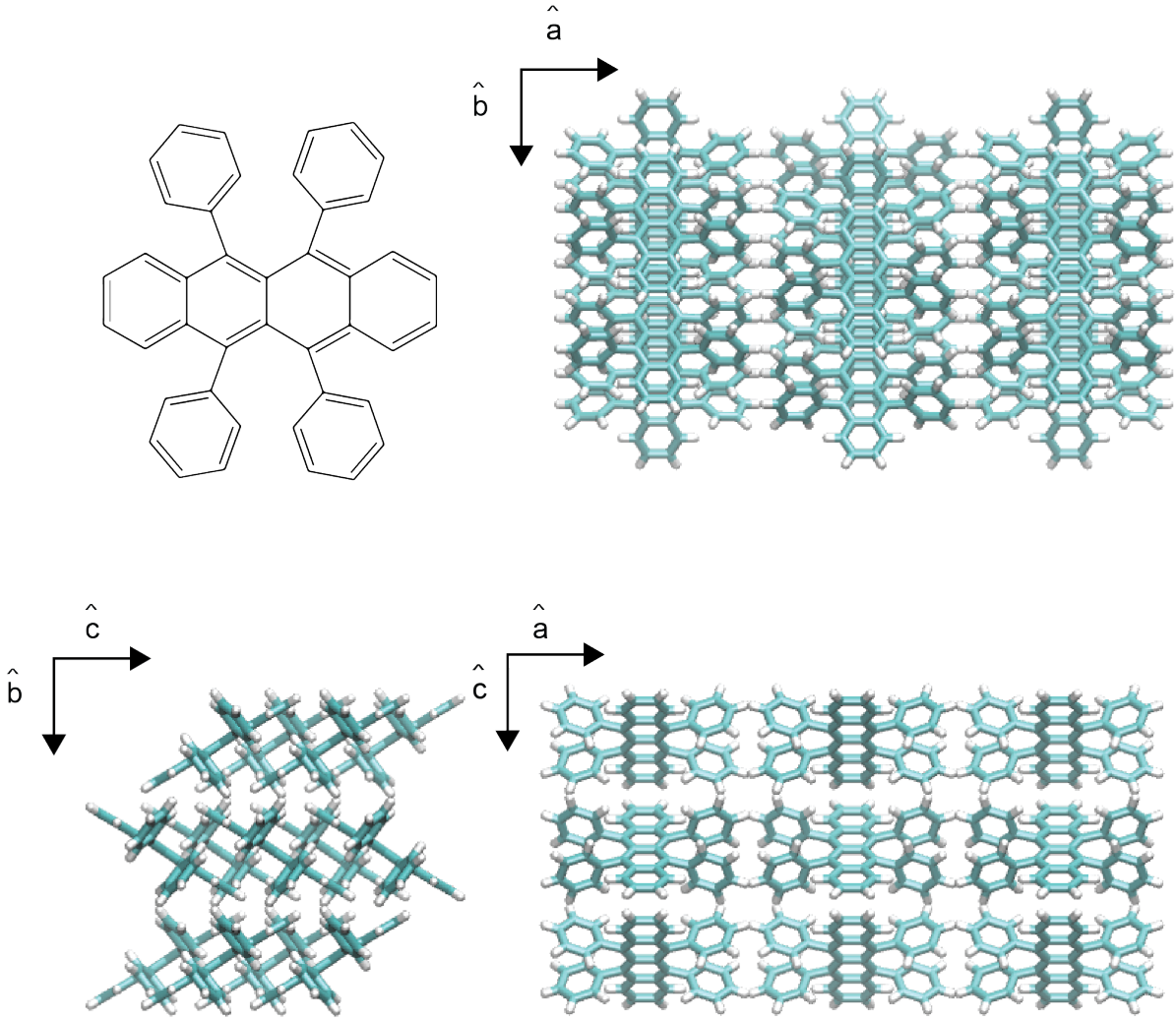

Figure 2.1. The molecular as well as the orthorhombic crystal structures of rubrene.

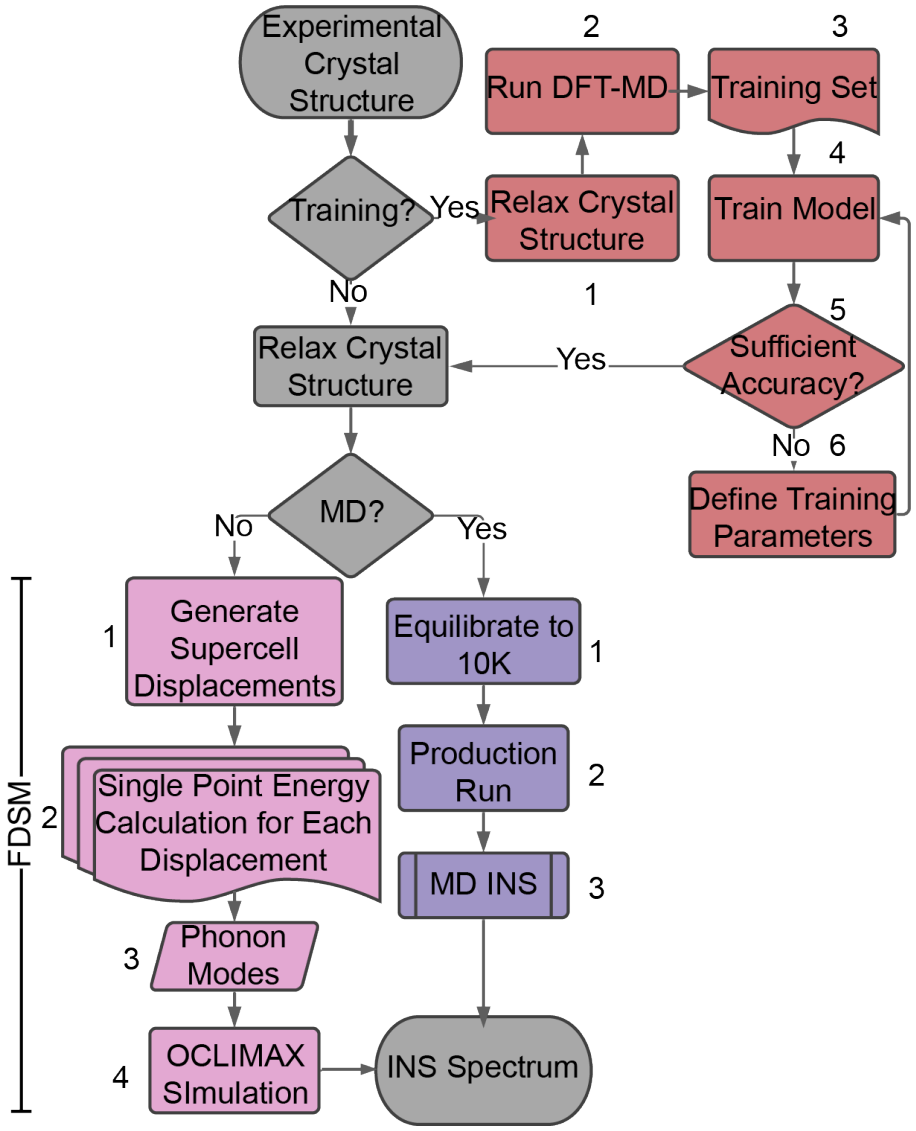

Figure 2.2. The workflow used for all of the calculation methods, where gray boxes indicate steps performed for all simulation methods. DFTB/ChIMES, ML, and MD were trained in this study and thus proceed through the red loop. The DFT, DFTB, and ANI-1 methods were not trained. DFT, DFTB, DFTB/ChIMES, ML, and ANI-1 used the finite displacement supercell method (FDSM, pink) while MD used a velocity-autocorrelation method (purple).

methods used were DFT, density functional tight-binding (DFTB)[35], the ANI-1 machine learning model[36], DFTB with a machine-learning ChIMES correction[22], a machine learning (ML) model based on a neural network[37], and a molecular dynamics-based technique (MD)[23]. Force matching to DFT was used to improve DFTB with ChIMES, ML, and MD[38]. Figure 2.2 shows the basic workflows for the six simulation techniques.

2.3 Results and Techniques

2.3.1 Untrained methods:

In this work, some simulation techniques required additional training, or changing the parameters of the calculator, while others did not. These untrained methods include DFT, DFTB, and ANI-1. DFTB and DFT were not trained because they are generally used as off-the-shelf calculators. However, DFTB can be trained to arbitrary accuracy by requiring a correction (e.g., Δ-machine learning[39]) or directly modifying the repulsive energy (e.g., through force-matching[40]) if additional training is desired. ANI-1 could have been trained more, but it was already trained on a large training set of organic molecules. For DFT, DFTB, and ANI-1, a finite displacement supercell method (FDSM) was used to compute the phonon density of states (Figure 2.2 pink).[12] This is the standard method for quantum-based simulation techniques.[3, 12, 22, 41] First, the crystal structure is relaxed using each method to match the CIF file (Crystallographic Information File).[42] Then, a supercell is formed and displacements are generated using phonopy [41] (pink 1 in Fig 2.2). Each atom in the crystal is translated 0.01 Å in the positive and negative x, y, and z directions. Next, the restoring forces on each atom and the system energy are calculated for each displacement (pink 2). Then the forces are collected and the phonon modes are calculated using phonopy (pink 3). Finally, the phonon modes are used to calculate the INS spectrum with oCLIMAX, a tool developed by INS beam scientists at ORNL to simulate the INS spectra of the VISION instrument from the calculated forces (pink 4).[43] This standard simulation workflow (gray then pink and ending up with gray for the spectrum) is used anytime the FDSM method is employed. Additional simulation details for DFT and DFTB can be found in Supplemental Information sections 1 and 2, respectively.

2.3.2 DFTB/ChIMES:

The DFTB [35] with ChIMES model was trained to determine the DFTB repulsive energy. Here, we have first computed the difference between results from DFT and the quantum mechanical parts of DFTB (i.e., the band structure and Coulombic energies). These

"repulsive free energy" quantities then become the training set for our DFTB/ChIMES model. In this case, we have predominantly trained on results for the ionic forces, though in practice fits can be made to the system's total energy and stress tensor as well[40]. ChIMES parameterization is performed by projecting the many-body interactions onto linear combinations of Chebyshev polynomials via an overdetermined linear least squares approach (See Refs. [22, 44] for further details).

For DFTB/ChIMES, the force predictions were improved using a training cycle (red blocks in Figure 2.2) to better match the DFT simulation. First, the experimental crystal structure was relaxed using DFT (red 1). Next, a training set was prepared by running DFT-MD and sampling the trajectory periodically (red 2 and 3). This DFT-MD run was performed at a high temperature to ensure a wide variety of configurations are sampled. After generating a training set of possible configurations, the various models were trained (red 4). After each training step was performed, the model was validated by comparing the differences in the predicted lattice constants between DFT and the trained model (red 5). Then, the training parameters were systematically varied and the model was refined (red 6). In this case, the training parameters were the order of the Chebyshev polynomials used for the 2- and 3-body interactions in ChIMES. The models produced by each set of training parameters were validated against the DFT forces and energies to find which set of training parameters produced the best model. By systematically checking every set of training parameters, we can be sure that the final model chosen has been trained to most accurately represent the measured sample.

The polynomial orders for the two-body terms were varied from 4 to 16 and the three-body terms were varied from 2 to 8. At each step, the unit cell was relaxed using the DFTB/ChIMES model and the lattice parameters were compared to the experimental lattice parameters. The full details of training are described in the Supplemental Information section 3. After the training was complete, FDSM (pink) was performed using DFTB/ChIMES as the force and energy calculator. This means that DFTB with ChIMES is theoretically equivalent to the other methods. Recently, the entire DFTB/ChIMES workflow has been wrapped in a command-line tool and python package known as DCS

Flow[45].

2.3.3 Machine Learning potentials:

In the case of ML, the atomistic simulation environment (ASE)[46] along with the atomistic machine learning package (AMP)[37] were used to train a neural net to calculate the forces and energies based on the atomic configuration of crystalline rubrene. A neural net is composed of an input layer, multiple hidden layers, and an output layer. The architecture of a neural net is defined by its hidden layers. For example, a neural net which has three hidden layers which has 2 nodes in the first layer, 7 in the second, and 4 in the third is a 2×7×4 neural net. In this case, the atomic positions are first transformed from x, y, and z coordinates to a rotation-invariant coordinate system called a Gaussian descriptor.[47, 48] A parameter set η defines how quickly the 2- and 3-body interactions fall off. A high η set means the local interactions will have a larger impact on the forces and energies of a given atom than for a low η set. Then the neural net takes these Gaussian descriptors as inputs and the forces and energies from DFT as the training set. The neural net changes the weights and biases in each node to recreate the DFT forces and energies in the training set given the associated Gaussian descriptor

As with DFTB / ChIMES, DFT was first used to relax the experimental crystal structure (red 1). Next, DFT-based molecular dynamics (DFT-MD) is performed to generate training and test sets (red 2 and 3). Though a similar method was used, distinct training sets were prepared for each method. Next, AMP was used to transform the x, y, and z coordinates from the training set into Gaussian descriptors and the neural net was trained on the training set (red 4). After each training, the accuracy was assessed by calculating the forces and energies on the test set (red 5). The parameters adjusted between training rounds were the architecture ($a \times b$) of the neural net and the symmetry parameter set η (red 6).

The full results of training can be seen in Supplemental Information section 4. The architecture was systematically varied from two hidden layers with three nodes each to three hidden layers with 10 nodes each. The 8×8 architecture converged the fastest, so we performed our symmetry tests on the 8×8 architecture. The fastest converging

architecture was chosen because the convergence time serves as a proxy for how well the model describes the system. For the symmetry tests, η was varied between $0.25\times$ to $4\times$ the default value $\eta_0 = [0.05, 4., 20., 80]$. It was found that an η set with values double the default provided the best force convergence. By systematically varying the training parameters, we produced the best ML model for our training set. Once the optimal model was found, FDSM was performed (pink) using the neural net as the energy/force calculator. This means that ML was treated equivalently to the other methods.

2.3.4 Classical Forcefield:

Typical MD forcefields have an analytical equation for each type of atomic interaction. Equation 2.1 defines the potential, $V(r)$ of a system in an MD forcefield. Here, the various k values (k_b, k_θ, k_ϕ, etc...) along with ϵ and σ define how strong each type of interaction is between a set of atoms. For instance, k_b defines the bond strength between two atoms. By changing these coefficients, the forces and energies are changed.

$$V(r) = \sum_{bonds} k_b(b - b_0)^2 + \sum_{angles} k_\theta(\theta - \theta_0^2) + \sum_{dihedrals} k_\phi \left(1 + cos(n\phi - \phi_0)\right) + \sum_{impropers} k_\psi(\psi - \psi_0)^2 + \sum_{\substack{non-bonded \\ pairs(i,j)}} 4\epsilon_{ij}\left[\left(\frac{\sigma_{ij}}{r_{ij}}\right)^{12} - \left(\frac{\sigma_{ij}}{r_{ij}}\right)^{6}\right] + \sum_{\substack{non-bonded \\ pairs(i,j)}} \frac{q_i q_j}{\epsilon_D r_{ij}} \quad (2.1)$$

Here b is the bond length, b_0 is the equilibrium bond length, k_θ is the force constant for angles, θ is the angle, θ_0 is the equilibrium angle, k_ϕ is the force constant for dihedrals, n is an integer, ϕ is the dihedral angle, ϕ_0 is the equilibrium dihedral angle, k_ψ is the force constant for improper dihedrals, ψ is the improper dihedral angle, ψ_0 is the equilibrium dihedral angle, ϵ is the depth of the Lennard-Jones potential well, σ is the distance at which the potential vanishes, r_{ij} is the distance between atoms i and j, q_i is the charge of atom i, and ϵ_D is the electric permittivity. The ForceBalance code[49] works by changing these coefficients until the forces and energies computed using the forcefield match DFT as closely as possible. Each time ForceBalance is run, the user decides which coefficients

(k, ϵ, and σ) to change.

Unlike other methods which require training, the first step here is to convert a molecule file obtained from the automated topology builder (ATB) into a crystal file which included periodic boundary conditions.[50–52] This process as well as the force-matching is detailed in Supplemental Information section 4. The starting forcefield also came from the ATB and was based an improved version of the GROMACS G54A7FF forcefield.[53–56]. Once a correctly-labeled crystal structure was generated, the crystal structure was relaxed (red 1). Next, DFT-MD was performed to produce a training set containing atomic positions as well as the DFT forces and energies for the configurations (red 2 and 3). ForceBalance was used to train the forcefield to reproduce the forces and energies from the DFT training set (red 4). After training, the root mean square error (RMSE) for the forces and energies was calculated to evaluate how well the training worked (red 5). By changing which coefficents were fit with ForceBalance, the optimal forcefield was produced.

After training, a velocity autocorrelation method, described in a previous publication, [23] was used. Starting from the relaxed crystal structure, the next step was to equilibrate the system to 10 K (purple 1), chosen because it is approximately the temperature for the INS experiment. Next, a production run of 500 ps was performed and the velocities were recorded at every step (purple 2). Finally, the velocity autocorrelation method was used to compute the INS spectrum (purple 3). This method was shown to be theoretically equivalent to the FDSM method. This was confirmed by performing the FDSM method as well (Supplemental Information Figure 7).

For this study, we initially allowed all coefficients to change, because we expected this would produce the best fit to DFT. However, only a small change was seen in the INS spectra after running ForceBalance. Inspecting the coefficients directly made it clear that the largest changes were in the σ and ϵ coefficients for the Lennard-Jones component. We ran ForceBalance again and only allowed the Lennard-Jones coefficients to change and the resulting INS spectrum was extremely similar to the previous spectrum (SI, Figure 5). Since neither forcefield produced an INS spectrum similar to the experimental spectrum, the force matching procedure was rerun on a higher-temperature training set.

This produced virtually no difference in the final forcefield. Finally, we assessed the impact of box size and production run length on the final INS spectrum (SI, Figure 6) to ensure we produced the best INS spectrum possible. While we could have experimented with different interaction types such as Buckingham potentials to describe the Van der Waals interactions, each forcematching run required 1-2 weeks and the computation of an INS spectrum took another 1-2 weeks running on a machine equipped with two 12-core Intel Xeon E5-2680 processors. Additionally, we were unable to make significant progress within our original forcefield framework, so we determined MD was unlikely to succeed at predicting INS spectra in general. Additional details about the MD simulations can be found in Supplemental Information section 5.

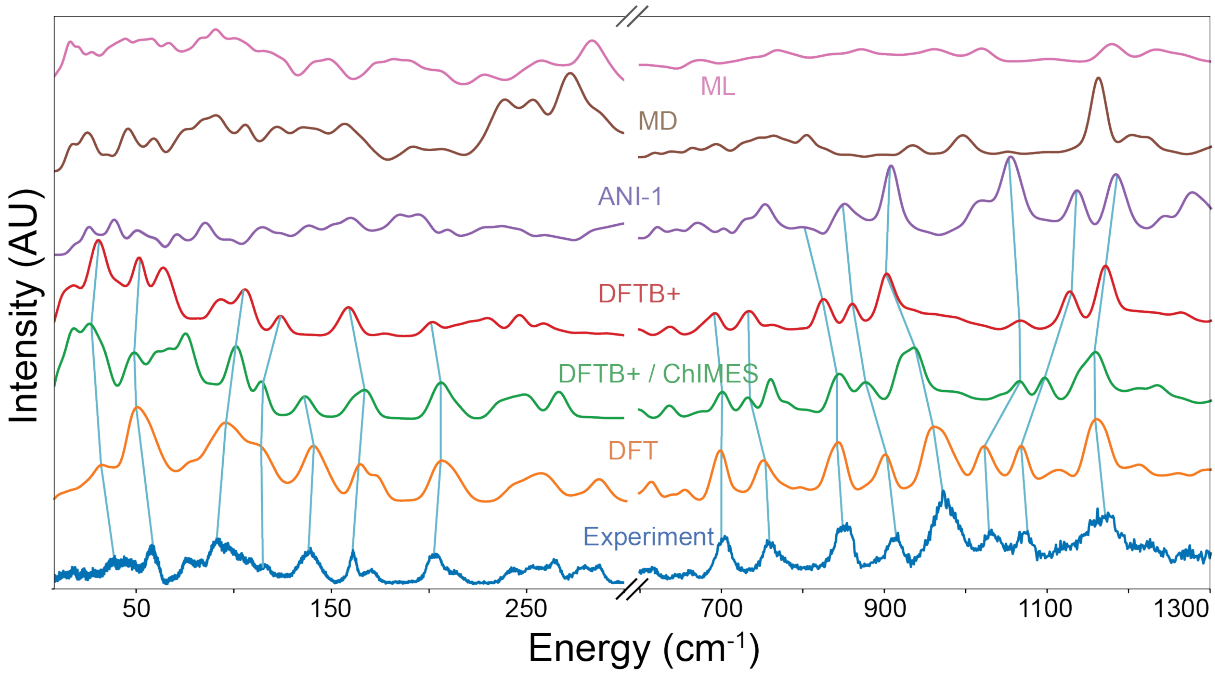

Figure 2.3. Comparison between simulation and experiment: The spectra produced by each method are shown. Light blue lines indicate corresponding peaks between spectra.

2.3.5 Comparison between simulation and experiment

Figure 2.3 shows the predicted INS spectra from each method, along with the experimental spectrum. The methods are ordered from bottom to top in order of accuracy. Traveling up, more peaks shift away from their experimental location and peaks appear

and disappear. In Figure 2.3, a light blue line is used to connect corresponding peaks from bottom to top. Across the entire energy range, many corresponding peaks can be found between the experiment, DFT, DFTB/ChIMES, and DFTB. There are a few regions where DFTB/ChIMES peaks can be found that DFTB does not predict such as $\sim$140 cm^{-1} and $\sim$250 - 300 cm^{-1}. In the higher energy range (800 - 1200 cm^{-1}), some peak assignments can be extended to ANI-1. Beyond that, none of the peaks could be confidently designated as shared between experiment and MD or ML.

The accuracies determined by peak comparison were confirmed by computing the distance between the curves. A simple least squares approach does not capture aspects such as the absence of a peak vs. a peak shift. Therefore, the Frechet distance is used to evaluate how similar each of the methods is to DFT, which is used as standard.[57] The Frechet distance is not computed with respect to experiment because the experimental spectrum would need to be smoothed. Different methods for smoothing the spectrum result in wildly different Frechet distances for each method. While the Frechet distance can capture some of the subtleties that the least squares approach misses, it is limited to curves of the same length. Since not all curves are of equal length, the overlapping portions of the curves are analyzed through partial curve mapping. The resulting error for each electronic simulation method compared to DFT is plotted in Figure 2.4 which shows that DFTB with a ChIMES correction most accurately reproduces the DFT spectrum followed by DFTB without the correction. The error continues to increase for ANI-1, MD, and ML. ANI-1 is likely more accurate than ML because it is trained on a much larger training set and the neural net contains many more nodes. Both factors are known to increase accuracy in neural nets. Finally, the error obtained from comparing to a spectrum containing random peaks is also shown. This serves to show that every method is better than a random guess, but the MD method is not much better than random data. The comparison shows that the spectra produced by DFTB/ChIMES and DFTB are both qualitatively and quantitatively similar to DFT, and nearly as accurate as DFT across 3 orders of magnitude of energy.

Figure 2.5 compares the computational cost and the estimated CO_2 emissions of each

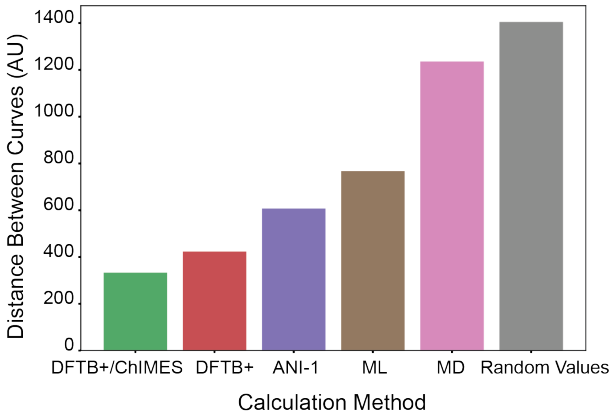

Figure 2.4. Frechet distance between the DFT spectrum and the spectra produced by each method. Partial curve mapping was used to determine the distance between curves.

quantum simulation method (DFT, DFTB, DFTB/ChIMES) for different supercell sizes. A supercell is made up of repeated unit cells. A 2×2×2 supercell contains two copies of the unit cell in each of the a, b, and c directions or eight molecules. The dashed red line indicates our annual NERSC allocation of 2 million CPU hours. Clearly, it is nearly impossible to perform DFT with even a 2×2×2 supercell size as it would require almost our entire annual NERSC allocation for a single simulation on a single configuration. Additionally, the estimated CO_2 emissions of a 2×2×2 DFT simulation are 10^4kg which is roughly equivalent to the annual carbon footprint of two people.[58] Moreover, there is no guarantee that this configuration is sufficient. On the other hand, DFTB and DFTB / ChIMES simulations with a 2×2×2 supercell show $10^3\times$ reductions in simulation time. In other words, switching from DFT to DFTB methods enables 1000 × more configurations to be simulated for the same computational expense. Alternatively, DFTB enables the simulation of larger supercells that would enable the introduction of structural anisotropy. Although not shown here, the time required for an MD run is lower than DFTB and the scaling (N^2) is preferable to the scaling of DFT, DFTB, and DFTB / ChIMES (N^3). Both ML and ANI-1 required less than an hour to perform a complete simulation. The times required for the spectra shown in Figure 2.3 are shown in Figure 9 of the Supplemental Information.

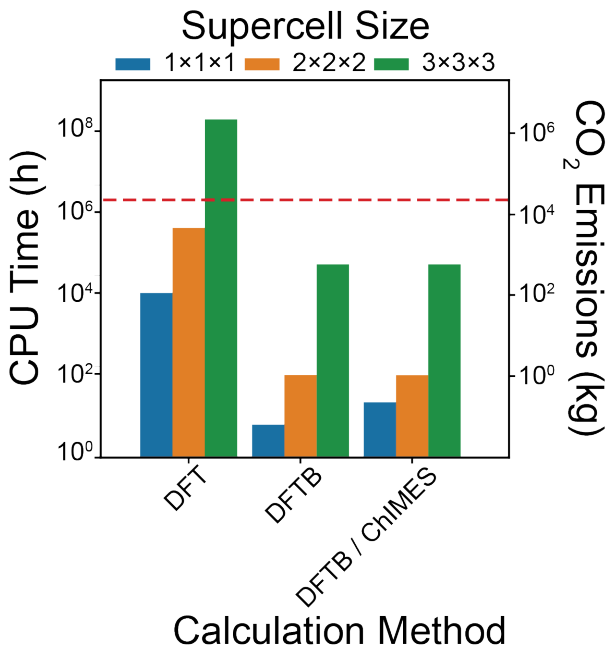

Figure 2.5. CPU time and CO_2 emissions for the three most accurate methods for a variety of box sizes. The actual box sizes used were 1x1x1 for DFT and 2x2x2 for DFTB and DFTB with ChIMES. The other values were estimated using the scaling law for each method (N^3). The values for DFTB with ChIMES do not include additional training. The dashed red line represents the yearly allocation for our group (2 million NERSC hours). The emissions data is based on a CPU with 8 cores and 130W thermal design power. The emission rate was based on the national weighted average CO_2 marginal emission rate for 2019[59].

2.4 Discussion

It is clear from Figures 2.3 and 2.5 that DFT was the most accurate technique, but had the greatest computational cost of the methods with acceptable accuracy. This means that DFT should be used when studying highly crystalline systems in which a high degree of accuracy is required. On the other hand, DFTB was still relatively accurate in predicting peak heights and intensities but required significantly less computational time than DFT. If we compare the time required for a 2×2×2 supercell using DFTB as shown in Figure 2.5, with the estimated 400,000 h required by DFT, there would be roughly three orders of magnitude reduction of simulation costs. This means that for less crystalline, or larger molecules DFTB or DFTB with ChIMES is a better option.

It is worth examining whether training a ChIMES correction is worth doing when DFTB already predicts phonon modes well. It is clear that the improvements from

ChIMES are real (Figure 2.4), but there is also a computational expense associated with creating these improvements (SI Figure 1). Ultimately, the true usefulness of ChIMES comes when studying large, complex systems. It has also been shown that a ChIMES model trained on a system containing a single molecule type can improve the predictions of forces and energies on other, similar molecules without additional training.[22] Thus, the computational cost associated with training is potentially only added once for a series of similar molecules. Since the computational cost of DFTB/ChIMES is nearly identical to DFTB without ChIMES at large box sizes (Figure 2.5), it is likely worth the additional computational time to train a ChIMES model when studying a series of large, complex systems. In our case, ChIMES was able to increase the accuracy in all regions of the spectra but most drastically in the 800 - 1200 cm^{-1} energy region. Here, the series of three peaks shifts to the lower energy region, nearer to the DFT and experimental spectra.

Recently, other methods for improving phonon predictions specifically within the DFTB framework have been examined. These include correcting the unit cell based on a DFT unit cell[24] and re-assigning phonon frequencies using a Γ-point DFT phonon calculation[60]. We note that our comparison does not include recent machine learning corrections to DFTB to yield high-level quantum chemical accuracy for molecular energies, specifically.[61–63] The main difference between ChIMES and these other phonon correction methods in DFTB is that ChIMES has demonstrated the ability to transfer a model determined from a single training set to multiple molecules[22, 45], rather than requiring the creation of unique parameter set for each system of interest. This means that when studying a series of similar molecules, the computational expense for the correction is only incurred once for ChIMES, enhancing its general appeal for predictions related to the vibrational properties of molecular crystals.

To understand why the MD, ML, and ANI-1 methods were less accurate, it is useful to examine the exact methodology for each. For MD, there is some agreement between the experimental and simulated spectra below roughly 200 cm^{-1}. This is due to the fact that the MD simulation was large (4×8×16 supercell) and that the intermolecular forces were well fit. Indeed, when comparing a forcefield in which all coefficients were allowed

to change to one in which only the Lennard-Jones parameters were allowed to change, there is virtually no difference (SI Figure 6). This means that the vast majority of the improvements in force prediction came from improving the Lennard-Jones parameters. It is possible that further improvement beyond what is shown here could be made, but the computational time required to try different training sets along with the researcher time required to check different interaction forms is significant.

When examining the spectrum produced by the ML method, it is difficult to identify any similarities between the experimental and simulated spectra. In this study, every parameter available in the AMP package was investigated and this is the best spectrum produced. It is possible that with larger training sets and neural net architectures, improvements could be made. If sufficient accuracy were somehow achieved without a computationally prohibitive training set, ML may even be preferable to DFTB or DFTB/ChIMES. However, ML is most likely best suited to be used as an alternative to ChIMES, as a way of improving the agreement between DFT and DFTB. This simpler problem should be more accessible for a neural net.

For ANI-1, there seem to be qualitative similarities between the simulated and experimental spectra in the 800 - 1100 cm^{-1} range. This makes sense because the training set for the ANI-1 model is composed of molecules up to 8 atoms in size. Therefore, it is not optimized for molecules the size of rubrene and should be expected to lose accuracy. In addition, the ANI-1 model is trained on isolated molecules. Because of this, it likely cannot describe the intermolecular interactions that contribute to low-energy modes. Conducting transfer learning on the ANI-1 calculator can improve predictions, and it is possible that training the ANI-1 model on larger systems could improve its predictive power on a system like rubrene.

2.5 Conclusion

Six methods for calculating atomic vibrations were compared for rubrene. The accuracy of each was evaluated by computing INS spectra with each method and comparing both to experimental data and the established simulation technique. These results allow us

to make the following broad recommendations. The DFT, DFTB/ChIMES, and DFTB methods were all able to produce accurate spectra across the entire INS energy range. The computational time required by DFT is much greater than for DFTB/ChIMES and DFTB. As such, DFTB/ChIMES and DFTB should be used in instances when speed or system size is a priority such as computational screening on a set with many materials or when trying to accurately reproduce the dynamics of large, complex systems like MOFs. DFT is still preferred on highly-crystalline systems when high accuracy is a requirement. Finally, ANI-1, MD, and ML are best suited to systems where speed requirements greatly outweigh accuracy such as long-term dynamics on large, disordered systems.

Bibliography

(1) Crabtree, G.; Glotzer, S.; McCurdy, B.; Roberto, J. *Computational materials science and chemistry: accelerating discovery and innovation through simulation-based engineering and science*; tech. rep.; USDOE Office of Science (SC)(United States), 2010.

(2) Fratini, S.; Mayou, D.; Ciuchi, S. *Adv. Funct. Mater.* **2016**, *26*, 2292–2315.

(3) Schweicher, G.; Avino, G. D.; Ruggiero, M. T.; Harkin, D. J.; Venkateshvaran, D.; Liu, G.; Richard, A.; Ruzié, C.; Kennedy, A. R.; Shankland, K.; Takimiya, K.; Geerts, Y. H.; Axel, J.; Fratini, S.; Sirringhaus, H. *Adv. Mater.* **2019**, *31*, 1902407.

(4) Shuai, Z.; Geng, H.; Xu, W.; Liao, Y.; André, J.-M. *Chem. Soc. Rev.* **2014**, *43*, 2662–2679.

(5) Oberhofer, H.; Blumberger, J. *Phys. Chem. Chem. Phys.* **2012**, *14*, 13846–13852.

(6) Wang, L.; Beljonne, D. *J. Phys. Chem. Lett.* **2013**, *4*, 1888–1894.

(7) Si, W.; Wu, C. Q. *J. Chem. Phys.* **2015**, *143*, 1–8.

(8) Troisi, A.; Orlandi, G. *Phys. Rev. Lett.* **2006**, *96*, 1–4.

(9) Heck, A.; Kranz, J. J.; Kubař, T.; Elstner, M. *J. Chem. Theory Comput.* **2015**, *11*, 5068–5082.

(10) Lee, N.-E.; Zhou, J.-J.; Agapito, L. A.; Bernardi, M. *Phys. Rev. B* **2018**, *97*, 115203.

(11) Bittle, E. G.; Biacchi, A. J.; Fredin, L. A.; Herzing, A. A.; Allison, T. C.; Hight Walker, A. R.; Gundlach, D. J. *Commun. Phys.* **2019**, *2*, DOI: 10.1038/s42005-019-0129-5.

(12) Harrelson, T. F. et al. *Mater. Horiz.* **2019**, *6*, 182–191.

(13) Bousige, C.; Ghimbeu, C. M.; Vix-Guterl, C.; Pomerantz, A. E.; Suleimenova, A.; Vaughan, G.; Garbarino, G.; Feygenson, M.; Wildgruber, C.; Ulm, F.-J., et al. *Nat. Mater.* **2016**, *15*, 576–582.

(14) Poelking, C.; Andrienko, D. *Macromolecules* **2013**, *46*, 8941–8956.

(15) Harrelson, T. F.; Cheng, Y. Q.; Li, J.; Jacobs, I. E.; Ramirez-Cuesta, A. J.; Faller, R.; Moulé, A. J. *Macromolecules* **2017**, *50*, 2424–2435.

(16) Latimer, A. A.; Kulkarni, A. R.; Aljama, H.; Montoya, J. H.; Yoo, J. S.; Tsai, C.; Abild-Pedersen, F.; Studt, F.; Nørskov, J. K. *Nat. Mater.* **2017**, *16*, 225–229.

(17) Cuadrado-Collados, C.; Fernández-Català, J.; Fauth, F.; Cheng, Y. Q.; Daemen, L. L.; Ramirez-Cuesta, A. J.; Silvestre-Albero, J. *J. Mater. Chem. A* **2017**, *5*, 20938–20946.

(18) Han, X.; Godfrey, H. G.; Briggs, L.; Davies, A. J.; Cheng, Y.; Daemen, L. L.; Sheveleva, A. M.; Tuna, F.; McInnes, E. J.; Sun, J., et al. *Nat. Mater.* **2018**, *17*, 691–696.

(19) Meekel, E. G.; Goodwin, A. L. *Cryst. Eng. Comm.* **2021**.

(20) Bellissent-Funel, M.-C.; Hassanali, A.; Havenith, M.; Henchman, R.; Pohl, P.; Sterpone, F.; Van Der Spoel, D.; Xu, Y.; Garcia, A. E. *Chemical reviews* **2016**, *116*, 7673–7697.

(21) Kayitmazer, A. B.; Seeman, D.; Minsky, B. B.; Dubin, P. L.; Xu, Y. *Soft Matter* **2013**, *9*, 2553–2583.

(22) Dantanarayana, V.; Nematiaram, T.; Vong, D.; Anthony, J. E.; Troisi, A.; Nguyen Cong, K.; Goldman, N.; Faller, R.; Moulé, A. J. *J. Chem. Theory Comput.* **2020**, *16*, 3494–3503.

(23) Harrelson, T. F.; Dettmann, M.; Scherer, C.; Andrienko, D.; Moulé, A. J.; Faller, R. *Sci. Rep.* **2021**, *11*, 1–12.

(24) Kamencek, T.; Wieser, S.; Kojima, H.; Bedoya-Martínez, N.; Dürholt, J. P.; Schmid, R.; Zojer, E. *J. Chem. Theory Comput.* **2020**, *16*, 2716–2735.

(25) Bisri, S. Z.; Takenobu, T.; Takahashi, T.; Iwasa, Y. *Appl. Phys. Lett.* **2010**, *96*, DOI: 10.1063/1.3419899.

(26) Mitchell, P.; Charles, H., *Vibrational spectroscopy with neutrons: with applications in chemistry, biology, materials science and catalysis*; World Scientific: 2005; Vol. 3.

(27) Seeger, P. A.; Daemen, L. L.; Larese, J. Z. *Nucl. Instrum. Methods Phys. Res., Sect. A* **2009**, *604*, 719–728.

(28) Reyes-Martinez, M. A.; Crosby, A. J.; Briseno, A. L. *Nat. Commun.* **2015**, *6*, 1–8.

(29) Horsley, A. *Nucl. Data Sheets* **1966**, *2*, 243–262.

(30) Schultz, J. F.; Li, L.; Mahapatra, S.; Shaw, C.; Zhang, X.; Jiang, N. *J. Phys. Chem. C* **2019**, DOI: 10.1021/acs.jpcc.9b09162.

(31) Miyadera, T.; Auchi, Y.; Koganezawa, T.; Yaguchi, H.; Chikamatsu, M. *APL Mater.* **2020**, *8*, DOI: 10.1063/1.5142307.

(32) Sutton, C.; Tummala, N. R.; Beljonne, D.; Brédas, J. L. *Chem. Mater.* **2017**, *29*, 2777–2787.

(33) Tang, X.; Pan, R.; Zhao, X.; Zhu, H.; Xiong, Z. *J. Phys. Chem. Lett.* **2020**, *11*, 2804–2811.

(34) Ma, H.; Liu, N.; Huang, J. D. *Sci. Rep.* **2017**, *7*, 1–12.

(35) Hourahine, B. et al. *J. Chem. Phys.* **2020**, *152*, DOI: 10.1063/1.5143190.

(36) Smith, J. S.; Isayev, O.; Roitberg, A. E. *Chem. Sci.* **2017**, *8*, 3192–3203.

(37) Khorshidi, A.; Peterson, A. A. *Comput. Phys. Commun.* **2016**, *207*, 310–324.

(38) Ercolessi, F.; Adams, J. B. *Europhys. Lett.* **1994**, *26*, 583.

(39) Ramakrishnan, R.; Dral, P. O.; Rupp, M.; von Lilienfeld, O. A. *J. Chem. Theory Comput.* **2015**, *11*, 2087–2096.

(40) Goldman, N.; Koziol, L.; Fried, L. E. *J. Chem. Theory Comput.* **2015**, *11*, 4530–4535.

(41) Togo, A.; Tanaka, I. *Scr. Mater.* **2015**, *108*, 1–5.

(42) Henn, D.; Williams, W.; Gibbons, D. *J. Appl. Crystallogr.* **1971**, *4*, 256–256.

(43) Cheng, Y. Q.; Daemen, L. L.; Kolesnikov, A. I.; Ramirez-Cuesta, A. J. *J. Chem. Theory Comput.* **2019**, *15*, 1974–1982.

(44) Lindsey, R. K.; Fried, L. E.; Goldman, N. *J. Chem. Theory Comput.* **2019**, *15*, 436–447.

(45) Cavalcante, L.; Daemen, L. L.; Goldman, N.; Moulé, A. J. *J. Chem. Inf. Model.* **2021**, *61*, 4486–4496.

(46) Hjorth Larsen, A. et al. *J. Phys.: Condens. Matter* **2017**, *29*, DOI: 10.1088/1361-648X/aa680e.

(47) Behler, J.; Parrinello, M. *Phys. Rev. Lett.* **2007**, *98*, 146401.

(48) Toukmaji, A. Y.; Board Jr, J. A. *Comput. Phys. Commun.* **1996**, *95*, 73–92.

(49) Wang, L. P.; Martinez, T. J.; Pande, V. S. *J. Phys. Chem. Lett.* **2014**, *5*, 1885–1891.

(50) Canzar, S.; El-Kebir, M.; Pool, R.; Elbassioni, K.; Malde, A. K.; Mark, A. E.; Geerke, D. P.; Stougie, L.; Klau, G. W. *J. Comput. Biol.* **2013**, *20*, 188–198.

(51) Koziara, K. B.; Stroet, M.; Malde, A. K.; Mark, A. E. *J. Comput.-Aided Mol. Des.* **2014**, *28*, 221–233.

(52) Malde, A. K.; Zuo, L.; Breeze, M.; Stroet, M.; Poger, D.; Nair, P. C.; Oostenbrink, C.; Mark, A. E. *J. Chem. Theory Comput.* **2011**, *7*, 4026–4037.

(53) Bekker, H.; Berendsen, H.; Dijkstra, E.; Achterop, S.; Vondrumen, R.; Vanderspoel, D.; Sijbers, A.; Keegstra, H.; Renardus, M. In *4th International Conference on Computational Physics (PC 92)*, 1993, pp 252–256.

(54) Berendsen, H. J.; van der Spoel, D.; van Drunen, R. *Comput. Phys. Commun.* **1995**, *91*, 43–56.

(55) Abraham, M. J.; Murtola, T.; Schulz, R.; Páll, S.; Smith, J. C.; Hess, B.; Lindahl, E. *SoftwareX* **2015**, *1*, 19–25.

(56) Huang, W.; Lin, Z.; van Gunsteren, W. F. *J. Chem. Theory Comput.* **2011**, *7*, 1237–1243.

(57) Eiter, T.; Mannila, H. *Computing discrete Fréchet distance*; tech. rep.; Citeseer, 1994.

(58) Watch, C. CAIT Data, data retrieved from CAIT, https://www.climatewatchdata.org/ghg-emissions, 2020.

(59) AVERT U.S. national weighted average CO2 marginal emission rate, year 2019 data, data retrieved from AVoided Emissions and geneRation Tool, https://www.epa.gov/avert, 2019.

(60) Cook, C.; Beran, G. J. *J. Chem. Phys.* **2020**, *153*, DOI: 10.1063/5.0032649.

(61) Stöhr, M.; Medrano Sandonas, L.; Tkatchenko, A. *J. Phys. Chem. Lett.* **2020**, *11*, 6835–6843.

(62) Li, H.; Collins, C.; Tanha, M.; Gordon, G. J.; Yaron, D. J. *J. Chem. Theory Comput.* **2018**, *14*, 5764–5776.

(63) Panosetti, C.; Engelmann, A.; Nemec, L.; Reuter, K.; Margraf, J. T. *J. Chem. Theory Comput.* **2020**, *16*, 2181–2191.

Chapter 3

Elucidating Correlated Defects in Metal Organic Frameworks Using Theory-Guided Inelastic Neutron Scattering Spectroscopy

3.1 Acknowledgement

Lucas Cavalcante was the primary investigator on this chapter. I performed some of the simulations and analysis. Tyler Sours did some of the foundational DFT work. Dong Yang and Bruce Gates created the sample. Luke Daemen is the instrument scientist at Oak Ridge who collected the data for us. Ambarish Kulkarni provided catalysis expertise which helped with the framing of this publication. Adam Moulé was the PI in charge of this project.

3.2 Introduction

As investigations of metal–organic frameworks (MOFs) have developed beyond synthesis, discovery, and bulk structure determination, researchers have increasingly focused on novel applications such as removal of water [1] and of CO_2 [2] from air. These potentially disruptive technologies require the MOF to be sufficiently stable under ambient conditions. MOF stability depends on the prevalence of structural defects and imperfections in the

underlying structure [3]. Defects include missing linkers and nodes and the presence of adventitious node ligands that arise during the synthesis. Defects have thus become central topics in MOF science; the associated challenges and opportunities have been recently reviewed.[4–8]

Although several studies have leveraged *defect engineering* in improving the catalytic and separation properties of MOFs, the role of defects on other properties (e.g., for energy storage,[9, 10] water purification,[11] supercapacitors,[12] electrocatalysis,[13, 14] mechanical properties,[15–17] conductivity,[18–21] optical properties[8, 22, 23]) is not well understood. Additionally, although we focus on porous MOF materials, we anticipate that defects play an important role in related materials such as dense MOFs [24–26] and porous organic cages.[27]

More specifically to the subject of this work, defects in UiO-66 MOFs are of great interest because they can act as catalytically active sites [28, 29] or as support sites for metal complexes [30, 31]. Investigations of the synthesis chemistry of MOFs such as UiO-66 provide insight into the control of defects.[32] The elucidation of the defect chemistry of MOFs is progressing using combined characterization techniques. Combined use of diffuse X-ray scattering, electron microscopy, and anomalous X-ray diffraction (XRD) demonstrated correlations between defects in a UiO-66 (Hf) MOF and phase separation between defective and defect-free regions on the nanoscale in hafnium-containing metal oxide cluster nodes.[33] High-resolution transmission electron microscopy (TEM) images have shown the evolution of defect distributions as function of MOF crystallization time.[34] Indirect characterization methods including thermogravimetric analysis [35], acid-base titration [36], nitrogen adsorption[3], and analysis of the products of MOFs digested in NaOH in D_2O by ^1H NMR spectroscopy[37] also enable quantification of defect chemistry and density, but cannot co-locate the chemical species with the physical structure. Table 3.2 summarizes the advantages and disadvantages of the mentioned techniques for characterizing defects in MOFs.

Notwithstanding these excellent characterization options, progress in relating MOF structure and chemistry to materials properties like catalytic activity and structural /

Methods	Advantages	Disadvantages
RAMAN/FTIR	Able to derive some local defect details	Not enough to characterize defect occupancy and define defect type
XRD	Able to derive crystal structure detecting missing clusters	No organic linker information (linker defects)
HRTEM	Detailed atomic observation of defects	Impractical to define/quantify all defects in the sample
Thermogravimetric analysis	Able to quantify defects	No atomic detail of the structures of defects
Acid-base titration	Able to quantify defects and reactive site information	No definition of the defect types (cluster or linker) and positions
Nitrogen absorption	Indicate existence of defects	No information on the definition/quantification of defects
1H NMR	Robust quantification	No atomic detail of the structure of defects
INS	Provide atomic-level structural / chemical details of the defects	Semiquantitative assessment of defects

chemical stability is limited by the lack of characterization techniques that provide atomic-level structural details. Here, we combine density functional theory (DFT) simulations with inelastic neutron scattering (INS) data to develop a general approach for spectroscopically characterizing defects in MOFs. We quantify the dynamics of missing linker defects and adventitious ligands in MOF UiO-66 using the low-frequency vibrational modes (¡ 100 cm^{-1}), measured by INS. Then we create an ensemble of possible defect configurations (e.g., the density and positions of missing linkers) in various topologies (e.g., fcu, bcu, reo, scu) with DFT. Quantitative comparison between the measured and simulated spectra is used to fingerprint the exact positions, density, and chemistry of missing linker defects and adventitious node ligands.

INS is effective for investigating structure and dynamic disorder in a wide range of materials.[38–40] Although INS has been used to investigate gas adsorption and phase changes in MOFs [41, 42], this technique has not been used to elucidate the structure of defects in these materials. INS is ideally suited to address the challenge of defect structure because, in contrast to XRD (which probes the structures of crystalline domains), INS is a quantitative spectroscopic technique that probes the dynamics of the whole sample. Unlike optical vibrational spectroscopies (e.g., Raman and infrared) that measure the energy exchanged by scattered photons which obey selection rules, INS is not limited by photon selection rules since it measures the exchanged energy of neutrons scattered by the atomic nuclei. Also, INS samples the complete Brillouin zone, not just the gamma point as for the optical spectroscopies, enabling resolution of phonons that cannot be detected using optical spectroscopies. In the SI, we present a comparison between optical spectroscopy methods (Raman and infrared) and INS, so the differences are made clear

to the reader [43]. Finally, owing to the high neutron scattering cross-section of the ^{1}H nucleus, INS is particularly sensitive to the molecular environment of organic linkers and node ligands. Because the ^{1}H atoms are present in a wide range of locations in the structural organic backbone, they are remarkably sensitive to subtle changes in the intermolecular environment.

We now illustrate the value of INS for structural characterization of UiO-66 samples that have been synthesized using modulators to incorporate node formate, acetate, and trifluoroacetate ligands. The extensive literature of UiO-66 provides a foundation for placing the new results in a broad context.[3, 7, 32, 34, 35, 37, 44–52] Since INS probes all the coupled vibrational modes involving hydrogen atoms, the interpretation of INS spectra is computationally challenging. Detailed modeling of the phonon modes (typically done with DFT) is necessary to link experimentally observed peak positions and intensities with specific vibrational modes. The high costs of the DFT calculations have, for the most part, limited this approach to simple crystalline materials with high structural symmetry (including a few nearly defect-free MOFs).[53, 54] For example,[42] combined DFT calculations with INS spectra to show the pressure-induced phase transition of ZIF-L to ZIF-8. Because defects in MOFs reduce the overall symmetry of the structure, INS simulations of defective MOFs require larger simulation volumes and are orders of magnitude more computationally expensive than those of their pristine analogs.

To work toward overcoming these limitations, we developed a Python-based workflow (denoted as DCS-Flow [55]) that facilitates seamless integration between the separate components of an INS simulation. DCS-Flow is an accurate, reproducible, efficient workflow for calculating phonon modes and the INS spectrum using DFT. The flowchart in Figure S1 in the Supporting Information summarizes our approach, which allows comparisons of experimental spectra with predictions from a library of candidate defect structures. We now illustrate the method by comparing predicted spectra with INS data characterizing UiO-66 with various node ligands. The results provide unprecedented insights into the structure of the missing linker defects and the ligands that reside on the Zr-nodes. We posit that this integrated experiment-theory approach can be broadly extended to a wide

family of MOFs.

3.3 Results and discussion

The structure of defect-free UiO-66 includes Zr_6O_8 nodes that are interconnected to form a fcu topology, where each node is bound to 12 linkers. The average connectivity of the nodes is controlled during synthesis by the use of modulators (e.g., acetic acid), which form anions that compete with the linker precursor anions during synthesis. For example, use of acetic acid (AA) as the modulator (with a modulator to $ZrCl_4$ mol ratio of 30) resulted a UiO-66 sample with 10.9(4) linkers/node (i.e., 1.0(6) missing linkers/node) where the number in parentheses is the numerical value of the standard uncertainty. We denote this material as UiO-66-AA. When trifluoroacetic acid (TFA) was used as a modulator instead of acetic acid, with the same modulator to $ZrCl_4$ ratio, the pKa of the synthesis solution was lower, the crystallization time was reduced, and the resulting MOF had 3.52 missing linkers per node. The experimental characterization (IR Spectroscopy, Powder X-ray Diffraction, Scanning Electron Microscopy, Transmission Electron Microscopy, Brunauer–Emmett–Teller (BET) Surface Area, Thermal Gravimetric Analysis, and ^{1}H NMR Spectroscopy) of the sample measured here was published previously by [37]

The linkers/node ratio, derived from ^{1}H NMR Spectroscopy, does not determine the relative positions of the missing linkers in the MOFs. The interpretation of linker and defect structure from the molar ratio is further complicated by the presence of other less-coordinated topologies in the UiO-66 samples.[33]

All the experiments were done at 5 K because the dynamics of the system can strongly suppress all neutron intensities at high temperatures, such as room temperature. A room-temperature spectrum is almost the same for any organic compound [40]. This point can be confirmed by the Debye-Waller factor, an exponential temperature-dependent term present in the scattering law that is used to model all modern neutron spectroscopy data.

3.3.1 Simulating defect free topologies

The main goal of this work is to develop an atomic-scale picture of the defective MOF structure. An appropriate starting point to understanding defects in UiO-66 topologies is

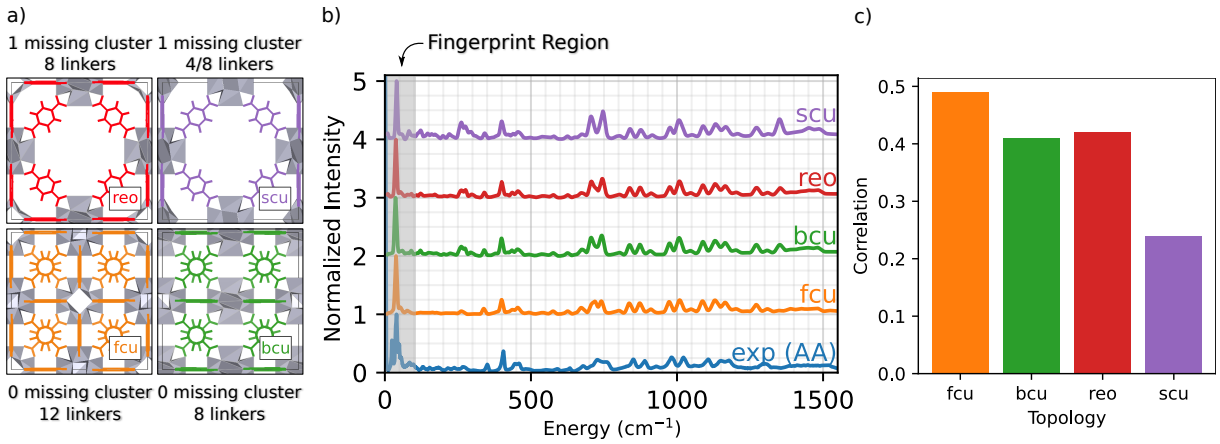

Figure 3.1. (a) Four proposed UiO-66 topologies; gray geometries represent the node clusters and colored geometries the linkers. (b) Comparison of INS spectra of UiO-66 at wavenumbers up to 1550 cm^{-1}. INS data of UiO-66-AA recorded at 5 K (blue curve) and DFT-simulated spectrum of the fcu (orange), bcu (green), reo (red), and scu (purple) topologies. The non-linker-occupied sites in the less-coordinated topologies (bcu, scu, and reo) are occupied by formate ligands. The gray shaded area in (b) denotes the INS fingerprint region (below 100 cm^{-1}). (c) Correlation comparison between experimental INS spectrum of UiO-66-AA and DFT simulated spectra of chosen topologies.

to simulate defect free and under-coordinated structures, shown in Figure 3.1a.[34] These under-coordinated topologies include varying numbers of missing linkers per node. The sites on the nodes where linkers are missing in UiO-66 are often occupied by adventitious ligands, including acetate derived from the acetic acid modulator and formate derived from DMF.[34] For example, the bcu topology presents the same density of Zr_6O_8 nodes as fcu (1 node / unit cell), but has 8 linkers per node instead of 12 linkers per node; thus there are four sites on each node that might either be capped by a proton or occupied by adventitious ligands. The reo and scu topologies have lower node densities per unit cell, meaning a more open MOF framework. The reo topology incorporates 8 linkers/node. The scu topology is more complex, with either 8 or 4 linkers/node. Figure 3.1b presents the simulated INS spectra of defect-free fcu, and defected bcu, reo, and scu topologies where the linker-occupied sites in the less-coordinated topologies (bcu, scu, and reo) are occupied by formate ligands derived from the DMF solvent. The simulation results are compared with the INS data for a UiO-66 sample synthesized with acetic acid modulator (i.e., UiO-66-AA).

The INS data characterizing the four topologies show some similar features, and excellent agreement between experiment and the INS simulations for the fcu topology over the entire energy range. The simulated INS spectra for the other topologies are less consistent with the data, especially in the regions of 250 and 1450 cm^{-1}; the peaks in these regions arise from the increased abundance of formate ligands in the under-coordinated topologies (details in Supporting Information). Two central conclusions emerge from this comparison:

1. our computational methods and the DCS-Flow approach are quantitatively accurate in predicting the vibrational modes and the resulting INS spectrum of UiO-66 over an energy range of 5-5000 cm^{-1} (Fig. S2).

2. the defect-free fcu topology provides the best overall representation of the UiO-66-AA sample among those investigated (details on how the correlation was calculated are given in the SI).

Conclusion 2 is especially encouraging because the experimental UiO-66-AA sample contains only 1.0(6) missing linkers/node.[37] Fig. 1c shows a quantitative comparison between the experimental and simulated spectra from Fig. 1b. The fcu structure shows the highest correlation, followed by equally good correlations between the bcu and reo topologies and a much poorer correlation with the scu structure. Assuming that the sample contains only pure fcu and bcu topologies that phase separate, then a sample with 1.0 missing linkers/node would be 75% fcu with no missing linkers and 25% bcu with 4.0 missing linkers/node.

We emphasize that the above analysis required a thorough testing of the parameters that are relevant for the INS simulation. Specifically, we evaluated the effect of DFT functionals, energy cutoffs, and mesh sampling of the phonon Brillouin zone to achieve optimal agreement with experiment, as reported previously [38]. We posit that such high-cost, high-quality simulations are necessary for direct comparison and correct interpretation of MOF INS experiments.

A fundamental advantage of INS over other vibrational spectroscopies is the high signal-to-noise ratio obtained at low wavenumbers (e.g., ¡ 100 cm^{-1}). These low-frequency

phonon modes are often associated with coupled motions (e.g., wagging, twisting, bending, rocking, breathing) that span several unit cells and involve multiple atoms in the structure. In the following sections, we demonstrate that this low-frequency INS data set serves as a fingerprint region for identifying the type (e.g., AA, formate, TFA), density, and relative positions of linkers and adventitious ligands bound to the Zr_6O_8 nodes in UiO-66.

Figure 3.2 compares the experimental INS measurement for UIO-66-AA (blue) with the DFT simulations of the INS spectrum in the low-frequency fingerprint region. The experimental INS data for UiO-66-AA data are characterized by four key features:

1. a major peak (denoted T_L) at about 40 cm^{-1} with a small, red-shifted shoulder ($\sim$35 cm^{-1})

2. a red-shifted double peak ($\sim$25 cm^{-1}, designated as A peak)

3. a blue-shifted double peak ($\sim$50 cm^{-1}, designated as B peak)

4. a broad shoulder at 55 cm^{-1} (designated as C peak)

Although the A, B, and C peaks are not observed in the simulations, all four topologies show a phonon mode close to T_L (i.e., 35 – 40 cm^{-1} region). To identify the specific molecular vibration corresponding to this peak, we calculate the eigenvalues and eigenvectors of the DFT-simulated dynamical matrix (determined using finite displacement, as implemented in Phonopy).[56] With this normal mode analysis approach, the eigenvalue for each phonon mode corresponds to the characteristic energy (i.e., the wavenumber), while the molecular motion itself is determined by the eigenvector (one vector for each atom in the system). Importantly, the eigenvectors are further analyzed to determine which atoms contribute to the phonon mode (e.g., node, linker, acetate ligand, etc.)

The above analysis shows that the T_L peak originates from a back and forth rocking/twisting motion about the longitudinal axis of the linker (Figure 3.2b, see *fcu_40cm-1.gif* animation in the SI). Since the phonon mode is dominated by linker motions (i.e., Zr_6O_8 nodes are not involved), it is observed at similar energies (and wavenumbers) across the different topologies. The slight differences in the position of the peak arise due to

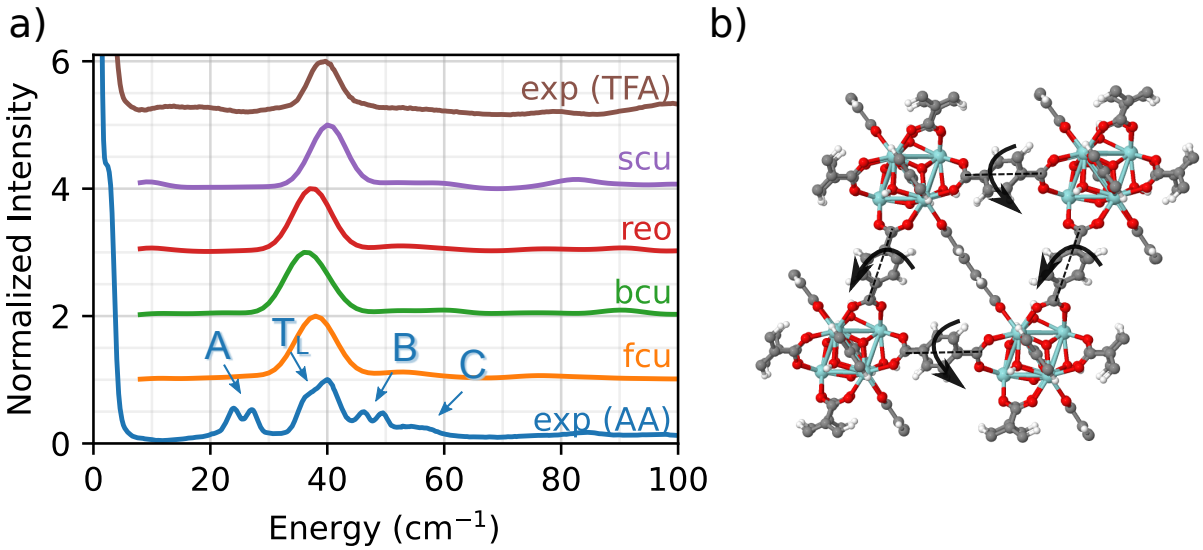

Figure 3.2. (a) Fingerprint region: INS spectra at frequencies up to 100 cm^{-1} for all simulated topologies and comparison with experiment for samples made with acetic acid called UiO-66-AA (blue) and trifluoroacetic acid called UiO-66-TFA (brown) modulators. Experimental peaks that are missing from the simulations and from the experimental spectrum of the sample modulated with trifluoroacetic acid are denoted as follows: A, a doublet at about 25 cm^{-1}; B, a doublet at about 45 cm^{-1}; and C, a shoulder at about 55 cm^{-1}. Because fluorine atoms have a low INS cross-section, peaks representing CF_3 dynamics are essentially missing from the INS spectrum, and the A, B, and C peaks are assigned to dynamics of the methyl groups of acetate ligands. (b) DFT-simulated vibrational mode corresponding to peak T_L is a rocking mode common to attached linkers in all topologies.

the small variations in the lattice constants for the four topologies. To the best of our knowledge, this is the first unambiguous assignment of a linker-specific phonon mode in the fingerprint region for any MOF. (The study by Deacon et al. was unable to identify modes below 200 cm^{-1}.[42])

We now explain the origin of A, B, and C peaks in the experimental INS. Since these features are not observed in the simulated INS spectra for any of the four topologies, we conclude that chemical defects due to the presence of adventitious synthesis-derived node ligands in UiO-66-AA are responsible for the peaks A, B, and C. Further evidence for this conclusion comes from comparison between the UiO-66-AA (blue) and UiO-66-TFA (brown) spectra (Figure 3.2a). The spectrum of UiO-66-TFA lacks the A, B, and C peaks and the TFA synthesized sample does not contain any acetate groups. Thus, we associate these peaks with the presence of acetate ligands in the structure. This

assignment is consistent with earlier work that shows that methyl groups in ZIF-8 are associated with a 25 cm^{-1} peak in the INS spectrum.[57] The computational models that consider only connectivity defects are incomplete and fail to capture the structural and chemical complexity of the experimental sample.

3.3.2 Simulating acetate ligands

To further investigate how the modulator acetic acid led to changes in the INS spectra, we created a library of UiO-66 models in which the formate ligands in the bcu, reo, and scu topologies were replaced with acetate ligands. This replacement resulted in a well-defined set of topologies with varying numbers of linkers and acetate ligands bonded to the nodes. In each of the three cases, the total coordination number of the node is 12.

A comparison of the predicted INS spectra of the three under-coordinated topologies with experiment is shown in Figure 3.3a. In contrast to the pristine fcu topology and the formate-containing bcu, reo, and scu topologies (Figure 3.2), we now observe many more peaks in the fingerprint region, indicative of the acetate ligands.

A central advantage of our DFT-based DCS-Flow approach is the ability it provides to computationally *set* the scattering cross-sections of individual atoms to zero. Thus, to isolate the vibrational modes that are related to these peaks, we set the cross-section of each atom except those of the acetate groups to zero. The resulting spectra in Figure 3.3b provides strong evidence that the low-energy doublets indeed originate from acetate groups bonded to the Zr_6O_8 clusters at defect sites.

The results show that the acetate group contributes differently to the INS spectrum depending on the topology, which means that the molecular environment around the acetate group strongly affects the correlated wag and twist motions of the methyl groups. Using bcu as an example (green in Fig. 3.3b), we observe two main features at 12 cm^{-1} (a1) and at 16 cm^{-1} (a2). This doublet corresponds to coupled twisting motions of two methyl groups (from the acetate) on opposing sides of the Zr_6O_8 node in a diagonal fashion (see Figure 3.3c). There are two different peaks because there are two different symmetric arrangements of methyl groups on each node. These modes are localized only on the methyl groups of the acetate ligand. Neither the linker (which dominates the T_L

peak) nor the Zr_6O_8 node is coupled to the doublet modes (see animations *bcu-4A_a1.gif* and *bcu-4A_a2.gif* in the SI).

In both the reo and scu cases, two different groups of acetate structures are involved in rocking motions that couple with the surrounding linkers. The coupling of the acetate motion with the linkers' motion increases the total energy of the mode. The scu simulated spectrum presents a stronger signal of peak C (Figure 3.3) because it contains a smaller number of linkers and a correspondingly larger number of acetate ligands.

This analysis shows that the A, B, and C peaks originate from the acetate defects and are associated with different phonon modes depending on the motions that are specific to the bonding environment in each topology. The slight disagreement in the peak positions ($\sim$10 cm^{-1}, 1.24 meV) of the bcu case is due to the fact that the INS simulations are performed using a 1x1x1 unit cell of the MOF, which corresponds to an infinite network of defective nodes. Nevertheless, our simulations provide strong evidence that the experimental A peaks arise from the coupled twisting of the methyl groups bound to the Zr_6O_8 node of UiO-66-AA. The phonon modes corresponding to a1 (*bcu-4A_a1.gif*) and a2 (*bcu-4A_a2.gif*) are presented in the SI as movie files.

We showed, in Figure 1, that the simulated INS spectrum from a non-defective lattice provides the best fit to the UiO-66-AA spectrum. This assignment was expected considering that the NMR measurements show an average ratio of one missing linker per node. This would correspond to a 3:1 volume ratio of fcu:bcu or fcu:reo topologies. The analysis in Figure 3 makes a strong case that the A peaks come from coupled acetate linkers in the bcu topology, because there were no peaks with energy below 40 cm^{-1} in the simulated INS spectra of the acetate defect reo and scu topologies. The B and C peaks however cannot be unambiguously assigned. Our analysis shows that the modes above 40 cm^{-1} in the fingerprint region are strongly coupled with the linker and the Zr_6O_8 node, but it is not unambiguous which acetate/linker geometry causes the doublet at B and the shoulder at C.

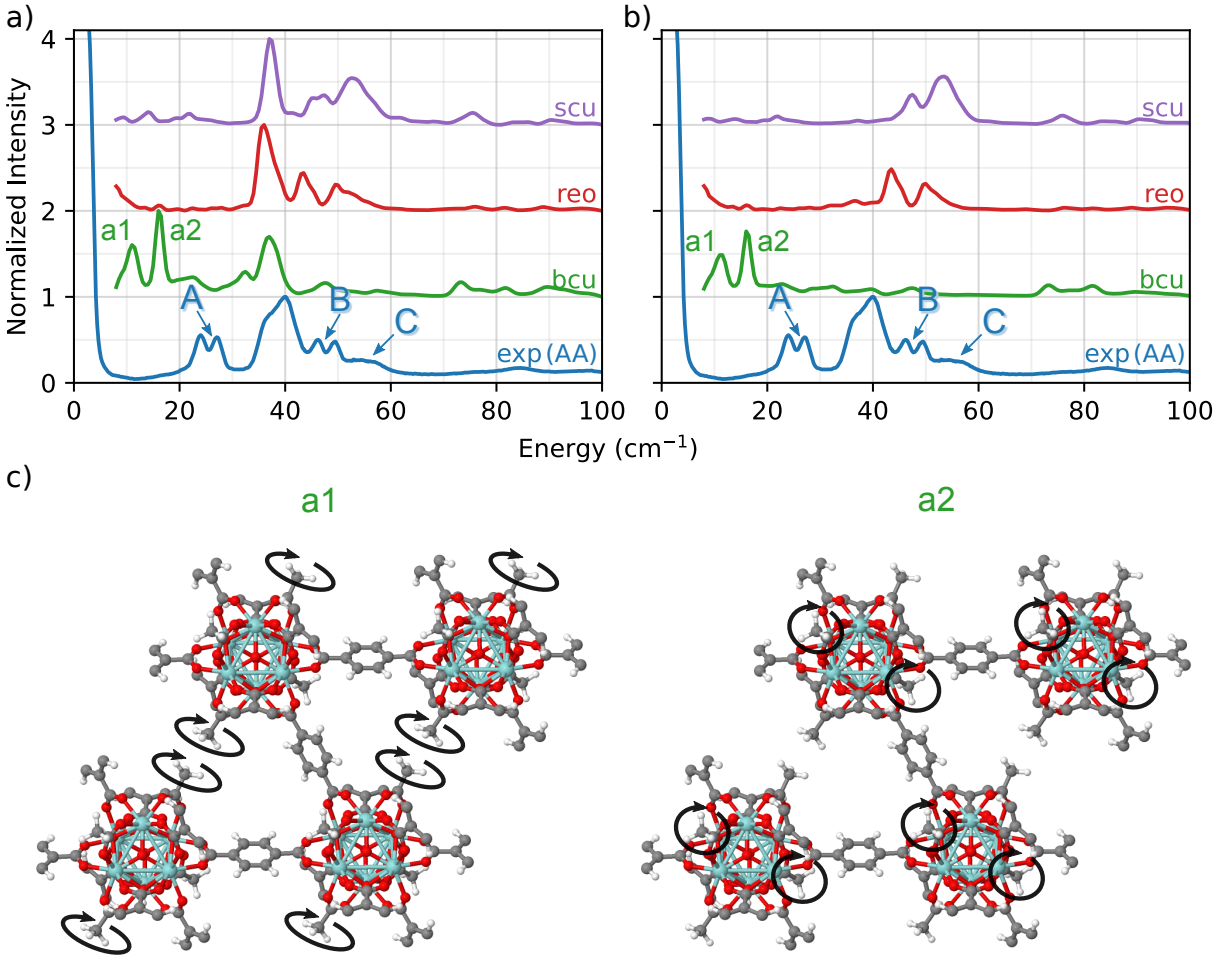

Figure 3.3. a) Simulated INS spectra characterizing defective topologies (bcu, reo, and scu) with missing linkers that provide sites for acetate ligands compared to INS experimental data of UiO-66-AA. (b) INS signal contribution of only the methyl groups in the MOF compared with complete signal determined by experiment of UiO-66-AA. (c) Vibrational modes related to peaks a1 and a2 of the bcu simulation.

3.3.3 Effect of defect symmetry

To address this issue, we focus on the bcu topology because it has the smallest unit cell, it has the same number of nodes as the fcu structure, and it provides a better fit to the full INS simulation in Figure 1 than either the reo or scu topologies. Indeed, the bcu topology can be considered as a defective fcu topology with four missing linkers per node. We consider four different variations of the bcu topology to demonstrate the structure sensitivity of the DFT-INS approach (Figure 3.4a). The four open missing linker sites on the bcu topology (i.e., missing linkers compared to fcu) can be occupied by either formate or acetate ligands. The simulated INS spectrum with all formate ligands (bcu-4F) was presented in Figure 1 and reproduced here (orange). The simulated INS spectrum with all acetate ligands (bcu-4A) was depicted in Figure 3 and reproduced here (green). Since the ^{1}H NMR data characterizing digested UiO-66-AA indicates the presence of both formate and acetate ligands on the node defect sites[37], we next consider the possibility that the four missing linker sites in the bcu topology were occupied by two acetate and two formate ligands. When the acetate groups are oriented diagonally with each other (bcu-2A2F, red spectrum in Figure 3.4b), we observe a single peak at 25 cm^{-1} at the correct energy for an A peak and a single peak at 52 cm^{-1}, which is the correct energy for a B peak. In Figure 3.4c, we present the mode corresponding to the peak at 25 cm^{-1} which consists of localized rotations of the acetate groups. The peak at 52 cm^{-1} includes significant contributions from the MOF linkers and involves coupled rocking motions of the acetate groups with the whole framework. The modes are also presented as animations *bcu-2A2F_a.gif* and *bcu-2A2F_b.gif* in the Supporting Information). The absence of the doublet (similar to peaks A and B in the experimental spectrum) arises because of the presence of a single diagonally opposite pair of acetate groups bound to the Zr_6O_8 node. The comparison suggests that the diagonal location of the acetate group results in vibrational motions at the correct frequencies, but the simple unit cell does not represent the heterogeneity of the environment surrounding the acetate in the measured sample.

To probe a greater degree of structural complexity, we simulated a 2x1x1 unit cell of the bcu topology with diagonal defects on one node and off-diagonal defects on the other

(bcu-2A2F-2F2A, purple spectrum in Figure 3.4). The simulated INS spectrum shows a doublet at 48 cm^{-1} and 52 cm^{-1} along with a broader peak centered at 60 cm^{-1}. The measured spectrum has a nearly identical doublet for the measured b1 and b2 peaks at 46 cm^{-1} and 50 cm^{-1} and the shoulder C peak is at 55 cm^{-1}. The slight offsets in the peak positions likely arise from the differences in the lattice constants of the computational model and the experimental sample. The motions corresponding to the doublet b involve coupled vibrations to the framework of neighboring acetate groups whereby one acetate rotates and the other rocks (b1), and vice versa (b2). Moreover, peak c is related to vibrations of all acetate groups from both the diagonals coupled to the framework (see the animations *bcu-2A2F-2F2A_b1.gif*, *bcu-2A2F-2F2A_b2.gif*, and *bcu-2A2F-2F2A_c.gif* in the Supporting Information). These results provide strong evidence that the experimental UiO-66-AA contains domains of the bcu-2A2F-2F2A defect structure that span multiple unit cells. Although the reo and scu topologies capped with acetates are able to reproduce peaks in the region of double peak b and shoulder c (see Figure 3.3), the INS simulation of the bcu-2A2F-2F2A defect structure is a much closer match to the experimental results.

In summary, the investigated sample, UiO-66-AA, has Zr-oxide nodes that have 12 possible linker attachment sites. The sample was prepared with adventitious node ligand acetate that occupies on average 1 of the 12 attachment sites. Formate was a second adventitious node ligand that was adventitiously introduced during synthesis. We first simulated all four of the known UiO-66 topologies (fcu, bcu, reo, scu) and compared them to the measured INS spectrum. The fcu produced the best fit across the full energy range, which tells us that the majority of the volume (75%) is a defect free fcu topology. We also showed that a series of INS peaks at frequencies below 100 cm^{-1} (labeled A, B and C) serve as fingerprint spectra for the acetate defect site. Next we simulated the bcu, reo, and scu topologies with all missing linker sites filled with acetate. Only the fully substituted bcu topology reproduced the A-peaks matching the doublet at 25 cm^{-1} which comes from a twisting motion of the acetate defect. The higher energy B and C peaks couple rocking motions of the acetate methyl group to twisting of the linkers, but none of the fully substituted acetate spectra matched the measured data, indicating again that

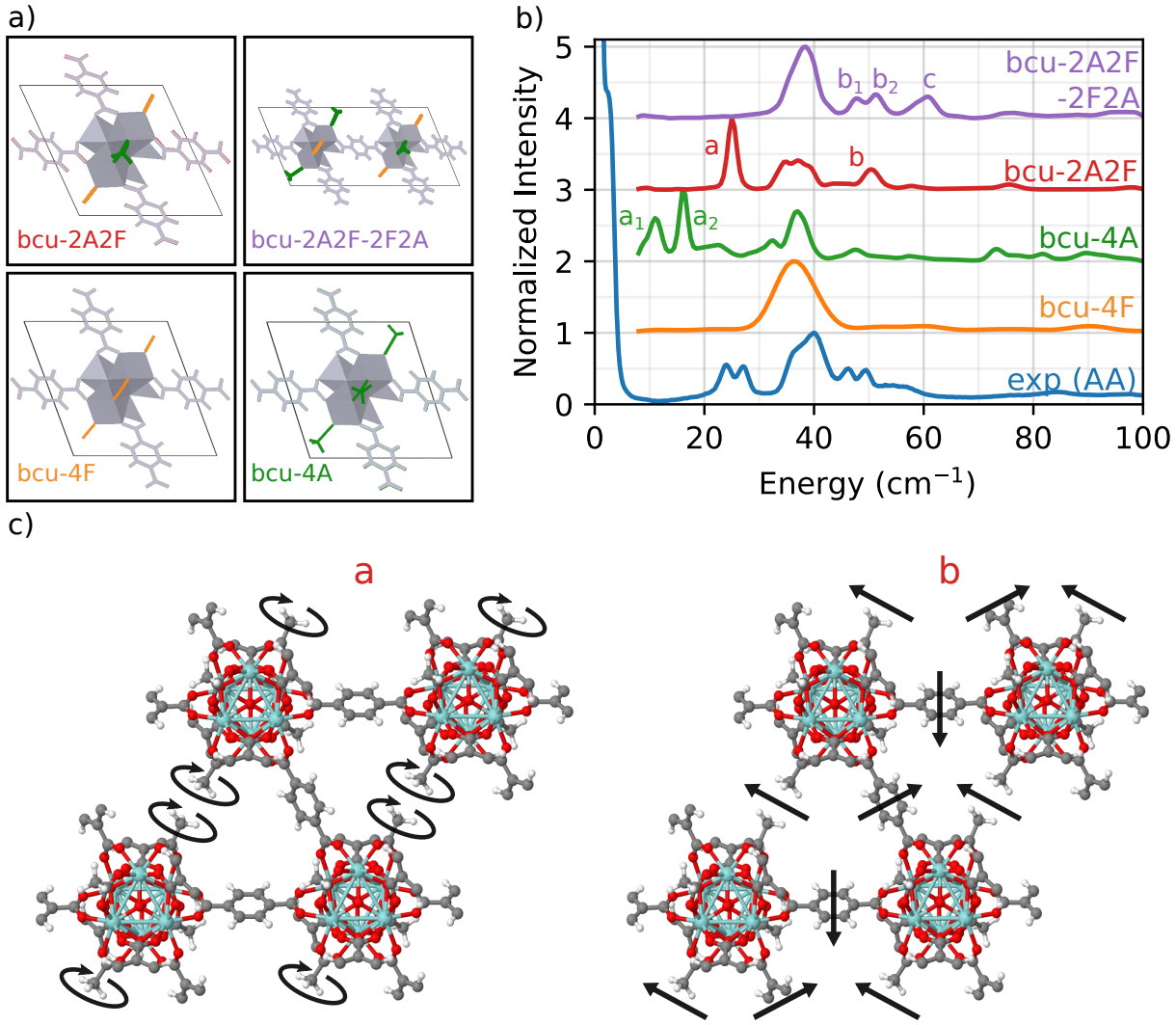

Figure 3.4. Analysis of bcu defect positions. (a) Simulation box containing bcu unit cell with the 4 missing linker sites occupied by formate ligands (bcu-4F), all 4 occupied by acetate ligands (bcu-4A), two formate groups and two acetate groups in a diagonal fashion (bcu-2A2F), and a 2x1x1 supercell with diagonal and off-diagonal defects (bcu-2A2F-2F2A). (b) Comparison of experimental INS spectra of UiO-66-AA up to 100 cm^{-1} with simulation of bcu UiO-66 MOF with various proposed defect configurations. (c) Vibrational modes related to peaks a and b of the simulation of bcu with diagonal defects (bcu-2A2F).

the reo and scu topologies were not present in the measured sample. Finally, we simulated the bcu topology with combined acetate and formate defects. Only geometries with acetate on opposite sides of the node and alternating orientation between neighboring nodes accurately reproduced the B-peak doublet and C-shoulder from the measured INS spectrum. We can therefore assign that 75% of the volume was the fcu topology with no defects. We assume, based on excellent previous work,[33] that the different topologies phase separate into domains. The remaining 25% of the volume seems to be roughly equally divided between the bcu topology with 100% of the adventitious node site occupied by acetate and the bcu topology with a 1:1 mixture of acetate and formate on the adventitious node sites. In the very roughly 12.5% of the volume with mixed acetate and formate, the sites ligands assume ordered arrangements, including occupying the opposite sides of the node and with alternating orientation between neighboring nodes. While our conclusions are consistent with a previous study by [34], the INS/DFT approach provides detailed structural insights (e.g., relative positions and number of acetate ligands) that are not possible with microscopy-based techniques.

3.4 Conclusions

We present a combined INS spectroscopic and simulation investigation of UiO-66 to characterize the geometry of adventitious defect sites occupied by ligands such as acetate and formate. INS spectroscopy is highly sensitive to the vibrational motions of linkers and defect species on MOF node defect sites because of the high resolution at low energies. Vibrations in the ¡100 cm^{-1} range include subtle wag and twist motions that capture details of the molecular-scale environment around the defect site, in this case coupling between wag motions by the methyl group on the acetate with twist motions on the terephthalate linker. We show a near quantitative match between the experimental INS spectrum and DFT simulated INS spectra, which demonstrates that this combination of experiment and theory is well-suited to characterization of heterogeneous reactive sites in MOFs. We suggest that this methodology should become part of the standard protocol for characterization of MOF structures.[58]

Bibliography

(1) Furukawa, H.; Gándara, F.; Zhang, Y. B.; Jiang, J.; Queen, W. L.; Hudson, M. R.; Yaghi, O. M. *Journal of the American Chemical Society* **2014**, *136*, 4369–4381.

(2) Rim, G.; Kong, F.; Song, M.; Rosu, C.; Priyadarshini, P.; Lively, R. P.; Jones, C. W. *JACS Au* **2022**, *2*, 380–393.

(3) Bueken, B.; Van Velthoven, N.; Krajnc, A.; Smolders, S.; Taulelle, F.; Mellot-Draznieks, C.; Mali, G.; Bennett, T. D.; De Vos, D. *Chemistry of Materials* **2017**, *29*, 10478–10486.

(4) Fang, Z.; Bueken, B.; De Vos, D. E.; Fischer, R. A. *Angewandte Chemie International Edition* **2015**, *54*, 7234–7254.

(5) Sholl, D. S.; Lively, R. P. *Journal of Physical Chemistry Letters* **2015**, *6*, 3437–3444.

(6) Dissegna, S.; Epp, K.; Heinz, W. R.; Kieslich, G.; Fischer, R. A. *Advanced Materials* **2018**, *30*, 1704501.

(7) Feng, Y.; Chen, Q.; Jiang, M.; Yao, J. *Industrial and Engineering Chemistry Research* **2019**, *58*, 17646–17659.

(8) Ma, X.; Wang, L.; Zhang, Q.; Jiang, H.-L. *Angewandte Chemie International Edition* **2019**, *58*, 12175–12179.

(9) Baumann, A. E.; Burns, D. A.; Liu, B.; Thoi, V. S. *Communications Chemistry 2019 2:1* **2019**, *2*, 1–14.

(10) Baumann, A. E.; Burns, D. A.; Díaz, J. C.; Thoi, V. S. *ACS Applied Materials & Interfaces* **2019**, *11*, 2159–2167.

(11) Cao, Y.; Mi, X.; Li, X.; Wang, B. *Frontiers in Chemistry* **2021**, *9*, 673738.

(12) Ferhi, N.; Desalegn Assresahegn, B.; Ardila-Suarez, C.; Dissem, N.; Guay, D.; Duong, A. *ACS Applied Energy Materials* **2022**, *5*, 1235–1243.

(13) Morales-Vidal, J.; García-Muelas, R.; Ortuño, M. A. *Catalysis Science & Technology* **2021**, *11*, 1443–1450.

(14) Wang, Z.-D.; Zang, Y.; Liu, Z.-J.; Peng, P.; Wang, R.; Zang, S.-Q. *Applied Catalysis B: Environmental* **2021**, *288*, 119941.

(15) Bennett, T. D.; Cheetham, A. K.; Fuchs, A. H.; Coudert, F.-X. *Nature Chemistry 2016 9:1* **2016**, *9*, 11–16.

(16) Cheetham, A. K.; Bennett, T. D.; Coudert, F.-X.; Goodwin, A. L. *Dalton Trans.* **2016**, *45*, 4113–4126.

(17) Zheng, B.; Fu, F.; Wang, L. L.; Wang, J.; Du, L.; Du, H. *The Journal of Physical Chemistry C* **2018**, *122*, 4300–4306.

(18) Choi, J. Y.; Park, J. *ACS Applied Electronic Materials* **2021**, *3*, 4197–4202.

(19) Talin, A. A.; Centrone, A.; Ford, A. C.; Foster, M. E.; Stavila, V.; Haney, P.; Kinney, R. A.; Szalai, V.; Gabaly, F. E.; Yoon, H. P.; Léonard, F.; Allendorf, M. D. *Science* **2014**, *343*, 66–69.

(20) Basu, O.; Mukhopadhyay, S.; Laha, S.; Das, S. K. *Chemistry of Materials* **2022**, *34*, 6734–6743.

(21) Islamov, M.; Babaei, H.; Wilmer, C. E. *ACS Applied Materials & Interfaces* **2020**, *12*, PMID: 33275844, 56172–56177.

(22) Jena, H. S.; Kaczmarek, A. M.; Krishnaraj, C.; Feng, X.; Vijayvergia, K.; Yildirim, H.; Zhao, S.-N.; Van Deun, R.; Der Voort, P. V. *Crystal Growth & Design* **2019**, *19*, 6339–6350.

(23) Taddei, M.; Schukraft, G. M.; Warwick, M. E. A.; Tiana, D.; McPherson, M. J.; Jones, D. R.; Petit, C. *Journal of Materials Chemistry A* **2019**, *7*, 23781–23786.

(24) Xin, L.; Fan, Z.; Li, G.; Zhang, M.; Han, Y.; Wang, J.; Ong, K. P.; Qin, L.; Zheng, Y.; Lou, X. *New Journal of Chemistry* **2017**, *41*, 151–159.

(25) Lorusso, G.; Natividad, E.; Evangelisti, M.; Roubeau, O. *Materials Horizons* **2019**, *6*, 144–154.

(26) Wu, Y.; Binford, T.; Hill, J. A.; Shaker, S.; Wang, J.; Cheetham, A. K. *Chemical Communications* **2018**, *54*, 3751–3754.

(27) Zhu, G.; Liu, Y.; Flores, L.; Lee, Z. R.; Jones, C. W.; Dixon, D. A.; Sholl, D. S.; Lively, R. P. *Chemistry of Materials* **2018**, *30*, 262–272.

(28) Rimoldi, M.; Howarth, A. J.; DeStefano, M. R.; Lin, L.; Goswami, S.; Li, P.; Hupp, J. T.; Farha, O. K. *ACS Catalysis* **2017**, *7*, 997–1014.

(29) Yang, D.; Ortuño, M. A.; Bernales, V.; Cramer, C. J.; Gagliardi, L.; *Journal of the American Chemical Society* **2018**, *140*, PMID: 29458253, 3751–3759.

(30) Bernales, V.; Yang, D.; Yu, J.; Gümüşlü, G.; Cramer, C. J.; Gates, B. C.; Gagliardi, L. *ACS Applied Materials & Interfaces* **2017**, *9*, PMID: 28537379, 33511–33520.

(31) Yang, D.; Odoh, S. O.; Borycz, J.; Wang, T. C.; Farha, O. K.; Hupp, J. T.; Cramer, C. J.; Gagliardi, L.; Gates, B. C. *ACS Catalysis* **2016**, *6*, 235–247.

(32) Chen, F. E.; Pitt, T. A.; Okong'o, D. J.; Wetherbee, L. G.; Fuentes-Rivera, J. J.; Milner, P. J. *Chemistry of Materials* **2022**, *34*, 3383–3394.

(33) Cliffe, M. J.; Wan, W.; Zou, X.; Chater, P. A.; Kleppe, A. K.; Tucker, M. G.; Wilhelm, H.; Funnell, N. P.; Coudert, F. X.; Goodwin, A. L. *Nature Communications* **2014**, *5*, 1–8.

(34) Liu, L.; Chen, Z.; Wang, J.; Zhang, D.; Zhu, Y.; Ling, S.; Huang, K. W.; Belmabkhout, Y.; Adil, K.; Zhang, Y.; Slater, B.; Eddaoudi, M.; Han, Y. *Nature Chemistry* **2019**, *11*, 622–628.

(35) Wu, H.; Yildirim, T.; Zhou, W. *Journal of Physical Chemistry Letters* **2013**, *4*, 925–930.

(36) Klet, R. C.; Liu, Y.; Wang, T. C.; Hupp, J. T.; Farha, O. K. *Journal of Materials Chemistry A* **2016**, *4*, 1479–1485.

(37) Wei, R.; Gaggioli, C. A.; Li, G.; Islamoglu, T.; Zhang, Z.; Yu, P.; Farha, O. K.; Cramer, C. J.; Gagliardi, L.; Yang, D.; Gates, B. C. *Chemistry of Materials* **2019**, *31*, 1655–1663.

(38) Harrelson, T. F. et al. *Mater. Horiz.* **2019**, *6*, 182–191.

(39) Harrelson, T. F.; Cheng, Y. Q.; Li, J.; Jacobs, I. E.; Ramirez-Cuesta, A. J.; Faller, R.; Moulé, A. J. *Macromolecules* **2017**, *50*, 2424–2435.

(40) Philip, C. H. (; Parker, S. F.; Ramirez-Cuesta, A. J.; Tomkinson, J., *Vibrational spectroscopy with neutrons: With applications in chemistry, biology, materials science and catalysis*; World Scientific Publishing Co.: 2005, pp 1–642.

(41) Casco, M. E.; Fernández-Catalá, J.; Cheng, Y.; Daemen, L.; Ramirez-Cuesta, A. J.; Cuadrado-Collados, C.; Silvestre-Albero, J.; Ramos-Fernandez, E. V. *ChemistrySelect* **2017**, *2*, 2750–2753.

(42) Deacon, A.; Briquet, L.; Malankowska, M.; Massingberd-Mundy, F.; Rudić, S.; Hyde, T. l.; Cavaye, H.; Coronas, J.; Poulston, S.; Johnson, T. *Communications Chemistry 2022 5:1* **2022**, *5*, 1–10.

(43) Vong, D.; Nematiaram, T.; Dettmann, M. A.; Murrey, T. L.; Cavalcante, L. S. R.; Gurses, S. M.; Radhakrishnan, D.; Daemen, L. L.; Anthony, J. E.; Koski, K. J.; Kronawitter, C. X.; Troisi, A.; Moulé, A. J. *The Journal of Physical Chemistry Letters* **2022**, *13*, PMID: 35695809, 5530–5537.

(44) Valenzano, L.; Civalleri, B.; Chavan, S.; Bordiga, S.; Nilsen, M. H.; Jakobsen, S.; Lillerud, K. P.; Lamberti, C. *Chemistry of Materials* **2011**, *23*, 1700–1718.

(45) Johnstone, D. N.; Firth, F. C. N.; Grey, C. P.; Midgley, P. A.; Cliffe, M. J.; Collins, S. M. *Journal of the American Chemical Society* **2020**, *142*, 13081–13089.

(46) Tan, K.; Pandey, H.; Wang, H.; Velasco, E.; Wang, K. Y.; Zhou, H. C.; Li, J.; Thonhauser, T. *Journal of the American Chemical Society* **2021**, *143*, 6328–6332.

(47) Wu, H.; Chua, Y. S.; Krungleviciute, V.; Tyagi, M.; Chen, P.; Yildirim, T.; Zhou, W. *Journal of the American Chemical Society* **2013**, *135*, 10525–10532.

(48) Øien, S.; Wragg, D.; Reinsch, H.; Svelle, S.; Bordiga, S.; Lamberti, C.; Lillerud, K. P. *Crystal Growth & Design* **2014**, *14*, 5370–5372.

(49) Vandichel, M.; Hajek, J.; Vermoortele, F.; Waroquier, M.; Vos, D. E. D.; Speybroeck, V. V. *CrystEngComm* **2014**, *17*, 395–406.

(50) Bennett, T. D.; Todorova, T. K.; Baxter, E. F.; Reid, D. G.; Gervais, C.; Bueken, B.; Van De Voorde, B.; De Vos, D.; Keen, D. A.; Mellot-Draznieks, C. *Physical Chemistry Chemical Physics* **2016**, *18*, 2192–2201.

(51) Zhou, F.; Lu, N.; Fan, B.; Wang, H.; Li, R. *Journal of Energy Chemistry* **2016**, *5*, 874–879.

(52) Atzori, C.; Shearer, G. C.; Maschio, L.; Civalleri, B.; Bonino, F.; Lamberti, C.; Svelle, S.; Lillerud, K. P.; Bordiga, S. *Journal of Physical Chemistry C* **2017**, *121*, 9312–9324.

(53) Cheng, Y. Q.; Daemen, L. L.; Kolesnikov, A. I.; Ramirez-Cuesta, A. J. *Journal of Chemical Theory and Computation* **2019**, *15*, 1974–1982.

(54) Dettmann, M. A.; Cavalcante, L. S.; Magdaleno, C.; Masalkovaitė, K.; Vong, D.; Dull, J. T.; Rand, B. P.; Daemen, L. L.; Goldman, N.; Faller, R.; Moulé, A. J. *Journal of Chemical Theory and Computation* **2021**, *17*, 7313–7320.

(55) Cavalcante, L. S.; Daemen, L. L.; Goldman, N.; Moulé, A. J. *Journal of Chemical Information and Modeling* **2021**, *61*, 4486–4496.

(56) Togo, A.; Tanaka, I. *Scr. Mater.* **2015**, *108*, 1–5.

(57) Casco, M. E.; Cheng, Y. Q.; Daemen, L. L.; Fairen-Jimenez, D.; Ramos-Ferná Ndez, E. V.; Ramirez-Cuesta, A. J.; Silvestre-Albero, J. *Chem. Commun* **2016**, *52*, 3639.

(58) Gropp, C.; Canossa, S.; Wuttke, S.; Gándara, F.; Li, Q.; Gagliardi, L.; Yaghi, O. M. *ACS Central Science* **2020**, *6*, 1255–1273.

Chapter 4

Catching the killer: Dynamic disorder design rules for small-molecule organic semiconductors

4.1 Acknowledgement

Lucas Cavalcante helped with the methods developement of ElPh. Corina Magdaleno helped with the documentation and development of ElPh. Adam Moulé was the PI in charge of this project.

4.2 Introduction

Small-molecule organic semiconductors are promising materials for various applications, including OLED displays in smartphones, photovoltaics, flexible transparent electronics, and bio-compatible medical devices[1–5]. However, organic semiconductors suffer from low charge mobilities (μ) due to large amplitude intra- and inter-molecular vibrations[6, 7]. These vibrations, referred to as phonons for the rest of this article, temporarily localize charge across a finite number of molecules, slowing transport. Although we have a basic understanding of why μ is limited, an essentially infinite design space for OSCs makes trial and error synthesis of new candidate molecules extremely inefficient. Thus, there

is a strong need for design rules to guide synthesis of new high μ materials. Transient localization theory correctly predicts μ in small-molecule organic semiconductors (OSCs) by simulating phonon modes and the electronic structure[8–10]. Although several works have used transient localization theory to predict electronic properties, design rules that effectively predict high μ for new structures remain elusive[8, 10–12].

Computation of μ within the transient localization framework requires accurate simulations of both the phonons and transfer integrals. A transfer integral describes how much the wavefunctions of neighboring molecules overlap and gives a measure of how difficult it is for charges to move between molecules. Phonons are calculated in the solid state, meaning systems are periodic and infinitely repeating[13, 14]. In contrast, transfer integrals are computed with quantum chemistry models in which individual molecules or pairs of molecules are considered either in a vacuum or a medium[15]. This difference mirrors the physical reality of charge transport in OSCs. In high-μ systems, band theory is used to model charge transport. In the band theory scenario, charges are delocalized across the entire material and only scatter due to thermal phonons[16]. For low-μ systems, charge transport is modeled using a hopping model in which localized charges hop to nearest neighbors[17–20]. Here, the transfer integral describes how often this hop can occur. Variable range hopping was introduced to bridge these two theories[21], but fails to match both thermodynamic and kinetic measurements[22]. Charge transport in small-molecule OSCs falls directly between the band transport and hopping transport scenarios. This is because fluctuations of the transfer integral due to phonons occur at the same order of magnitude as the average transfer integral[22, 23]. In other words, the phonons' influence on the transfer integral, known as electron-phonon coupling, is just as important as the average transfer integral. Thus, consideration of both periodic and isolated molecule models is critical to model high-μ OSCs accurately.

Accurate simulation of the phonon spectrum requires plane-wave density functional theory (DFT) calculations on periodic models[24–26]. Periodic models must be employed because the surrounding lattice significantly impacts the forces experienced by each atom. In contrast, accurate simulation of the electronic structure, especially the transfer integral,

requires DFT calculations with Gaussian basis sets performed on isolated molecules in a vacuum[27–29]. Because these simulations require multiple areas of expertise and different software packages, only components of the entire process appear in individual publications. The process from an experimental crystal structure (.cif) file to electron-phonon coupling often requires collaboration between several groups and months or years of collaborative work.[30–32] This slow process is incompatible with the type of multi-system studies necessary to search design space computationally and discover new synthetic design rules. Previously, we introduced DCS-Flow[33]: a workflow to compute the phonon modes using various calculators including DFT, density functional tight binding (DFTB)[34], or DFTB with a Chebyshev Interaction Model for Efficient Simulation (ChIMES)[35] correction from just a .cif file. Here, we introduce another workflow, ElPh, which works alongside DCS-Flow to compute the electronic structure using the method popularized by the Troisi and Fratini groups[6, 22, 23, 36]. Together, these workflows unlock the ability to compute the electron-phonon coupling using accurate phonon simulations. Moreover, we introduce a novel analysis technique that enables visual inspection of the impacts that each atom and each mode contributes to the transfer integral and dynamic disorder.

Electron-phonon coupling measures how much each phonon mode disturbs the transfer integral between neighboring molecules. Typically, the electron-phonon coupling is computed only en route to computing μ. However, any hope of finding design rules lies in the electron-phonon coupling because it can directly quantify the effect of each mode on charge transport and μ. Recent efforts to define synthetic design rules have focused on finding particular modes that limit μ[9, 37]. In contrast, the simulations that most accurately predict μ using transient localization theory included the entire spectrum of phonon modes,[8, 11] which suggests that consideration of the full spectrum of phonon modes is a requirement to generate practical synthetic design rules. As we will demonstrate, each molecule contains thousands of phonon modes that are difficult or impossible to compare, even between similar materials. Thus, a new analysis technique is required: one in which all phonon modes are considered, but one that can also help explain differences in performance between similar and dissimilar molecules.

Here, we demonstrate a method to quantify the total impact of each atom on charge transport. This method makes it possible to analyze molecules with different structures and identify the impacts of design motifs like side chains or backbone length on μ. We believe that this simulation workflow and visualization strategy will prove valuable in uncovering synthesis design rules for small-molecule OSCs.

4.3 Methods

Figure 4.1 shows the workflow to compute the electron-phonon coupling and μ. The workflow splits into two paths, starting with an experimental structure determination, often with a .cif file. To the right (yellow), DCS-Flow is our previously published method that calculates all of the phonon modes for a particular molecular crystal.[33] DCS-Flow is a platform-independent plane-wave calculator that can run with VASP (Vienna Ab Initio Simulation Package), CASTEP, DFTB+, or DFTB+ with ChIMES depending on the desired level of accuracy and computational efficiency. The phonon simulations employ periodic boundary conditions to ensure that the computed dynamics are as accurate as possible. We used VASP with the PBE functional in this study to ensure the highest accuracy. We previously explored the impacts of various functionals on the accuracy of dynamics in small molecule OSCs.[8] The dynamics were validated by computing a simulated inelastic neutron scattering (INS) spectrum and comparing it to experimental data[38]. We demonstrated nearly quantitative matching to INS spectra over three orders of energy for a variety of common small molecule OSCs using these techniques.[8, 11, 30, 39]

The left side of the workflow (green) computes the electronic contributions to μ. This part of the workflow employs Gaussian-based DFT without periodic boundary conditions to ensure the best possible description of the electronic structure. This technique is described in a series of papers from the Troisi group[31, 32, 36, 40, 41]. This study employed the 3-21G* basis set which has been reported to accurately capture the electronics of these types of systems[23, 40]. The structure must first be "unwrapped" to discard the periodic boundary. Figure 4.1B shows the structure described by the raw rubrene .cif file. The

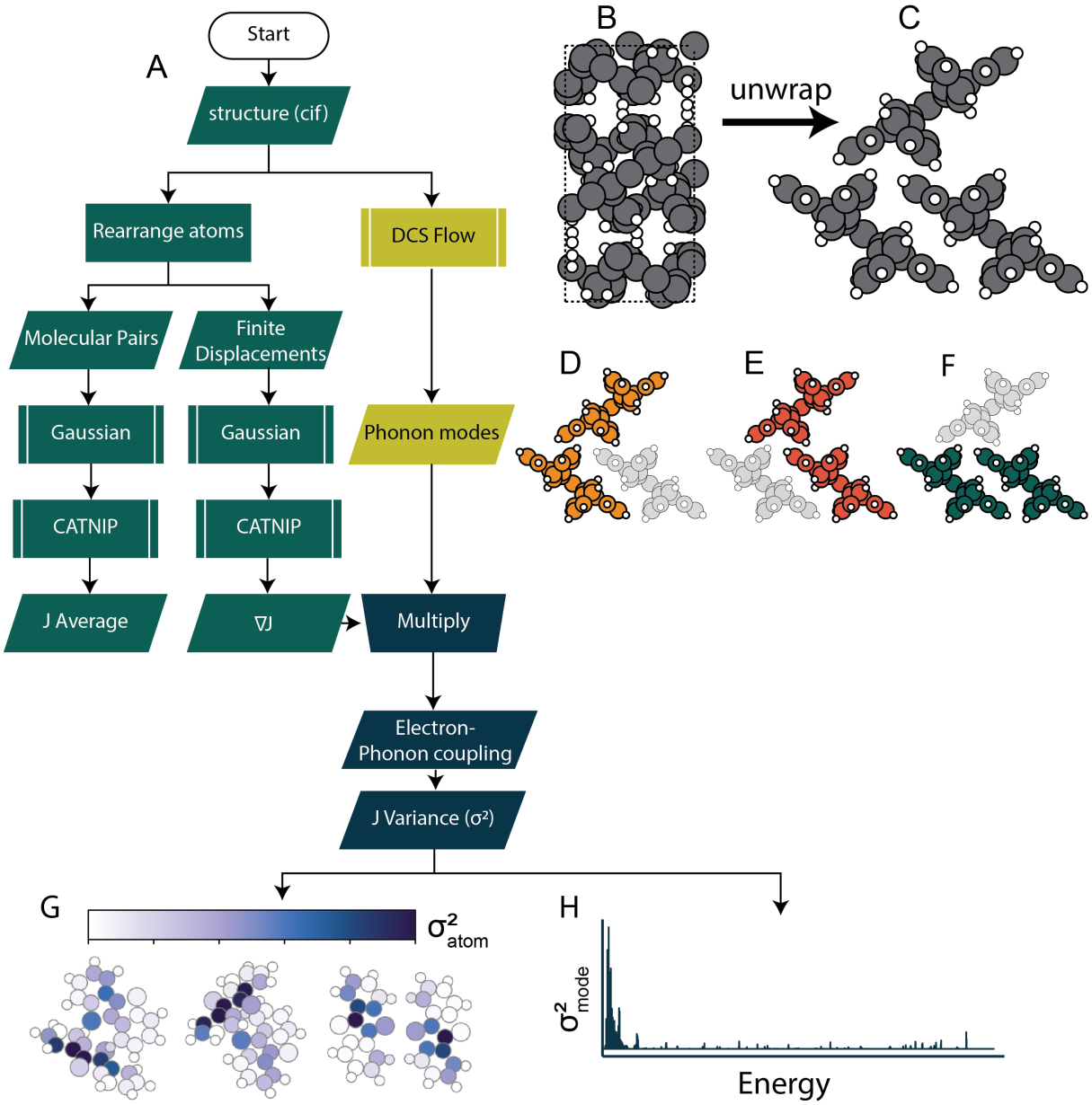

Figure 4.1. **Simulation workflow:** A The workflow showing how to compute the electron-phonon coupling for a small-molecule OSC. The green part of the workflow indicates that periodic boundary conditions are not considered. The yellow part indicates that periodic boundary conditions are considered, and the blue part indicates that a mix of periodic and non-periodic results are used together. (Right) An illustration of the process of going from a periodic system to molecular pairs. B shows the periodic structure of rubrene from a .cif file. C shows what three molecules look like after unwrapping the periodic structure. D, E, and F show the distinct molecular pairs within the high-μ plane. G and H show the variance of the transfer integral per-atom and per-mode, respectively.

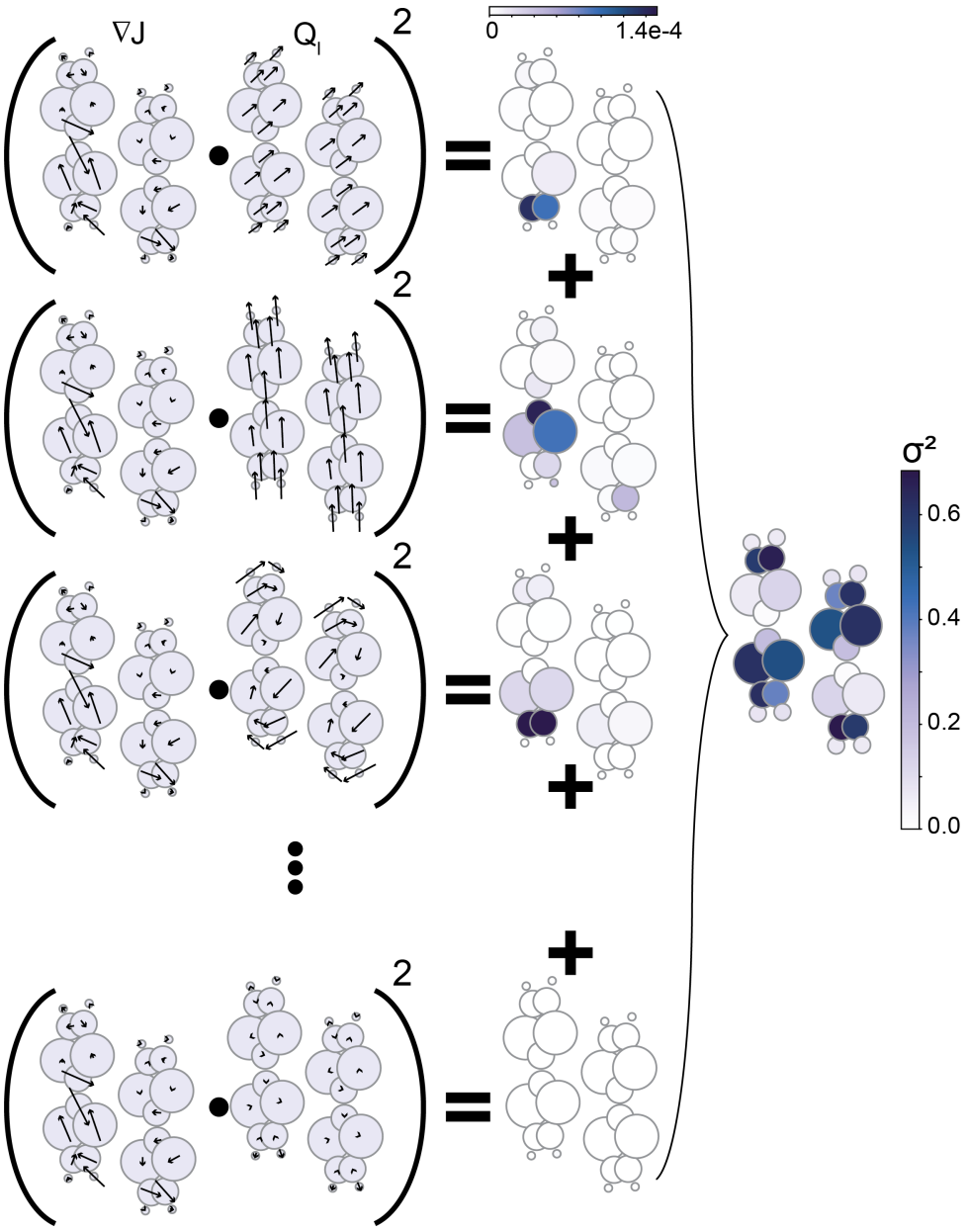

Figure 4.2. **Visualization of the atom-specific dynamic disorder:** The derivative of the transfer integral (∇J) is projected onto the atomic displacements resulting from each phonon mode (Q_l) resulting in the mode specific variance of the transfer integral (σ^2_{mode}). The magnitude of the effect on each atom (σ^2_{atom}) is visualized as a 3D heat map where the heat of the atom indicates how much each atom in a particular mode limits μ. Summing the contribution from each mode gives the total variance of the transfer integral, σ^2.

dotted box represents the periodic boundaries. Next, the workflow identifies molecular pairs within the high-μ plane. Figure 4.1C is the unwrapped structure with the three unique molecules. Figures 4.1D, E, and F show each pair of molecules. Depending on the crystal structure, these materials can have up to three distinct pairs but may have as few as one. For completeness, all three pairs are considered in this study, regardless of whether or not they should be identical. Next, the electronic structure of each configuration is computed using Gaussian. Then a finite-displacement scheme is used to compute the gradient of the transfer integral. The workflow then employs the ChArge TraNsfer Integral Package (CATNIP) package to obtain the transfer integral, J, for each pair and displacement from the electronic structure[42, 43]. These results yield the average J for each pair and the gradient of J ($\boldsymbol{\nabla} J$) for each atom. Finally, the workflow multiplies $\boldsymbol{\nabla} J$ by the phonon modes computed with DCS-Flow ($\boldsymbol{Q}$) to obtain the electron-phonon coupling for each atom and each mode. Summing over all atoms and modes yields the variance of J, σ^2.

$$\sigma^2_{ij,T} = \left\langle (J_{ij} - \langle J_{ij} \rangle)^2 \right\rangle = \frac{1}{N_q} \sum_l \frac{|g^l_{ij}|^2}{2} \coth\left(\frac{\hbar\omega_l}{2k_B T}\right) \tag{4.1}$$

is the variance of the transfer integral. Here, N_q is the number of points that sample the reciprocal space, and g^l_{ij} is the electron-phonon coupling between molecules i and j due to mode l and ω_l is the frequency of mode l. The variance (σ^2) represents a thermal average of how the phonon modes affect the transfer integral. Here, $g^l_{ij} = \nabla J_{ij} \cdot Q_l$ where ∇J_{ij} is the gradient of the transfer integral between molecules i and j and Q_l are the atomic displacements for mode l. $\sigma^2_{ij,T}$ is a useful measure, but summing over all atoms and modes does not allow for a mode-by-mode or an atom-by-atom analysis. Thus, we define the variance for atoms as

$$\boldsymbol{\sigma}^2_{ij,atom} = \frac{1}{N_q} \sum_l \frac{\left(\boldsymbol{g^l_{ij}}\right)^{\mathbf{2}}}{2} \coth\left(\frac{\hbar\omega_l}{2k_B T}\right) \tag{4.2}$$

and the variance for modes as

$$\boldsymbol{\sigma}^2_{mode} = \frac{1}{N_q} \sum_a \frac{\left(\boldsymbol{g}^l_{ij}\right)^2}{2} \coth\left(\frac{\hbar\omega_l}{2k_BT}\right) \tag{4.3}$$

Here, $\boldsymbol{\sigma}^2_{mode}$ is a vector containing the total contribution to σ^2 for each mode and $\boldsymbol{\sigma}^2_{ij,atom}$ is a vector containing the total contribution to σ^2 for each atom. In other words, $\boldsymbol{\sigma}^2_{mode}$ tells how much each mode limits μ while $\boldsymbol{\sigma}^2_{ij,atom}$ tells how much each atom limits μ.

Figure 4.2 is a visual representation of the math presented above for tetrathiafulvalene (TTF). In each row on the left, the same ∇J is projected onto the atomic displacements (Q_l) of each mode and squared. This gives the square of the electron-phonon coupling for each mode. This can be represented as a heatmap as in the third column. Summing these along with an energy-based factor gives the variance for each atom as shown by the heatmap on the far right. Note that this can be performed for each pair identified in figure 4.1. This is a measure of how much each atom limits μ.

4.4 Results and Discussion

A useful analysis of the electron-phonon coupling for molecular design should be able to reveal several pieces of information. First, the analysis should quantitatively predict differences in μ between similar molecules with variations in molecular structure (i.e. different side chains). Second, the analysis should explain how design decisions can improve or reduce the μ within similar molecules. Finally, the analysis should help synthetic chemists design new, higher-performing materials by discovering new design rules.

4.4.1 Mode Analysis

A mode analysis technique has been widely used to search for design rules for higher μ OSCs[8, 9, 11, 44–47]. A mode analysis involves simulating all of the phonon modes and then calculating which phonon modes most contribute to the reduction of μ. Here, we use $\boldsymbol{\sigma}^2_{mode}$ to describe this. A mode analysis for a series of BTBTs and -acenes is shown in figure 4.3. Figures 4.3a and 4.3B show the contribution to the variance for each mode. In many studies, this analysis is performed using only the gamma point phonons. We recently

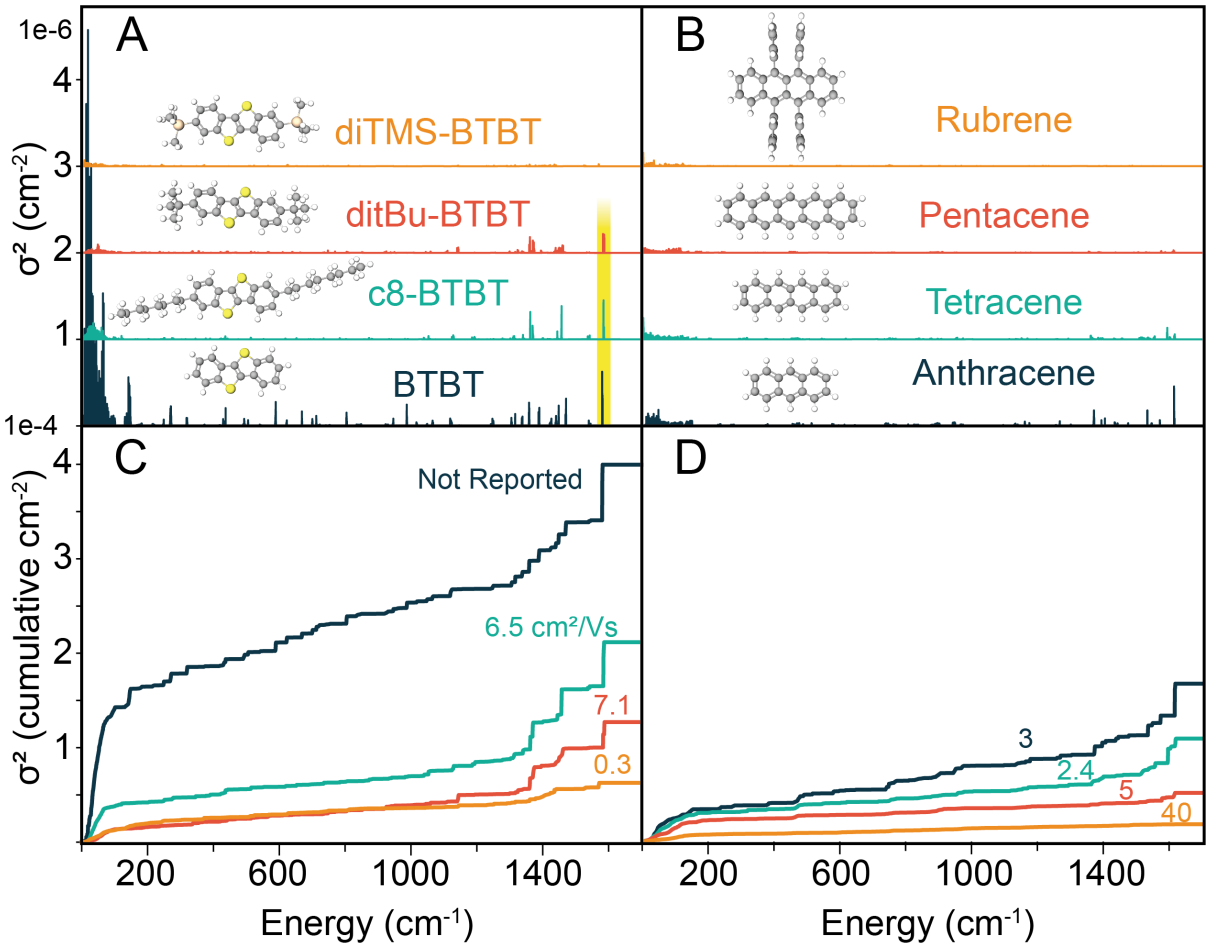

Figure 4.3. **Mode specific analysis:** The mode-wise variance, cumulative variance, and structures for BTBT, c8-BTBT, ditBu-BTBT, diTMS-BTBT, Anthracene, Tetracene, Pentacene, and Rubrene. A) shows the mode-wise variance and the molecular structure for the BTBTs: diTMS-BTBT, ditBu-BTBT, c8-BTBT, and BTBT. The highlighted peaks in ditBu, c8-BTBT, and BTBT are analyzed further in figure 4.5. B) shows the mode-wise variance and molecular structures for Rubrene, Pentacene, Tetracene, and Anthracene. C) and D) show the cumulative variance of the transfer integral for BTBTs and -acenes respectively. This is a running sum of variance with energy.

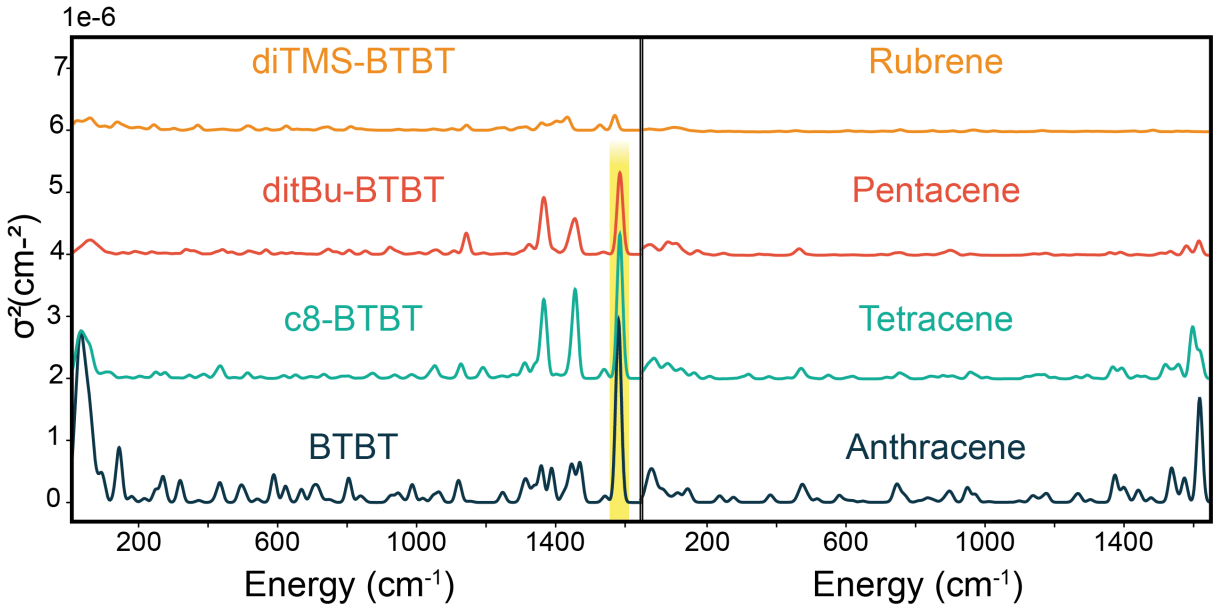

Figure 4.4. **Spectral density of the variance of the transfer integral:** (σ^2) for the BTBT-based materials as well as the -acenes. This plot is created by centering a Gaussian around each mode with a width of 5 cm^{-1} and summing them together. The result is a spectral density of the variance which helps to visualize how phonon modes in certain energy regions reduce μ. The highlighted peak in ditBu-BTBT, c8-BTBT, and BTBT is the same mode highlighted in figure 4.3a). A width of 5 cm^{-1} was chosen because it combined similar modes without broadening the spectrum dramatically.

showed that a gamma point-only analysis leads to reduced accuracy in the prediction of μ,[11] so we depict all modes across the entire Brillouin zone mesh here. Figures 4.3c and 4.3d show the cumulative contribution to σ^2. The cumulative contribution is obtained by summing each mode's contribution to σ^2 with increasing energy. The inset numbers show the highest reported μ for each material in cm^2/Vs [48–52]. BTBT reportedly sublimates spontaneously upon synthesis, so its μ has not been reported[53]. Note that μ measurements vary significantly between studies or even within a single study. As a result, these values are a rough estimate rather than a definitive measure of μ. Also, measured samples are typically multi-grain, while the effect of simulated σ^2 would only consider a single grain. Finally, summing σ^2 treats the sample isotropically while a real sample has different μ along each crystallographic axis. Because these values of μ are estimates and because σ^2 is only one factor along with J, which determines charge mobility, there is not a direct correlation between increased μ and reduced σ^2.

BTBT has by far the highest amplitude low energy modes; they overlap the plots of the other BTBTs. Regarding the energetic distribution of modes, there are apparent similarities between BTBT, c8-BTBT, and ditBu-BTBT. The most apparent similarity is the highlighted (yellow) peak just below 1600 cm^{-1}. This peak corresponds to a single mode in BTBT, c8-BTBT, and ditBu-BTBT related to the aromatic carbon-carbon stretch within the ring and is an expansion and contraction of the carbon rings within the BTBT core. This mode is also Raman active and has been used to study doping levels in some OSCs[54, 55]. By comparison, there is no equivalent phonon in diTMS-BTBT, at least not in the same energy region. No other modes in any of the other samples enable comparison of equivalent phonon modes at the same energy.

The modes at low energies generally have larger amplitudes and involve most or all of the atoms in the system. As the energy increases, the modes typically have lower amplitudes and involve fewer atoms. The low energy modes are typically thought to have a significant impact on J. BTBT fits this paradigm, and to some extent, C8-BTBT, but none of the other samples show the most significant increase in σ^2 at low energy. Additionally, is tempting to equate each peak in this analysis with a single mode. However, most of the peaks contain several tightly clustered modes. However, these tightly clustered modes are not distinguishable on this scale, which suggests that representing the phonons as a spectrum of delta functions is misleading.

Figure 4.4 shows a Gaussian convolution of the same data from figures 4.3a and 4.3b. After broadening the peaks, the plot presents a spectral density defining how much all the modes at a particular energy limit μ. The difference between figures 4.3 and 4.4 shows the weakness of the non-convolved analysis. Comparing the representation of the mode around 1600 cm^{-1}, the representation in 4.3a) appears to have low amplitude and thus a low impact on μ. However, in figure 4.4 it is clear that this mode is, in fact, important. This is because the mode near 1600 cm^{-1} demonstrates a strong phonon contribution at every q-point, while the low energy modes have large amplitude only at particular q-points. Figure C.2 shows these peaks across the Brillouin zone in detail. In contrast, when plotting the spectral density in figure 4.4, it becomes clear that the highlighted peak

is nearly as impactful as the broad low-energy peak. This is confirmed in figure 4.3c where there is a large jump in total $\boldsymbol{\sigma}^2_{mode}$ at 1600 cm^{-1}. In other words, the low energy modes are much more sensitive to their position in the Brillouin zone than the highlighted mode.

Figure C.1 shows the difference between the modes computed across the Brillouin zone and at a single q point for BTBT. While the characters of the two plots are somewhat similar, the single q-point plot misses many of the details in the full Brillouin plot. This fact, along with the information presented in figures 4.3 and 4.4 make it clear that analyzing phonon modes only at the gamma point will give an incomplete and likely incorrect picture of which modes limit μ. For this reason, it is necessary to practice caution when using this type of analysis technique and always compute phonon modes across the entire Brillouin zone.

Figure 4.5 shows a mode-specific analysis ($\boldsymbol{\sigma}^2_{mode}$) of the featured mode in BTBT (A), c8-BTBT (B), and ditBu-BTBT (C). As in figure 4.2, we show ∇J and Q_l for each molecule. The mode's amplitude is largest in BTBT, as seen in the second column. However, by dividing the amplitude by 15, as seen in the third column, it is clear that this mode has the same motion in all three materials. The attachment of side chains has reduced the degree of dynamic disorder for this mode by a factor of 15. Note that this is one of the most important modes limiting charge transport, as evidenced by the intensity in figure 4.4. We can learn several things from a comparative analysis of this mode. First, it is not a long-axis mode, yet it strongly contributes to a reduction in μ. Second, the side chains dampened this motion by roughly a factor of 15. Third, 1600 cm^{-1} is ¿5kT, but this mode contributes strongly to σ^2. The Boltzmann factor is considered in equation 3, which implies that the higher energy peaks are important because of mixing with lower energy phonons,[56, 57]. However, this has not been proven for organic samples.

A mode-by-mode analysis for any other mode that did not show identical motions at identical energies would be exceedingly tricky and subject to various subjective choices. This is because every other peak in figures 4.3 and 4.4 contains many different modes. This peak was the only mode with the same motion in all three materials at similar energies. For emphasis: studying the spectral density and looking at modes that form prominent

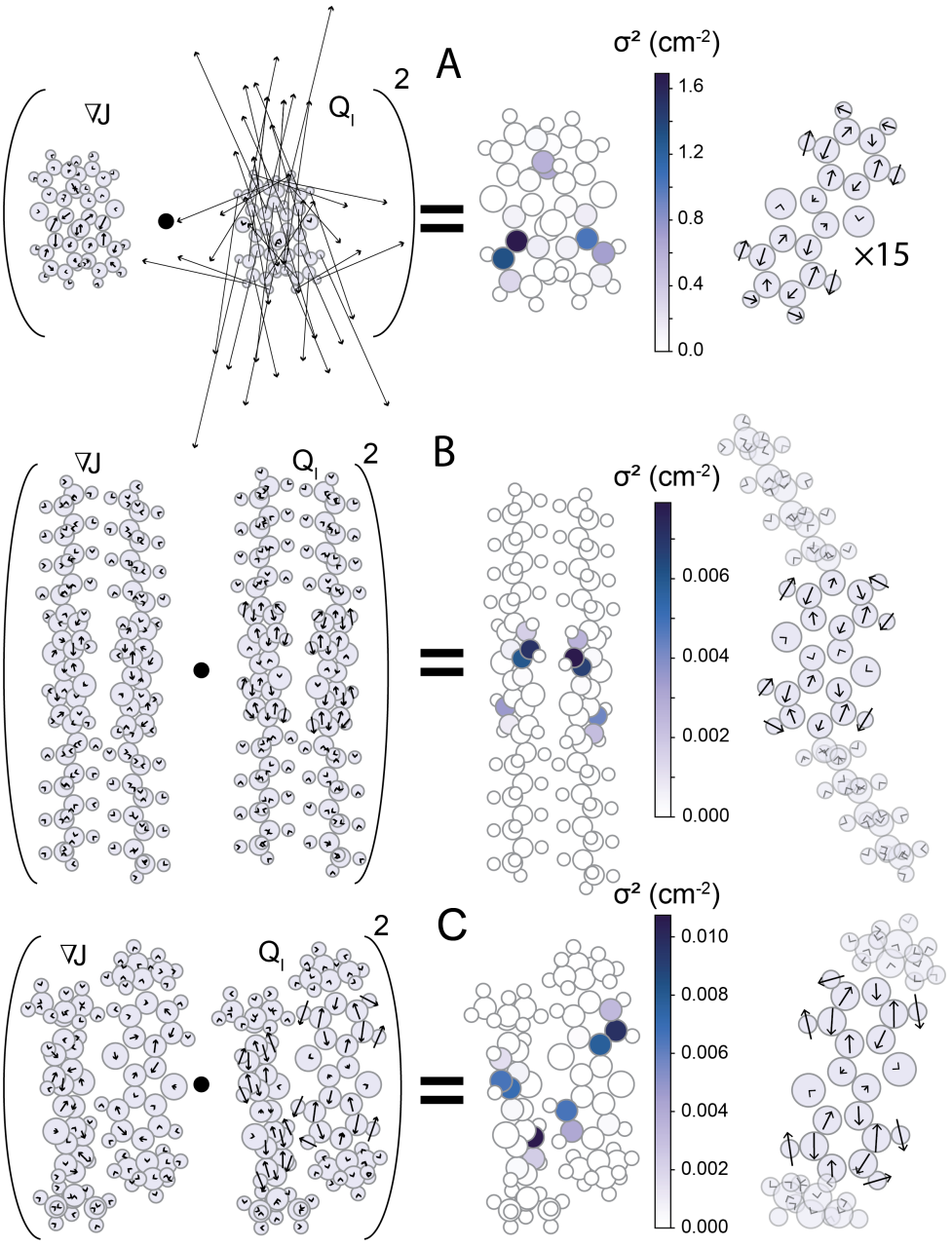

Figure 4.5. **Comparing σ^2_{mode} between molecules:** This is a visualization for how the phonon mode below 1600 cm^{-}1 is expressed in BTBT (A), c8-BTBT (B), and ditBu-BTBT (C). The left of A, B, and C shows per atom vector representations of ∇J and Q. Their squared dot product is represented as a color map of σ^2_{atom} in the center. On the right is a vector picture of the atomic displacements. The side chains are greyed for c8-BTBT and ditBu-BTBT and the length of the vectors is divided by 15 for BTBT. Only a single molecule is presented because the vectors are identical for each molecule in the pair.

peaks is not a path toward new synthetic design rules. Even when using a spectral density and phonons across the entire Brillouin zone, individual peaks rarely correspond to single modes. Moreover, the spectral density can change dramatically depending on the width of the Gaussian used. Comparisons like the one presented in figure 4.5 are complicated to find if they exist at all–even for structurally similar molecules.

4.4.2 Atomic Analysis

Figure 4.6 shows a novel analysis of the per-atom contribution to the variance of the transfer integral for the BTBT series of high μ molecules.[48, 58, 59] The color scale represents a quantitative comparison of how much each atom limits μ. All three unique molecular pairs are depicted and the numbers inset are the transfer integrals (J) of each pair in units of cm^{-1}. There is an apparent similarity in the atoms that reduce μ between BTBT, c8-BTBT, and ditBu-BTBT. The atoms which contribute most are carbon atoms that form an unbroken diagonal across the BTBT segment. As expected from figure 4.3, there is a substantial reduction in the magnitude of the contribution across these diagonals for c8-BTBT and ditBu-BTBT compared to BTBT, consistent with the higher μ in the side chain substituted molecules.

The traditional explanation for how c8-BTBT and ditBu-BTBT perform better is that they damp out a "long-axis" phonon mode represented in motion of the whole core vertically.[9, 58, 60, 61] The analysis presented here paints a more complex picture. If a long-axis mode–or many long-axis modes–were most impactful, the most significant atoms would form a line along the long axis. However, because we do not see this, we can conclude that it is a combination of modes that move the backbone in various ways that limit μ. The diagonal line of atoms across the center of the BTBT core suggests that phonon modes that bend or twist the central core of the multi-ring BTBT structure have the largest effect on reducing μ. Attaching side chains along the long axis improves μ by reducing the magnitude of core atom molecular motion both in and out of the plane.

diTMS-BTBT does not follow this trend because adding Silicon to the side chains significantly disrupts the crystal structure. BTBT, c8-BTBT, and ditBu-BTBT are monoclinic, while diTMS-BTBT has a triclinic crystal structure, resulting in lower J for the

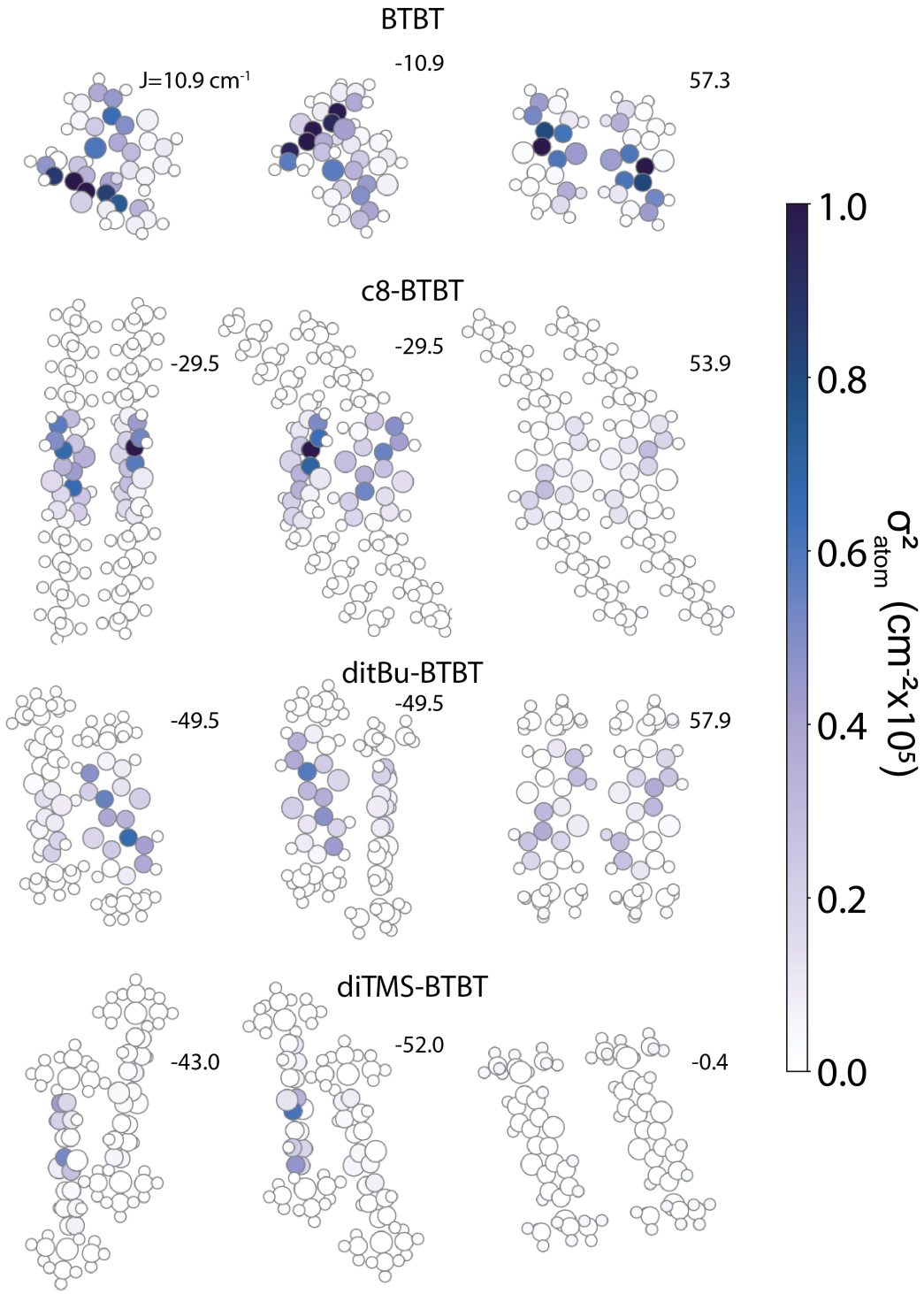

Figure 4.6. $\boldsymbol{\sigma^2_{atom}}$ **comparison for BTBT molecules:** Depicted are the unique molecular pairs for BTBT, c8-BTBT, ditBu-BTBT, and diTMS-BTBT. The color scale quantitatively represents the degree that each atom in each pair reduces μ. The inset numbers are the average transfer integrals for each pair in cm^{-1}.

third pair compared to the monoclinic BTBT's. Thus, it is more difficult to compare directly. One observation for diTMS-BTBT in the highly coupled directions is that only one of the two molecules has atoms with high σ^2. Also, the high σ^2 atoms on the BTBT core are separated by two carbons with very low σ^2. The similarity remains, however, that atoms toward the center of the BTBT unit are still the most important for the reduction of μ, and there is no indication that a long axis motion dominates the dynamic disorder.

Figure 4.7 shows the visualization of the per-atom contribution to the variance of the transfer integral for the -acenes. In the transition from anthracene to tetracene and pentacene, similar atoms are the most intense–those that form a line along the long axis on the side with the nearest molecular neighbor. The intensities significantly reduce as the -acene increases in length. This aligned intensity indicates that long-axis motions play a role in reducing μ in this series, but the full story is more complex. Increasing the length of the -acene increases the molecule's mass and thus reduces all types of dynamic disorder. Simultaneously, increasing the -acene length increases its conjugated area, which increases the nearest neighbor coupling. It appears that increasing the backbone length to hexacene or heptacene would increase nearest neighbor coupling while reducing dynamic disorder. However, as has been shown, increasing the length also reduces the solubility leading to smaller domains and also reduces the stability due to Diels-Alder reactions with nearest neighbors.[62–64]

Comparing unsubstituted acenes with rubrene is less straightforward. The addition of the side chains radically changes the crystal structure. The change in crystal structure dramatically increases the transfer integral in the c-pair direction. However, the crystal structure and change in coupling alone do not explain the improved performance of rubrene. The dynamic disorder analysis shown here also reveals that rubrene has a remarkably low variance in every molecular pair, especially when compared to the transfer integral.

4.4.3 Dynamic Disorder Design Rules

The detailed analysis of $\boldsymbol{\sigma}^2_{mode}$ and $\boldsymbol{\sigma}^2_{atom}$ reveals unprecedented information that can explain why a particular molecule with a particular crystalline motif has either higher

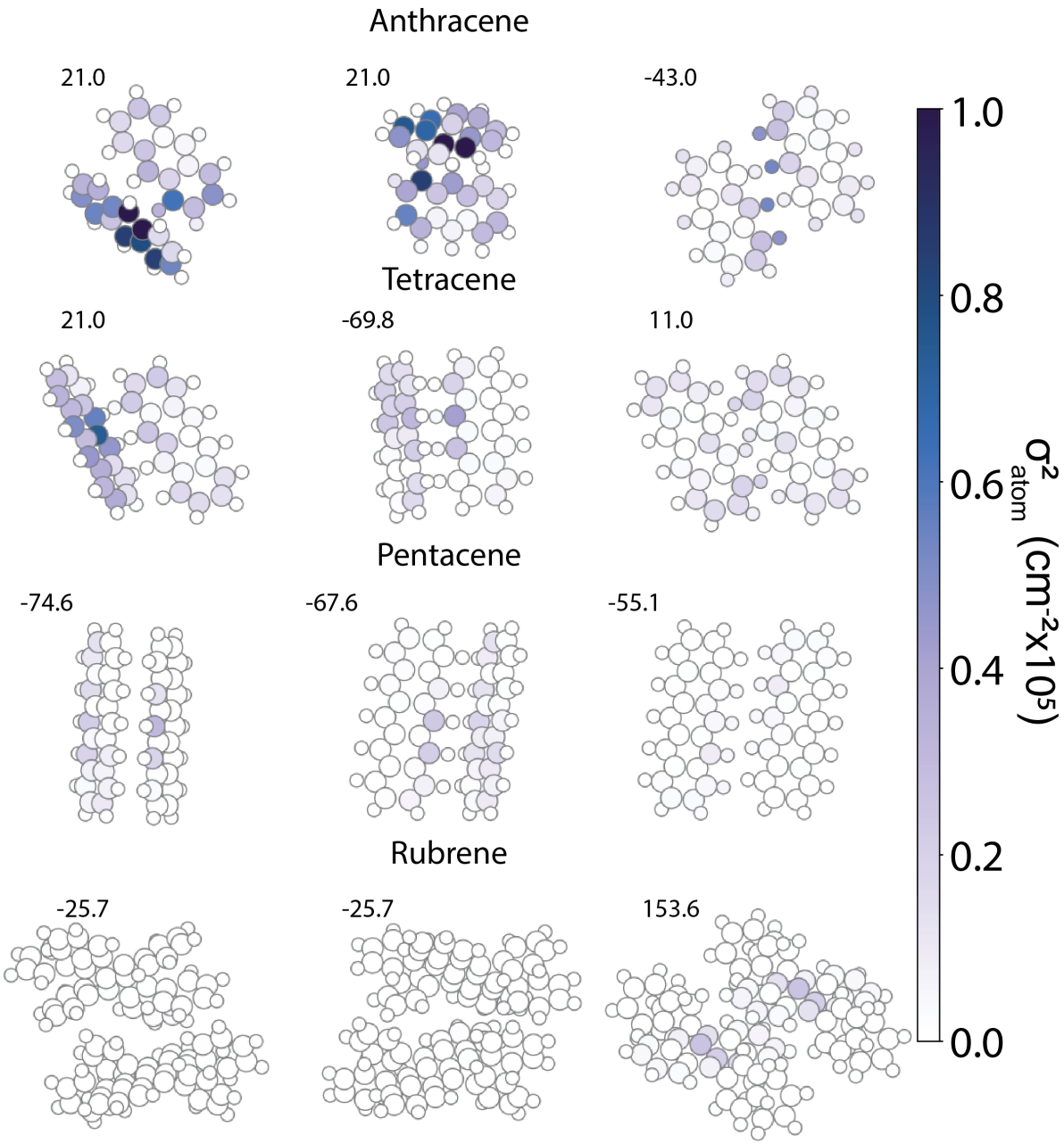

Figure 4.7. $\boldsymbol{\sigma^2_{atom}}$ **comparison of -acene molecules:** Depicted are the unique molecular pairs for anthracene, tetracene, pentacene, and rubrene. The color scale quantitatively represents the degree that each atom in each pair reduces μ. The inset numbers are the average transfer integrals for each pair in cm^{-1}.

or lower μ. This glut of information cannot be directly translated into simple synthetic design rules for new and improved organic semiconductors. However, we can articulate a series of lessons learned regarding accurate simulation and depiction of dynamic disorder and extract some hints to improve synthetic design.

Before addressing accurate simulation and visualization of dynamic disorder, it is first necessary to simulate all phonon modes. Using only gamma point modes will misrepresent and undercount the phonon contribution to dynamic disorder. It is also necessary to consider the entire energy spectrum of modes even far above kT because, at room temperature, the low energy modes can couple to higher energy modes, as was shown for the BTBT series. It is more accurate to depict the phonon mode spectrum or variance spectrum with some broadening because high amplitude, low energy modes are often only relevant at a single q-point. In contrast, higher energy modes could have lower amplitude but be relevant at all q-points. Finally, focusing on specific modes in specific molecules is seductive since the mode analysis points out which dynamic modes most reduce μ. However, this approach is doomed to fail because (1) it draws attention to particular modes that are not universally represented, (2) simulations that are not validated to data may be incorrect, and (3) just identifying the problem does not suggest a logical solution.

A more rational approach to improving μ through molecular design is to focus on a combination of increasing J coupling while simultaneously reducing total σ^2. The atom-specific analysis of transfer integral variance enables a comparison of how specific atomic structure and crystal motif changes can reduce atomic and summed (molecular) variance. However, a single analysis does not provide a guide for how changes in molecular design affect $\boldsymbol{\sigma}^2_{atom}$. Instead, it is necessary to compare several structures and then extract design hints from the comparison. For example, looking at the BTBT series, adding a side chain has the same effect between c8-BTBT and ditBu-BTBT. This suggests that further altering symmetric side chains in this position to create the same crystal structure is a waste of time. Another comparative observation from the BTBT series comes from diTMS-BTBT. This side chain caused this molecule to have a split between the high variance atoms on the BTBT. Although the transfer integral (J) was lower for diTMS-

BTBT, the μ is still high because the center of the BTBT core had little σ^2_{atom}. Perhaps a design motif could be to design new structures that split the high σ^2_{atom} to different ends of the conjugated core. The acene series shows that more extended conjugated cores increase J while reducing σ^2, which was already known. Rubrene and tips-pentacene suggest that solubility groups perpendicular to the long axis lock in high J with low σ^2. Again, this design theme was discovered empirically, and the analysis shown here only confirms what is known. Nevertheless, the computational tools presented here, DCS-flow combined with ElPh, enable a facile visualization and systematic approach to phonon engineering in organic semiconductors.

4.5 Conclusions

It is well known that dynamic disorder limits μ in organic semiconductors. More precisely, μ is increased by more electronic coupling between neighboring molecules and reduced by the variance of the transfer integral. We present here a new workflow, ElPh, designed to simulate and visualize the electron-phonon coupling for molecular crystals. ElPh combines several disparate, non-standardized processes into a standardized, reproducible simulation that can be used with various calculators. Using ElPh along with previously developed DCS-Flow, which accurately simulates the phonon modes, we compute the electron-phonon coupling and variance of this coupling for BTBT, c8-BTBT, ditBu-BTBT, diTMS-BTBT, anthracene, tetracene, pentacene, and rubrene. The variance cannot be quantitatively compared between molecular crystals since each structure has a different number of atoms. ElPh provides a means to visualize and compare the effect of coupling variance between molecules by visualizing the energetic spectrum of variance (the mode analysis) and the contribution of each atom in a molecular crystal (the atom analysis).

Using the two series of materials –acenes and BTBTs– this article analyzes how a mode analysis or an atom analysis of the variance can explain the observed μ. From these analyses, we gain deep insight into the difficulties of accurately computing variance, lessons that can be learned from a mode analysis, and insights gained from an atomic

analysis. Accurately calculating the phonon modes requires computations at multiple q-points throughout the entire Brillouin zone. A spectral density of transfer integral variance is a more meaningful way to display the effect of dynamic disorder because it more accurately weights the contributions from modes present in multiple q-points compared to gamma point modes. In addition, simulation through the entire energy range and validation to measured data significantly improve the quality of these calculations.

Accurate mode-wise analysis of the transfer integral variance provides insight into the energy distribution over which dynamic disorder reduces μ. However, this analysis is unable to tie this distribution to molecular design choices because it is nearly impossible to compare modes between different molecules. For example, BTBT contains 18424 mode samples while c8-BTBT contains 55272 mode samples at the $8 \times 8 \times 8$ mesh sampling used here. Moreover, this technique cannot help discover design rules because it does not tie the intensity of each peak to anything other than energy.

An atomic mapping of the variance of the transfer integral enables a quantitative comparison between different molecular structures. By comparing similar molecular crystals, differences in the contribution to the variance of the transfer integral can be used to make logical decisions about new synthetic design rules. In the case of the BTBTs, the addition of side chains dampened contributions to the transfer integral. However, there is still room for significant improvements. The diagonal band of high-impact atoms in figure 4.6 is still present in c8-BTBT and ditBu-BTBT. This diagonal band indicates that these side chains helped dampen all of the modes but had did not dampen them out completely. Some of the most important modes are likely a combination of short-axis or twisting modes. Thus, a wider backbone or perpendicular side chains would likely help reduce disorder. Indeed, in the case of rubrene, the presence of side chains in multiple directions was a successful strategy to dampen out many potentially problematic modes by locking the backbone in place.

We believe that an iterative approach in which synthetic chemists work in concert with computational experts will uncover more design rules and allow for improved performance from small-molecule OSCs. The combination of ElPh and DCS-Flow allows

anyone to perform the analysis presented in figures 4.6 and 4.7. Moreover, these tools can re-examine existing materials and explain why specific improvements are seen or not. Several tools exist which predict crystal structures from chemical formulas. These allow researchers to compute the properties of materials without actually producing the materials. Combining the tools and analysis presented here with structure prediction tools will enable the development of synthetic design rules for materials not yet synthesized. The tools presented here will save considerable time and material costs associated with developing new materials experimentally and will enable the comparison of simulations between groups that can be quantitatively compared using the same workflow.

Bibliography

(1) Crabtree, G.; Glotzer, S.; McCurdy, B.; Roberto, J. *Computational materials science and chemistry: accelerating discovery and innovation through simulation-based engineering and science*; tech. rep.; USDOE Office of Science (SC)(United States), 2010.

(2) Walzer, K.; Maennig, B.; Pfeiffer, M.; Leo, K. *Chemical reviews* **2007**, *107*, 1233–1271.

(3) Wang, C.; Dong, H.; Jiang, L.; Hu, W. *Chemical Society Reviews* **2018**, *47*, 422–500.

(4) Zhang, X.; Dong, H.; Hu, W. *Advanced Materials* **2018**, *30*, 1801048.

(5) Kuribara, K.; Wang, H.; Uchiyama, N.; Fukuda, K.; Yokota, T.; Zschieschang, U.; Jaye, C.; Fischer, D.; Klauk, H.; Yamamoto, T., et al. *Nature communications* **2012**, *3*, 1–7.

(6) Ciuchi, S.; Fratini, S.; Mayou, D. *Physical Review B* **2011**, *83*, 081202.

(7) Fratini, S.; Mayou, D.; Ciuchi, S. *Adv. Funct. Mater.* **2016**, *26*, 2292–2315.

(8) Harrelson, T. F. et al. *Mater. Horiz.* **2019**, *6*, 182–191.

(9) Schweicher, G.; Avino, G. D.; Ruggiero, M. T.; Harkin, D. J.; Venkateshvaran, D.; Liu, G.; Richard, A.; Ruzié, C.; Kennedy, A. R.; Shankland, K.; Takimiya, K.; Geerts, Y. H.; Axel, J.; Fratini, S.; Sirringhaus, H. *Adv. Mater.* **2019**, *31*, 1902407.

(10) Nematiaram, T.; Padula, D.; Landi, A.; Troisi, A. *Advanced Functional Materials* **2020**, *30*, 2001906.

(11) Vong, D.; Nematiaram, T.; Dettmann, M. A.; Murrey, T. L.; Cavalcante, L. S.; Gurses, S. M.; Radhakrishnan, D.; Daemen, L. L.; Anthony, J. E.; Koski, K. J., et al. *The Journal of Physical Chemistry Letters* **2022**, *13*, 5530–5537.

(12) Nematiaram, T.; Troisi, A. *Materials Horizons* **2020**, *7*, 2922–2928.

(13) Ashcroft, N. W.; Mermin, N. D., *Solid state physics*; Cengage Learning: 2022.

(14) Togo, A.; Tanaka, I. *Scripta Materialia* **2015**, *108*, 1–5.

(15) Marcus, R. A.; Sutin, N. *Biochimica et Biophysica Acta (BBA)-Reviews on Bioenergetics* **1985**, *811*, 265–322.

(16) Giannini, S.; Carof, A.; Blumberger, J. *The journal of physical chemistry letters* **2018**, *9*, 3116–3123.

(17) Ji, D.; Jiang, T.; Zheng, Y.; Sun, Y.; Wei, Z.; Li, L.; Hu, W. *Advanced Optical Materials* **2022**, *10*, 2102484.

(18) Ji, D.; Li, T.; Liu, J.; Amirjalayer, S.; Zhong, M.; Zhang, Z.-Y.; Huang, X.; Wei, Z.; Dong, H.; Hu, W., et al. *Nature communications* **2019**, *10*, 1–8.

(19) Sakanoue, T.; Sirringhaus, H. *Nature materials* **2010**, *9*, 736–740.

(20) Wang, L.; Beljonne, D. *J. Phys. Chem. Lett.* **2013**, *4*, 1888–1894.

(21) Hamilton, E. *Philosophical Magazine* **1972**, *26*, 1043–1045.

(22) Troisi, A. *Chemical Society Reviews* **2011**, *40*, 2347–2358.

(23) Fratini, S.; Ciuchi, S.; Mayou, D.; De Laissardière, G. T.; Troisi, A. *Nature materials* **2017**, *16*, 998–1002.

(24) Kohn, W.; Sham, L. J. *Physical review* **1965**, *140*, A1133.

(25) Kresse, G.; Furthmüller, J. *Computational materials science* **1996**, *6*, 15–50.

(26) Kresse, G.; Furthmüller, J. *Physical review B* **1996**, *54*, 11169.

(27) Frisch, M. J. et al. Gaussian˜16 Revision B.01, Gaussian Inc. Wallingford CT, 2016.

(28) Sutton, C.; Sears, J. S.; Coropceanu, V.; Bredas, J.-L. *The Journal of Physical Chemistry Letters* **2013**, *4*, 919–924.

(29) Kubo, T.; Häusermann, R.; Tsurumi, J.; Soeda, J.; Okada, Y.; Yamashita, Y.; Akamatsu, N.; Shishido, A.; Mitsui, C.; Okamoto, T., et al. *Nature communications* **2016**, *7*, 1–7.

(30) Dettmann, M. A.; Cavalcante, L. S.; Magdaleno, C.; Masalkovaité, K.; Vong, D.; Dull, J. T.; Rand, B. P.; Daemen, L. L.; Goldman, N.; Faller, R., et al. *Journal of Chemical Theory and Computation* **2021**, *17*, 7313–7320.

(31) Nematiaram, T.; Ciuchi, S.; Xie, X.; Fratini, S.; Troisi, A. *The Journal of Physical Chemistry C* **2019**, *123*, 6989–6997.

(32) Xie, X.; Santana-Bonilla, A.; Troisi, A. *Journal of chemical theory and computation* **2018**, *14*, 3752–3762.

(33) Cavalcante, L. S.; Daemen, L. L.; Goldman, N.; Moulé, A. J. *Journal of Chemical Information and Modeling* **2021**, *61*, 4486–4496.

(34) Elstner, M.; Porezag, D.; Jungnickel, G.; Elsner, J.; Haugk, M.; Frauenheim, T.; Suhai, S.; Seifert, G. *Physical Review B* **1998**, *58*, 7260.

(35) Lindsey, R. K.; Fried, L. E.; Goldman, N. *Journal of chemical theory and computation* **2017**, *13*, 6222–6229.

(36) Troisi, A. *Advanced Materials* **2007**, *19*, 2000–2004.

(37) Bittle, E. G.; Biacchi, A. J.; Fredin, L. A.; Herzing, A. A.; Allison, T. C.; Hight Walker, A. R.; Gundlach, D. J. *Commun. Phys.* **2019**, *2*, DOI: 10.1038/s42005-019-0129-5.

(38) Dettmann, M. madettmann/DCS-Discover: DCS Discover, version 1.1.0, 2021.

(39) Dantanarayana, V.; Nematiaram, T.; Vong, D.; Anthony, J. E.; Troisi, A.; Nguyen Cong, K.; Goldman, N.; Faller, R.; Moulé, A. J. *Journal of chemical theory and computation* **2020**, *16*, 3494–3503.

(40) Landi, A.; Troisi, A. *The Journal of Physical Chemistry C* **2018**, *122*, 18336–18345.

(41) Troisi, A.; Orlandi, G. *Phys. Rev. Lett.* **2006**, *96*, 1–4.

(42) Valeev, E. F.; Coropceanu, V.; da Silva Filho, D. A.; Salman, S.; Brédas, J.-L. *Journal of the American Chemical Society* **2006**, *128*, 9882–9886.

(43) Baumeier, B.; Kirkpatrick, J.; Andrienko, D. *Physical Chemistry Chemical Physics* **2010**, *12*, 11103–11113.

(44) Nematiaram, T.; Troisi, A. *The Journal of Chemical Physics* **2020**, *152*, 190902.

(45) Vener, M. V.; Parashchuk, O. D.; Kharlanov, O. G.; Maslennikov, D. R.; Dominskiy, D. I.; Yu. Chernyshov, I.; Yu. Paraschuk, D.; Yu. Sosorev, A. *Advanced Electronic Materials* **2021**, *7*, 2001281.

(46) Otaki, T.; Terashige, T.; Tsurumi, J.; Miyamoto, T.; Kida, N.; Watanabe, S.; Okamoto, T.; Takeya, J.; Okamoto, H. *Physical Review B* **2020**, *102*, 245201.

(47) Banks, P.; Dyer, A.; Whalley, A.; Ruggiero, M. **2022**.

(48) Wei, W.; Yang, C.; Mai, J.; Gong, Y.; Yan, L.; Zhao, K.; Ning, H.; Wu, S.; Gao, J.; Gao, X., et al. *Journal of Materials Chemistry C* **2017**, *5*, 10652–10659.

(49) Hu, P.; He, X.; Jiang, H. *InfoMat* **2021**, *3*, 613–630.

(50) Butko, V.; Chi, X.; Ramirez, A. *arXiv preprint cond-mat/0307372* **2003**.

(51) Schweicher, G.; Lemaur, V.; Niebel, C.; Ruzié, C.; Diao, Y.; Goto, O.; Lee, W.-Y.; Kim, Y.; Arlin, J.-B.; Karpinska, J., et al. *Advanced materials* **2015**, *27*, 3066–3072.

(52) Sánchez-Carrera, R. S.; Paramonov, P.; Day, G. M.; Coropceanu, V.; Brédas, J.-L. *Journal of the American Chemical Society* **2010**, *132*, 14437–14446.

(53) He, Y.; Xu, W.; Murtaza, I.; Zhang, D.; He, C.; Zhu, Y.; Meng, H. *RSC advances* **2016**, *6*, 95149–95155.

(54) Tsang, J.; Freitag, M.; Perebeinos, V.; Liu, J.; Avouris, P. *Nature nanotechnology* **2007**, *2*, 725–730.

(55) Barnes, A.; Majid, M.; Stuckey, M.; Gregory, P.; Stead, C. *Spectrochimica Acta Part A: Molecular Spectroscopy* **1985**, *41*, 629–635.

(56) Shen, Y.; Saunders, C. N.; Bernal, C. M.; Abernathy, D. L.; Manley, M. E.; Fultz, B. *Physical Review Letters* **2020**, *125*, 085504.

(57) Kim, D. S.; Hellman, O.; Shulumba, N.; Saunders, C. N.; Lin, J. Y.; Smith, H. L.; Herriman, J.; Niedziela, J. L.; Abernathy, D. L.; Li, C. W., et al. *Physical Review B* **2020**, *102*, 174311.

(58) Chung, H.; Chen, S.; Patel, B.; Garbay, G.; Geerts, Y. H.; Diao, Y. *Crystal Growth & Design* **2020**, *20*, 1646–1654.

(59) Chung, H.; Chen, S.; Sengar, N.; Davies, D. W.; Garbay, G.; Geerts, Y. H.; Clancy, P.; Diao, Y. *Chemistry of Materials* **2019**, *31*, 9115–9126.

(60) Illig, S.; Eggeman, A. S.; Troisi, A.; Jiang, L.; Warwick, C.; Nikolka, M.; Schweicher, G.; Yeates, S. G.; Henri Geerts, Y.; Anthony, J. E., et al. *Nature communications* **2016**, *7*, 1–10.

(61) Eggeman, A. S.; Illig, S.; Troisi, A.; Sirringhaus, H.; Midgley, P. A. *Nature materials* **2013**, *12*, 1045–1049.

(62) Miyazaki, T.; Watanabe, M.; Matsushima, T.; Chien, C.-T.; Adachi, C.; Sun, S.-S.; Furuta, H.; Chow, T. J. *Chemistry–A European Journal* **2021**, *27*, 10677–10684.

(63) Einholz, R.; Fang, T.; Berger, R.; Grüninger, P.; Fruh, A.; Chasse, T.; Fink, R. F.; Bettinger, H. F. *Journal of the American Chemical Society* **2017**, *139*, 4435–4442.

(64) Watanabe, M.; Chang, Y. J.; Liu, S.-W.; Chao, T.-H.; Goto, K.; Islam, M.; Yuan, C.-H.; Tao, Y.-T.; Shinmyozu, T.; Chow, T. J., et al. *Nature chemistry* **2012**, *4*, 574–578.

Chapter 5

Unpublished Work

5.1 Preamble

This chapter details work which was either unfinished or unpublished. First, I'll explain software I wrote to help clean and analyze atomic force microscopy (AFM) images. Then, I'll share some simulations of TTF-TCNQ which was ultimately unpublishable. Finally, I'll detail how I built DCS Discover, our open-source database of measured and predicted INS specta.

5.2 AFM Software

One of my first projects after joining the group was to write some software to improve AFM images. One of the main issues with raw AFM images is that they can have a systematic, semi-parabolic curve across the whole image. This makes surfaces that are mostly flat appear curved. Another common issue was that there would be large step discontinuities which were an artifact of the AFM and not a real signal. Finally, when taking AFM images of older samples, there is often dust on the sample which makes it difficult to see the underlying structure. Each of these issues was solved with a series of MatLab plugins.

Figure 5.1 demonstrates how the software is able to flatten the image and remove step discontinuities. The first step is to identify where the discontinuities are. This can be done with the aid of manual input or automatically. In my testing, it was always better

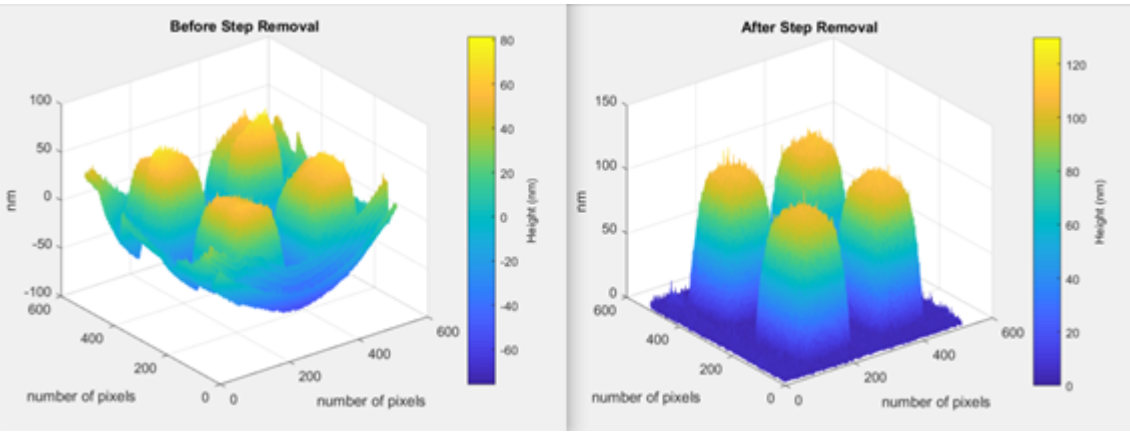

Figure 5.1. Before and after removing steps and flattening. The film is a P3HT film which has been doped through a shadow mask. Then the mask is removed and the film is submerged in solvent to dissolve the non-doped portions, resulting in bumps. This data is also presented in a publication by Jun Li et al.[1] The left shows the raw data from the AFM and the right shows the image after flattening and removing steps

with some degree of manual input. I wrote a GUI that made it possible to just click where the discontinuity was found. Then, an average per line near where the user indicated was computed. By comparing the averages between lines, it was possible to identify where the jump took place. Then the entire image following the jump was shifted by the difference in averages. This could be repeated until all of the jumps were removed.

Next, the image needed to be flattened. This had been done in the past by fitting a parabola to the spectrum. The challenge here is that the AFM image now contained features. Attempting to fit the entire spectrum to a parabola would distort the features. Instead, it was better to choose a featureless line and impose a uniform rolling average. In other words, the average for each line in the x direction would be computed. Then each line would be shifted until the average remained the same. This could not be done along the entire line, however, as the features would again interfere. Thus, manual input was required to identify a region along which there were no features. This process was repeated for the y direction. The right side of figure 5.1 shows the image on the left after removing steps and flattening. The image is also shifted so that the bottom (z-axis) is at 0nm. The software is available as matlab add-ons. It is available at [2].

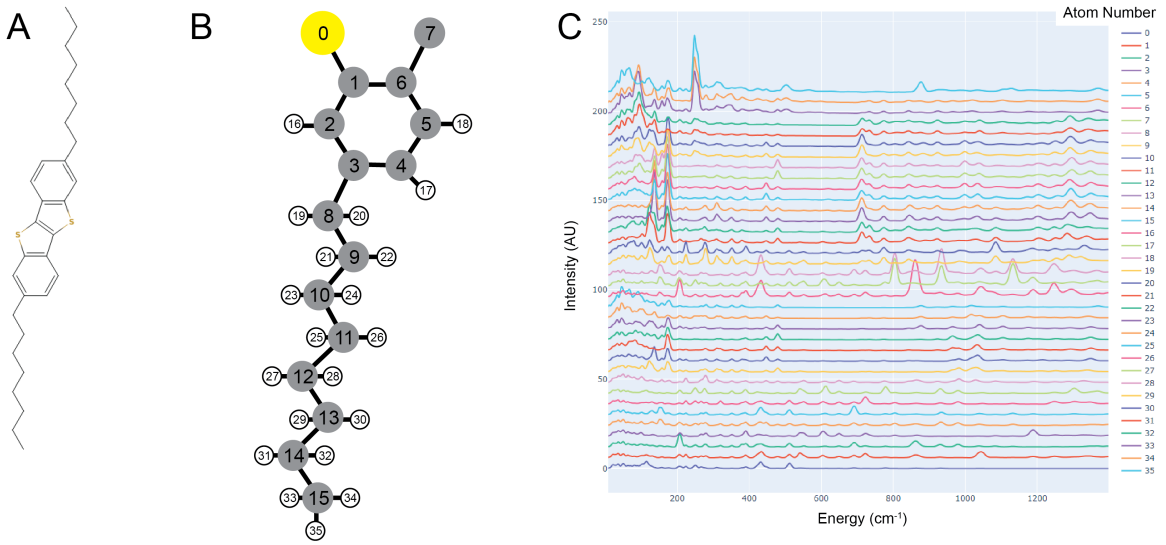

Figure 5.2. The atom-wise contribution to the INS spectrum of c8-BTBT. A shows the atomic structure of c8-BTBT. B shows the atom labels for half of c8-BTBT. C shows the contribution to the INS spectrum for each atom as numbered in B.

5.3 Isolating atomic contributions to INS spectra

I developed a method for isolating the contributions of individual atoms to an INS spectrum. After validating a computed INS spectrum by comparing it to an experimental spectrum, it is possible to decompose the individual contributions of the atoms to the complete spectrum. This is done with the help of oclimax.[3] Oclimax uses a .oclimax file to compute the INS spectrum. This file contains all of the information about the phonon modes along with the locations and cross-sections of each atom. The neutron cross-section is a measure of how much an atom interacts with neutrons. By setting this neutron cross-section to 0, we can make this atom's contribution to the INS spectrum disappear without changing anything about the phonon modes.

Figure 5.2 shows the contribution of each atom to the INS spectrum for c8-BTBT. The atoms are labeled in part B and the corresponding spectra are shown in part C. There are several notable pieces of information that are visible using this type of analysis. For instance, there is a double peak just below 200 that appears in atoms 8-15. This double peak must be related to some collection of modes involving the carbons on the side chain. Moreover, as the atom gets farther from the backbone, those peaks shift systematically

in energy. This type of analysis can also be used to group atoms and see the contribution from just the backbone, for instance. The main limitation of this analysis is that for large molecules, the amount of data is overwhelming. Thus, it is likely better to only perform atom-by-atom analysis on smaller molecules and use groups of atoms for anything larger. The code for performing this analysis is available at [4].

5.4 Comparing INS spectra

In many instances, it is helpful to compare two INS spectra. Standard comparison techniques such as subtracting spectra is unhelpful because small shifts in energy cause massive differences. Thus, an analysis technique which can account for small shifts in energy is necessary. I used Fréchet distance in my method comparison paper because it addresses this issue [5]. However, it requires arrays of equal length. This means it cannot be used to compare experimental spectra, which have an unequal distribution of points with energy, to a simulated spectra, which have evenly-distributed points with energy. Thus, a new technique was required.

The first step toward comparing similar molecules is to map the more data-dense spectrum onto the less data-dense spectrum. When comparing experimental data to simulated data, this requires mapping the experimental spectrum onto the simulated energies. This mapping is done by finding the closest experimental point in energy to a point in the simulated spectrum. This process is repeated for every point in the simulated spectrum. Now, the intensity arrays are of equal length.

The next step is to choose an analysis that can account for shifts in energy. The Fréchet distance can again be used, and my testing reveals it works quite well. This testing involved comparing every curve matching analysis I could find. Both Fréchet distance and correlation give results which match intuition and can be performed in a reasonable amount of time. Another technique is to compute the correlation coefficient. The correlation coefficient is used in a variety of applications including in investment analysis, which is where I found inspiration. In investment analysis, the correlation coefficient explains to which degree two stocks follow the same trends. The correlation coefficient is defined

in section B.0.1. I created a small library for computing correlation between two INS spectra. It also has some tools for easily reading and plotting both experimental and computed INS spectra [6].

5.5 TTF-TCNQ

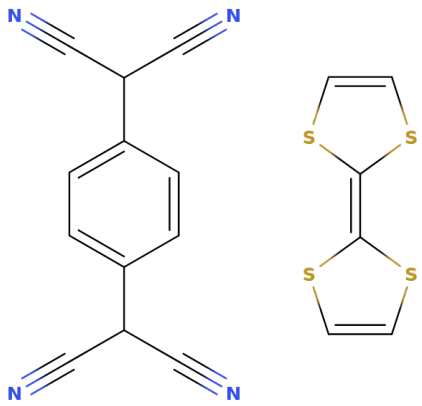

Figure 5.3. The chemical structure of TTF-TCNQ.TCNQ is the left molecule and TTF is on the right. Together, they form the salt TTF-TCNQ

TTF-TCNQ is a charge transfer salt made up of two small molecules, TTF and TCNQ. Figure 5.3 shows the chemical structure of TTF-TCNQ. At 54K and 38K, it undergoes two electronic spin coupling transitions in which the electronic transport properties change wildly. It is theorized that a subtle structural transition takes place at these two temperatures as well. The structural change is that neighboring molecules "pair" up, making the energetic landscape more difficult for charge transport. We hoped that by using INS, we could spot some differences between the phonon modes at different temperatures and correlate this to structural changes. Figure 5.4 shows experimental INS spectra for TTF-TCNQ at 5K, 38K, and 75K. We also collected INS data for TTF and TCNQ alone. There are slight differences between the spectra, but they are subtle.

We performed several computations of the INS spectrum to try and explain the subtle

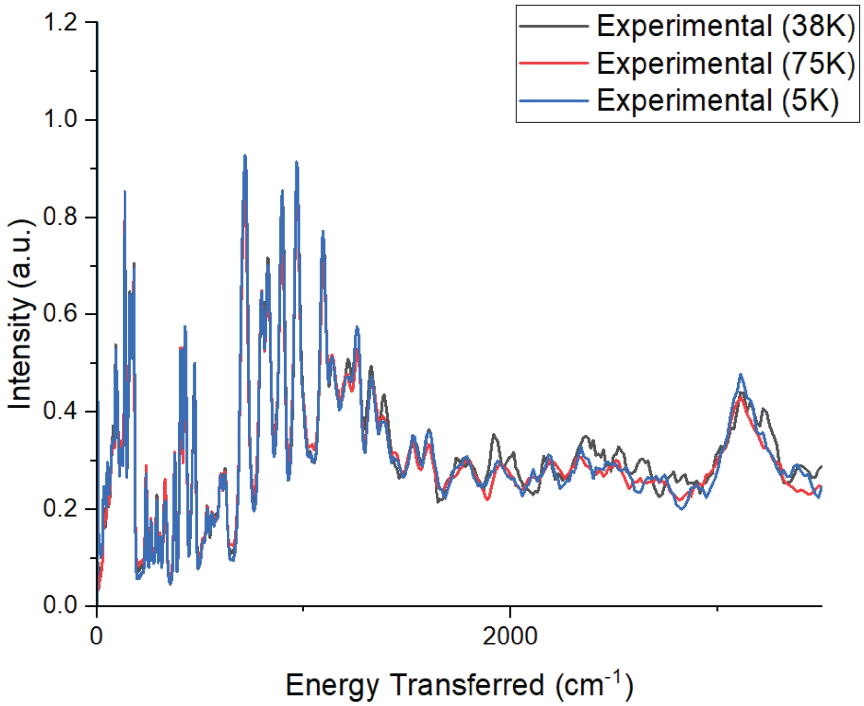

Figure 5.4. Experimental INS of TTF-TCNQ. Data was taken at 5 Kelvin, 38 Kelvin, and 75 Kelvin.

differences between the spectra. Figure 5.5 shows the predicted spectra computed at the gamma point or throughout the full Brillouin zone at 0K, 5K, 38K, and 75K. Once again, there are subtle differences due to the Debeye-Waller factor, which accounts for the effect of temperature on neutron scattering. The differences are subtle, except for the low-energy region where the gamma point simulation is significantly different than the full Brillouin zone calculations.

We experimented with other starting configurations for TTF-TCNQ and larger box sizes but ultimately concluded that we were unable to identify the causes of the extremely subtle differences between the spectra at different temperatures. We later applied this same strategy to MOFs and were successful because the differences between spectra were more prominent. This will always be an issue with this project. It is impossible to know whether the experiment will reveal a difference in the dynamics before taking the data.

We also tried to find connections between the INS spectrum for TTF-TCNQ and the spectra for TTF and TCNQ individually. We did this by computing INS spectra for a

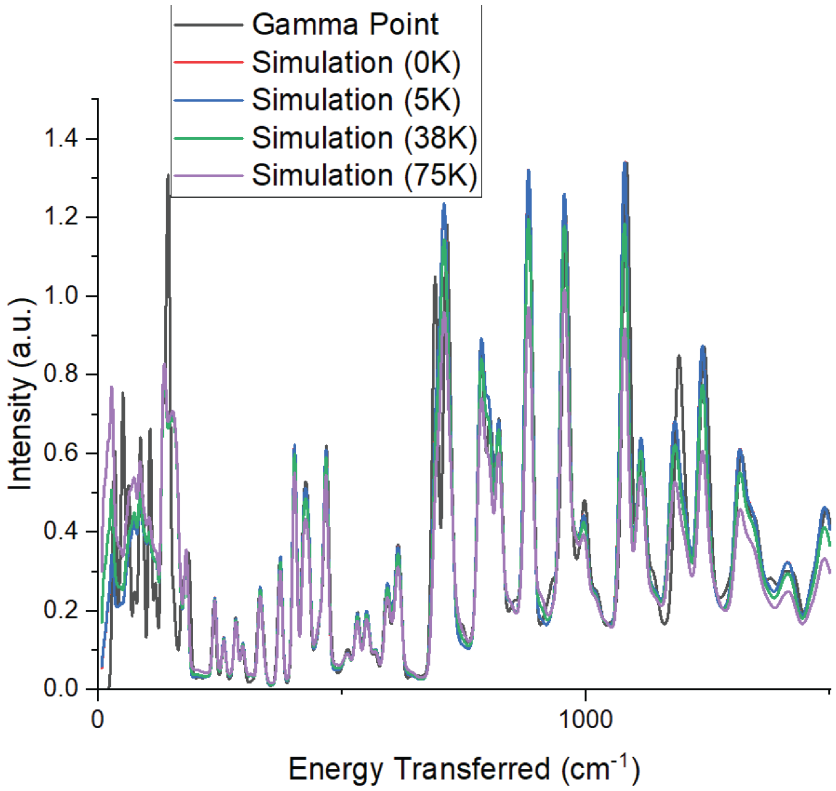

Figure 5.5. Simulated spectra of TTF-TCNQ at the gamma point throughout the full Brillouin zone at 0K, 5K, 38K, and 75K.

variety of structures of TTF and TCNQ. We also computed INS spectra for TTF and TCNQ in the same arrangement that they are in when part of TTF-TCNQ. This also failed to reveal anything substantial.

Since we had the data anyway, we also performed a transfer learning study on TTF-TCNQ and TCNQ. In this study, we wanted to see whether we could train ChIMES on TCNQ and apply it to TTF-TCNQ. We also wanted to do the reverse: train on TTF-TCNQ and apply it to TCNQ. Figure 5.6 shows the experimental INS spectrum for TTF-TCNQ (blue) along with a number of computed spectra. DFT shows the best agreement and DFTB shows a loss in accuracy. ChIMES is able to recover quite a bit of accuracy for the model trained on TTF-TCNQ while the model trained on TCNQ shows worse agreement.

Figure 5.7 shows the experimental INS spectrum for TCNQ (blue) along with a number of computed spectra. DFT shows the best agreement with the experiment while DFTB

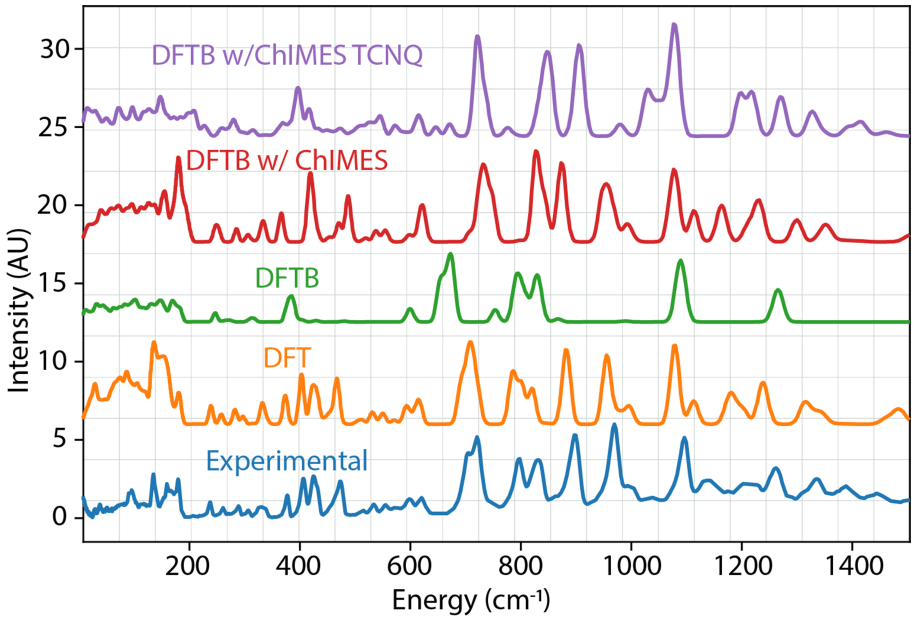

Figure 5.6. Experimental INS spectrum (blue) of TTF-TCNQ along with INS spectra computed using DFT (orange), DFTB (green), DFTB with ChIMES trained on TTF-TCNQ (red), and DFTB with ChIMES trained on TCNQ (purple).

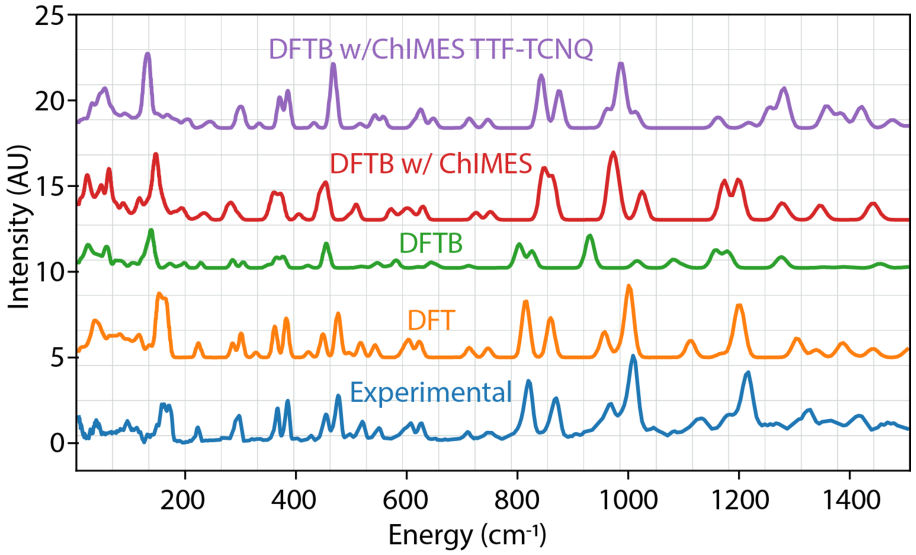

Figure 5.7. Experimental INS spectrum (blue) of TCNQ along with INS spectra computed using DFT (orange), DFTB (green), DFTB with ChIMES trained on TTF-TCNQ (red), and DFTB with ChIMES trained on TTF-TCNQ (purple).

	Applied to TCNQ	Applied to TTF-TCNQ
Trained on TCNQ	0.198	0.144
Trained on TTF-TCNQ	0.208	0.151

Table 5.1. Correlation coefficient between the experimental INS spectrum and the INS spectrum computed using DFTB/ChIMES trained on both TCNQ and TTF-TCNQ. A higher values corresponds to better agreement between spectra.

shows the worst agreement with the experiment. In both cases, ChIMES recovers some of the accuracy of DFT, but the model trained with TTF-TCNQ appears slightly more accurate than the model trained with TCNQ. This result is surprising because a model trained on TCNQ alone would be expected to outperform a model trained on a different molecule. However, the fact that training on a larger molecule improved performance indicates that training a single model on many molecules might be a good strategy to create more versatile models.

To confirm the qualitative results that TTF-TCNQ creates a better training set for both molecules, we computed the correlation coefficient for all 4 spectra predicted using DFTB/ChIMES. Table 5.1 shows the correlation coefficient for both TCNQ and TTF-TCNQ trained using TCNQ and TTF-TCNQ. The model trained on TTF-TCNQ was better at predicting an INS spectrum in both TCNQ and TTF-TCNQ. This agrees with the qualitative assessment above. In conclusion, when designing a system for training, it is better to train with a larger, more complex system than a smaller, less complex system.

5.6 INS spectra from MD trajectories

The most recent version of OCLIMAX makes it possible to compute an INS spectrum from an MD trajectory [7]. Thomas Harrelson from the Moulé group also published a method for computing an INS spectrum from an MD trajectory [8]. This method offers a modest improvement over the OCLIMAX implementation because it is able to include the Debeye-Waller factor and includes q dependence. Both methods are ideal for amorphous or semi-crystalline samples because it is possible to sample more configurations than the finite displacement method. Moreover, it is possible to use barostats and thermostats to

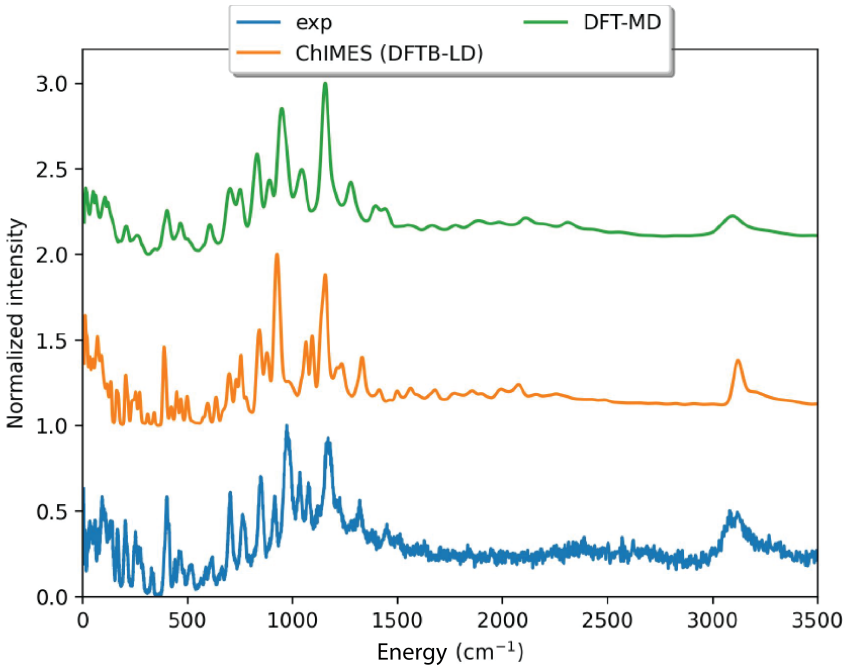

Figure 5.8. INS spectrum of amorphous rubrene. The experimental spectrum is shown in blue. Orange shows an INS spectrum computed with DFTB and ChIMES trained on rubrene with the finite displacement method. The orange line is from a perfectly crystalline model. The green line is from an NVT DFT-MD trajectory with 25,000 steps at 500K

sample morphologies unavailable at 0K.

Figure 5.8 shows an INS spectrum computed from a DFT-MD trajectory (green) and the finite displacement method with DFTB/ChIMES (orange) compared to an experimental INS spectrum of an amorphous sample. The spectrum from the DFT-MD trajectory shows good agreement with the experimental spectrum. This demonstrates that this technique can be useful for non-crystalline materials. It's also worth noting that this particular sample seemed to have quite a bit of mid-range order which is why the crystalline model also shows good agreement with the experiment.

A paper from Kubo et al., strain is induced on a small-molecule OSC [9]. This squeezes the backbones of the molecules closer together, increasing orbital overlap and increasing mobility. It is impossible to study a system under strain with the finite displacement method because the molecule would return to it's lowest-energy configuration after relaxing. Thus, the MD-based technique would be ideal for this type of sample.

5.7 DCS Discover

In order to share our results more broadly, I created DCS discover [10]. DCS discover is a mobile-first repository of our experimental and simulated INS spectra. The web app allows users to learn about the project, interact with the data directly in their browser, and download any of our data. I created the web app twice and learned a lot about these types of projects in the process. I hope to share some lessons I learned to help others who wish to create and deploy similar projects

The first time I built DCS discover, I used django for the backend and vanilla javascript for the frontend. I chose django because I was experienced with python as possible and wanted to do as much of the computation with python. I also chose a SQL database because it was the database architecture I was most familiar with. I designed the app to build a separate page for each molecule in the database and a main explore page which had each of the molecules. I used vanilla javascript because I had no experience with frontend libraries.

I developed the web app locally and everything worked well until it was time to deploy. I deployed the app using google cloud app engine and hosted the SQL database using google cloud SQL. After launching the app, it was extremely slow to load even the explore page. Even though the app and sql server were both hosted in California, where I was attempting to access the app from, page load times were nearly a minute in length. Moreover, the SQL server cost $50 per month for an app I believed would have very few monthly users. All of this was unacceptable in the end.

When I rebuilt the app, I had learned my lesson. While I was experienced with python, I did not have the backend experience to reduce load times. Instead of django, I opted for google firebase which is a backend-as-a-service. Firebase makes it possible to ship an extremely responsive app without extensive technical experience deploying web apps. I also switched from an SQL database to a no-SQL database. This was ideal because no-SQL databases do not require a constantly-running server. Instead, data is just stored in .json files and can be accessed on-demand. For apps which have a low number of users, this is ideal for cost and efficiency.

I also used the React web framework for the frontent. React has a steep learning curve, but it makes it easy to build responsive apps. I also used a modal (a kind of popup) to display the data for each material rather than a separate page. This meant I only had to load the discover page once. Each time a new material was selected, I just updated that part of the app rather than loading a whole new page.

Switching to firebase and React drastically lowered my page load times. It also lowered the monthly cost to $0 because it fell under the firebase free tier for both storage and hosting. In general, I learned it was better to use the best tools for the job rather than the tools I was most familiar with.

Bibliography

(1) Li, J.; Holm, D. M.; Guda, S.; Bedolla-Valdez, Z. I.; Gonel, G.; Jacobs, I. E.; Dettmann, M. A.; Saska, J.; Mascal, M.; Moulé, A. J. *Journal of Materials Chemistry C* **2019**, *7*, 302–313.

(2) Dettmann, M. A. Madettmann/AFM-Apps: A Collection of Matlab plugins for fixing AFM Images, 2022.

(3) Cheng, Y. Q.; Daemen, L. L.; Kolesnikov, A. I.; Ramirez-Cuesta, A. J. *J. Chem. Theory Comput.* **2019**, *15*, 1974–1982.

(4) Dettmann, M. Madettmann/mode-analysis: A collection of scripts for analyzing atomic contributions to INS Spectra, 2022.

(5) Dettmann, M. A.; Cavalcante, L. S.; Magdaleno, C.; Masalkovaité, K.; Vong, D.; Dull, J. T.; Rand, B. P.; Daemen, L. L.; Goldman, N.; Faller, R., et al. *Journal of Chemical Theory and Computation* **2021**, *17*, 7313–7320.

(6) Dettmann, M. Madettmann/correlate-spectra: A small library for loading, plotting, and computing correlation between different INS spectra, 2022.

(7) Cheng, Y.; Kolesnikov, A. I.; Ramirez-Cuesta, A. J. *Journal of Chemical Theory and Computation* **2020**, *16*, 7702–7708.

(8) Harrelson, T. F.; Dettmann, M.; Scherer, C.; Andrienko, D.; Moulé, A. J.; Faller, R. *Sci. Rep.* **2021**, *11*, 1–12.

(9) Kubo, T.; Häusermann, R.; Tsurumi, J.; Soeda, J.; Okada, Y.; Yamashita, Y.; Akamatsu, N.; Shishido, A.; Mitsui, C.; Okamoto, T., et al. *Nature communications* **2016**, *7*, 1–7.

(10) Dettmann, M. madettmann/DCS-Discover: DCS Discover, version 1.1.0, 2021.

Appendix A

SI for Comparing the expense and accuracy of methods to simulate atomic vibrations in rubrene

A.1 DFT

For the DFT simulation, the VASP package was used with the opt-pbe functional, a cutoff energy of 520 eV, and a k-point sampling of 2x2x2 across all calculations. A full optimization was performed (lattice and atomic positions) with a maximum force criteria of 0.02 eV/Å. In order to calculate the phonon modes, the finite displacement method was used with a 1x1x1 supercell.

A.2 DFTB

For the DFTB simulation, we performed the calculations with the mio1-1 Slater-Koster parameters and a similar criteria of k-point sampling and optimization as the DFT simulation. Furthermore, using the same method of phonon calculation as before, we set a 2x2x2 supercell.

A.3 DFTB/ChIMES

The best DFTB/ChIMES simulation began with a full structure optimization. Next a DFT-MD simulation was performed for the modeling step. VASP was with the same

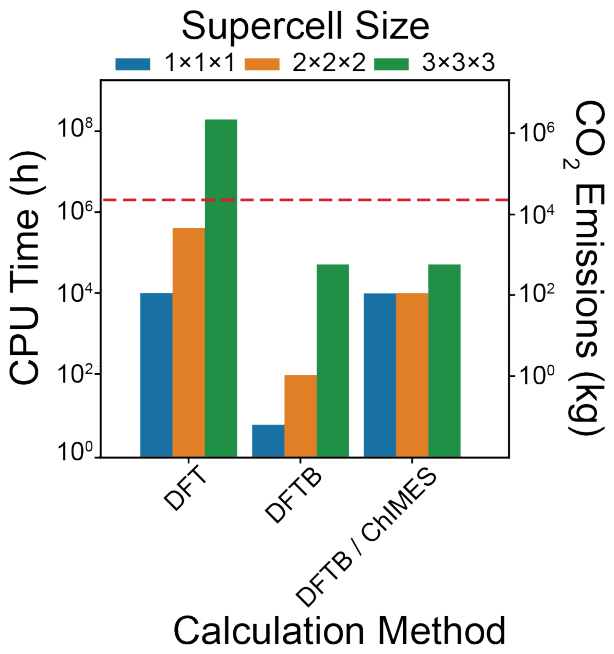

Figure A.1. CPU time for the three most accurate methods for a variety of box sizes. The actual box sizes used were 1x1x1 for DFT and 2x2x2 for DFTB and DFTB/ChIMES. The other values were estimated using the scaling law for each method (N^3). The values for DFTB with ChIMES include additional training. The dashed red line represents the yearly allocation for our group (2 million NERSC hours)

conditions as before, but with the PBE functional. The MD simulation was performed considering the canonical ensemble [NVT] with a trajectory integrated at 1000K with a 0.20 fs time step and the Nosé-Hoover thermostat with periodic boundary conditions. The DFT-MD simulation had in total a duration of 5 ps from which uniformly spaced frames were extracted every 100 fs producing a training set of 50 configurations. The ChIMES coefficients were fit to the training set for two body interactions up to the 8th order and three body interactions up to the 4th order. The remaining steps of the workflow were performed using DFTB/ChIMES imposing the same set of parameters for the optimization and phonon calculation as the non-corrected DFTB simulation.

Figure A.2 shows the effect of order of 2- and 3-body interactions on the predicted INS spectrum. In this case, 8th- and 4th-order 2- and 3-body interactions showed a better fit than 16th- and 8th-order interactions. This indicates that the larger order model may have been overfit. In the region between 800 $cm^{-1}|$ and 1000cm^{-1}, the lower order model correctly predicts three peaks while the larger order predicts four. In this study, 2-body

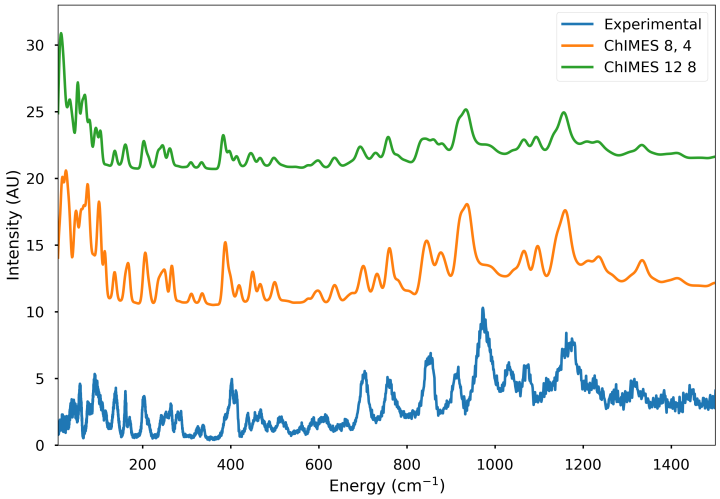

Figure A.2. Comparison between two ChIMES parametrizations. The orange line was produced from a ChIMES model which used up to 8th order 2-body interactions and up to 4th order 3-body interactions. The green line was produced using a ChIMES model with up to 16th order 2-body interactions and up to 8th order3-body interactions.

interaction orders were varied from 4th to 16th and 3-body interaction orders were varied from 2nd to 8th. The 8-4 model was the most successful of all.

A.4 ML

ML was also employed to compute INS spectra. The atomistic machine learning package (AMP) along with the atomic simulation environment(ASE) was used to train a neural net to predict the forces and energies in Rubrene. The same training set used for forcebalance was used for the ML method and the Gaussian descriptor was used. First, the effects of neural net architecture were investigated. Figure A.3 shows the time required to train each neural net so that the force root mean square error (RMSE) was 0.5 eV/Å. The 8x8 neural net showed the fastest convergence, so it was then trained until the maximum accuracy was achieved.

The effect of the width ν in the Gaussian descriptor was also investigated. The width was quartered, halved, doubled, and quadrupled to determine the best width. It was found that a width twice as large as the default was able to achieve the highest convergence. The force RMSE for the best result achieved is shown in figure A.4. The final RMSE was

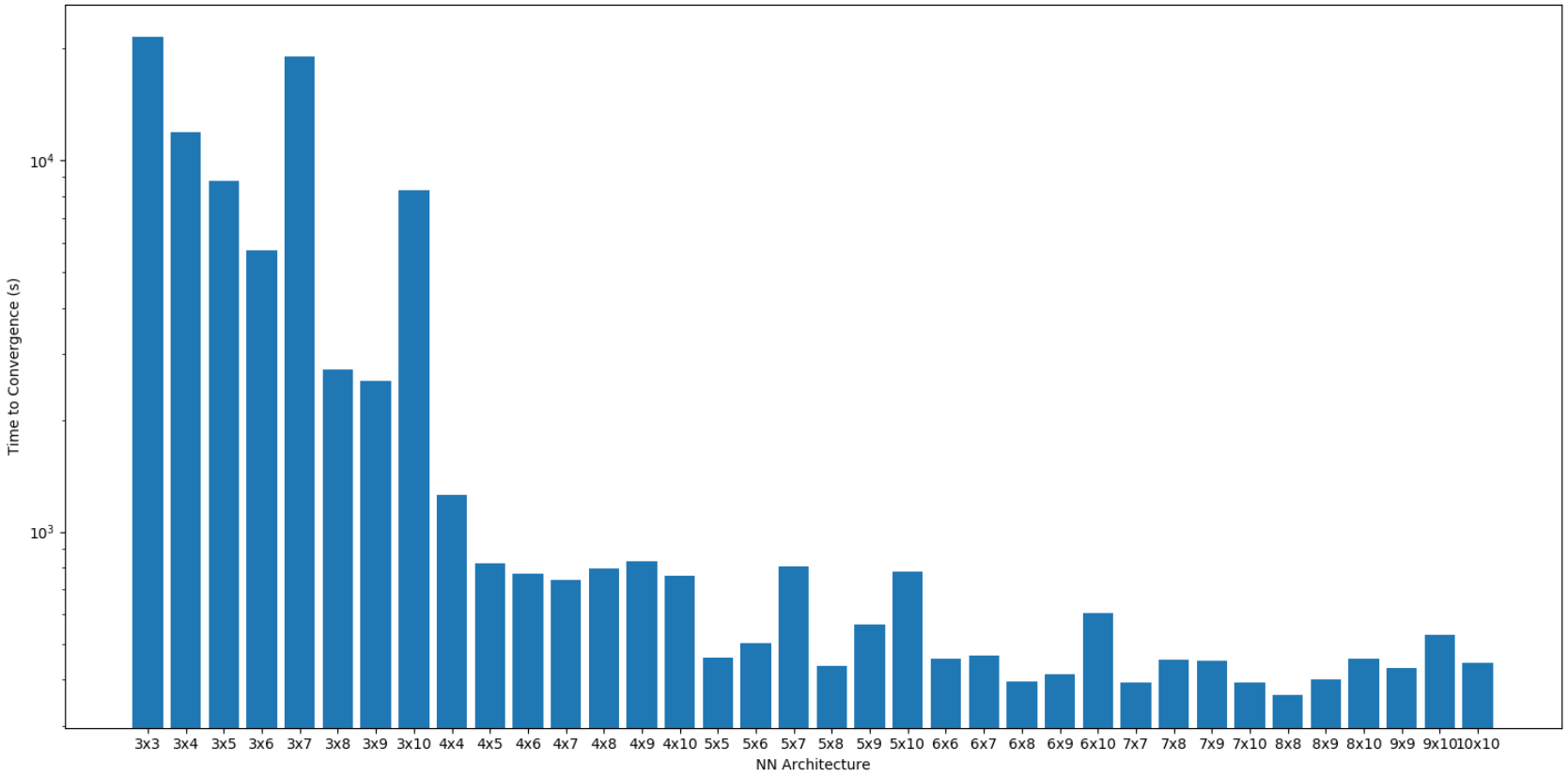

Figure A.3. Convergence time for different 2-layer neural net architectures. All models were fit to within 0.5 eV/Åfor the force RMSE. Here, a 3×10 architecture is a neural net with 3 nodes in the first hidden layer and 10 nodes in the second hidden layer.

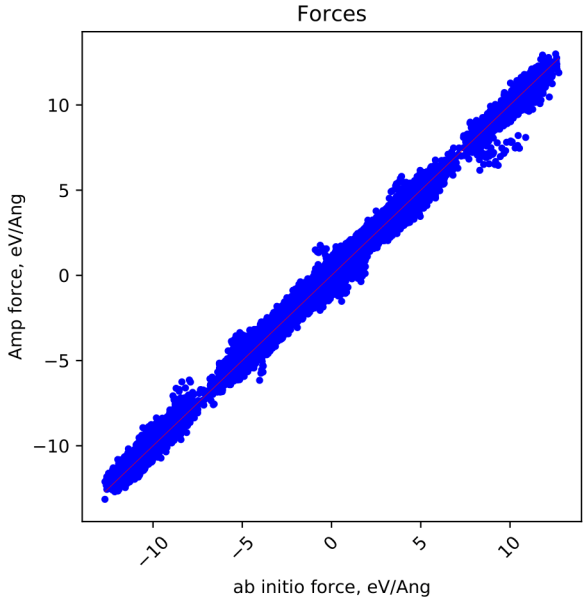

Figure A.4. The force RMSE of the ML model compared to VASP. An 8x8 architecture with a Gaussian descriptor in which η values were double the defaults.

0.34159 eV/Å. This model was used to produce the INS spectrum seen in the main paper.

A.5 MD

In a previous publication, a method for computing an INS spectrum from an MD trajectory was described. This method was developed to be theoretically equivalent to the finite displacement supercell method paired with OCLIMAX. This study extends that discussion by examining the effect of forcefield fitting on predicted INS spectra.

The initial forcefield was taken from the automated topology builder (ATb). It was based on a modified GROMOS 54A7 forcefield for gromacs. The .pdb file was also taken from ATb. In order to transform the molecule in a vacuum into a periodic crystal, a periodic .cif file from the Cambridge Crystallographic Data Centre was employed. ASE was used to place the single molecule inside the crystal lattice. The single molecule was then translated and rotated until it matched the lattice molecule as closely as possible. This was repeated for each molecule in the unit cell. Once these positions were determined, the molecules needed to be untwisted. The molecule as downloaded from ATb was twisted around its backbone (Figure A.5a), but crystalline rubrene (Figure A.5b is not. Next, a

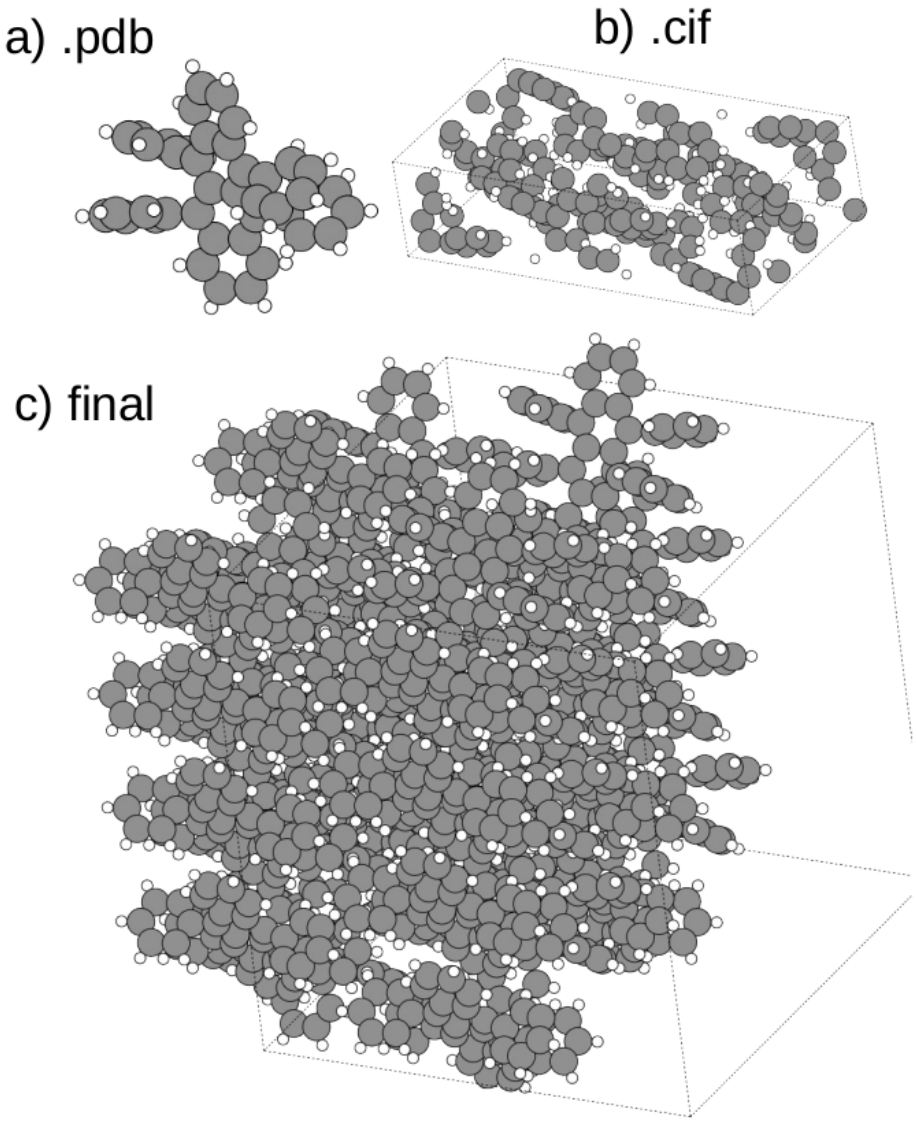

Figure A.5. Atomic structures of rubrene. a shows the structure from the .pdb file. B shows the structure from a .cif file and c shows the final structure after transforming a to look like b, creating a supercell, and performing a simulated annealing run.

4x2x1 supercell was made and simulated annealing was performed. The final structure is shown in Figure A.5c.

After creating the supercell, the system was equilibrated to 10 Kelvin. Then an NVT training MD simulation was performed in gromacs. The training run was 500ps and the positions were extracted every 0.5ps which generated 1000 configurations. VASP was then used to calculate the forces and energies at each configuration. Then forcebalance was

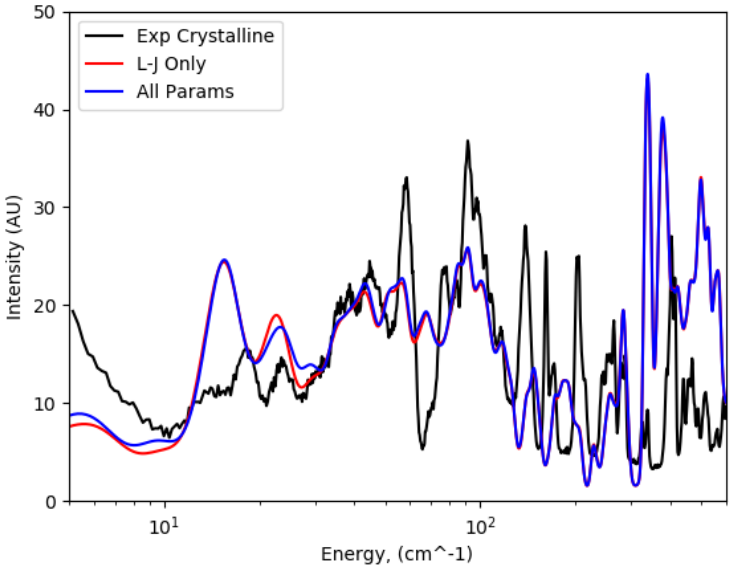

Figure A.6. Effect of trained parameters on INS spectrum. L-J Only indicates that only the Lennard-Jones parameters were trained and All Params means that every coefficient in the forcefield was allowed to change (various k values along with σ and ϵ in the main paper). A log scale is used because differences are subtle on a linear scale.

used to improve the forcefield. A number of different training sessions were performed in which different parameters were allowed to change. Allowing all bonds, angles, dihedrals, and Lennard-Jones parameters to change yielded a similar result as just allowing the Lennard-Jones parameters to change (Figure A.6. Thus, a forcefield with only improved Lennard-Jones parameters was used.

After the best forcefield was produced, the box effect of the box size was also investigated. Figure A.7 shows how the supercell size affected the final INS spectrum. Supercells up to 4x16x8 were used to compute an INS spectrum. Larger supercells were not investigated due to computational limitations. The results show that a larger simulation size produces more accurate results and supercell size is important in these types of simulations.

Finally, the velocity autocorrelation method was compared to the finite displacement supercell method. Figure A.8 shows the INS spectra computed using each method. The two spectra are largely similar with the primary difference in the low energy region. This is likely because a small box size was required for the finite displacement method while a

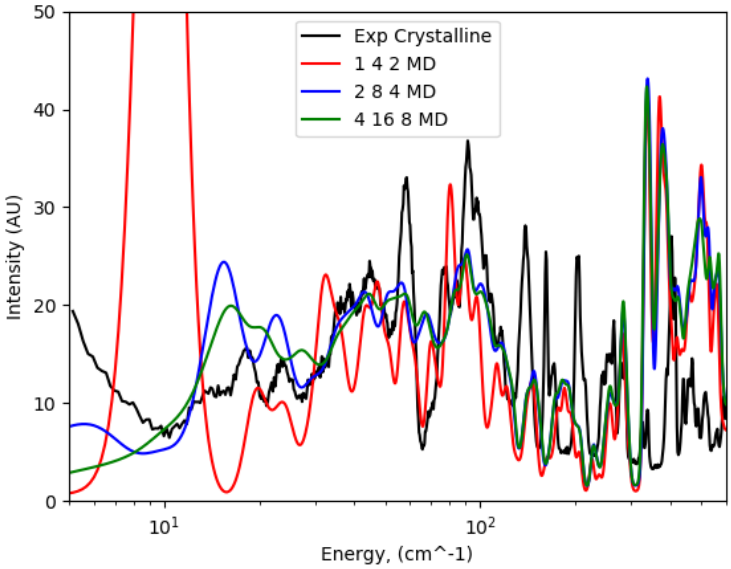

Figure A.7. Effect of the production run's box size on the final INS spectrum. 1 4 2 MD means that a $1 \times 4 \times 2$ supercell was used, 2 8 4 MD indicates that a $2 \times 8 \times 4$ supercell was used, and 4 16 8 MD indicates that a $4 \times 16 \times 8$ supercell was used. A log scale is used for the x-axis because the majority of the differences are at low energies.

larger box was used for the velocity autocorrelation method.

A.6 Times

The CPU times required to produce the spectra shown in Figure 3 of the main article are shown in Figure A.9. For MD and DFTB/ChIMES times including training and without training are shown. This is because these methods should be transferrable to other systems. The time without training is not shown for ML because it is not known how well a neural net potential trained on one system would perform with a different system. The color indicates the supercell size used to compute the spectra in Figure 3 of the main article.

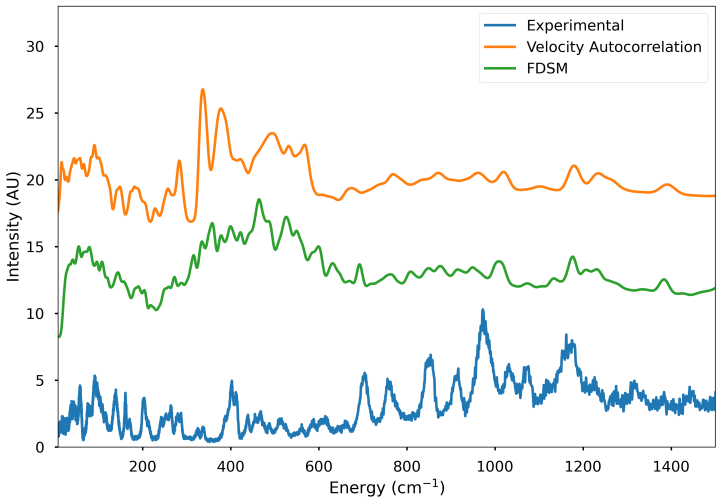

Figure A.8. The INS spectrum computed using the finite displacement supercell method (green) compared to the INS spectrum computed using the velocity autocorrelation method (orange) and the experimental INS spectrum (blue).

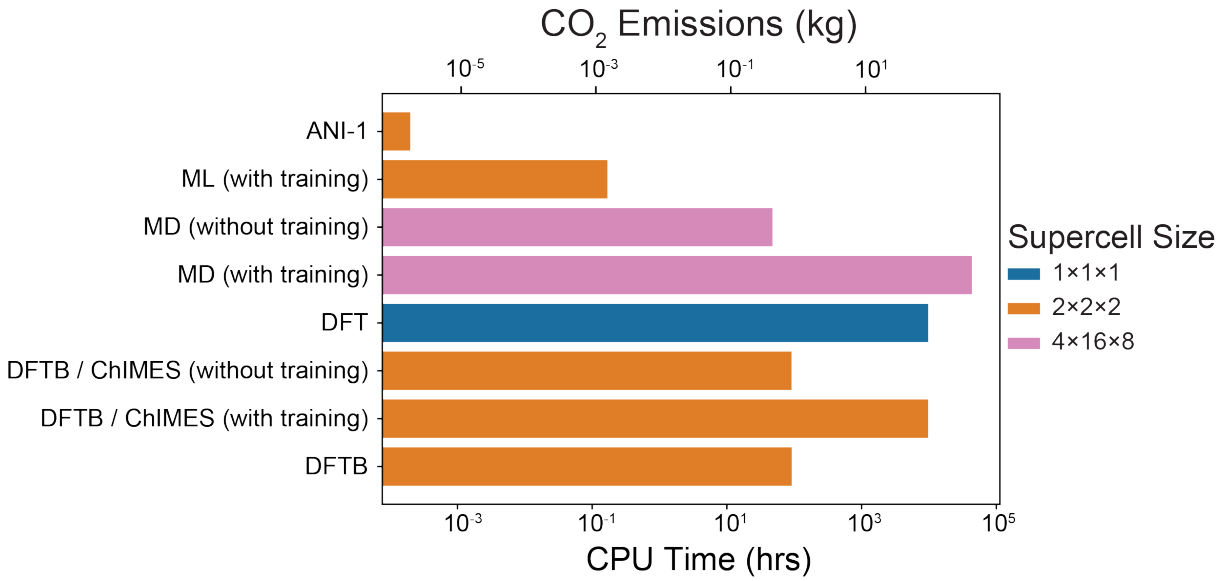

Figure A.9. The times and estimated CO_2 emissions for each method. These times correspond to the best spectrum produced by each method. These spectra are the ones plotted in figure 3 of the main article. The supercell sizes used for each calculation are indicated by color. For MD and DFTB/ChIMES, times are shown both with and without training.

Appendix B

SI for Elucidating Correlated Defects in Metal Organic Frameworks Using Theory-Guided Inelastic Neutron Scattering Spectroscopy

B.0.1 Sample preparation

Synthesis of UiO-66 with Modulators. $ZrCl_4$ (0.120 g, 0.515 mmol) and the modulators (1.00 mL acetic acid (AA) or 1.18 mL trifluoroacetic acid (TFA)) were dissolved in 20 mL of DMF in an 8-dram vial using ultrasound for 5 min. The mol ratio of modulators to Zr were both 30. 0.086 g of the linker precursor (benzene-1,4-dicarboxylic acid or a functionalized BDC linker precursor) was then added to the solution and dissolved by ultrasound for 15 min. The vials were kept under static conditions in a preheated oven at 393 K for 24 h. MOF precipitates formed, and they were isolated by centrifugation after cooling to room temperature. The solids were washed with DMF (30 mL) three times in a day to remove unreacted precursors and with acetone (30 mL) six times in 2 days to remove DMF. Then, the powder was dried at room temperature and activated at 393 K under vacuum for 18 h prior to characterization.

B.0.2 INS experiment details

The neutron vibrational spectra were collected at the VISION beam line (Spallation Neutron Source, Oak Ridge National Laboratory). VISION is an inverted geometry spectrometer with a resolution of 1-1.5% over the -2 ¡ E ¡ 1000 meV dynamic range. It measures neutron incident energy with the time-of-flight method. The final neutron energy is fixed and selected by Bragg reflection on a series of curved, pyrolytic graphite analyzers. The samples were placed in cylindrical vanadium sample holders (8 mm diam. x 50 mm height). The samples were inserted in a top-loading, closed-cycle refrigerator and cooled to 5 K before data collection. It took approximately 2 hours to collect each spectrum. An empty sample holder was also measured, and the corresponding signal was subtracted from all the data sets to remove beam-related background associated with scattering from aluminum windows, heat shield, vacuum shroud, and sample holder. Slits were used to reduce the beam size to illuminate only the sample during the experiment.

B.0.3 INS simulation details

All the simulations were accomplished using the Vienna Ab initio Simulation Package (VASP) with projector augmented-wave pseudo-potentials [1, 2] and the Perdew-Burke-Ernzerhof (PBE) density functional [3] with DFT-D3 vdW corrections [4]. The atomic positions and lattice parameters were optimized considering a energy cutoff of 520 meV and force criteria of 0.01 eV/Å. In order to calculate the phonon modes, the supercell displacement method was used with a simulation box of the same size as the original and forces being calculated at the gamma point. Finally, oclimax [5] used the phonon modes with a q-point sampling of 8 x 8 x 8 to calculate the INS spectrum.

B.0.4 INS comparison to optical spectroscopy methods

In a simple example, we demonstrate the advantages of INS over optical spectroscopy methods with a organic electronic material (TIPS-PN) as the studied system. In Fig. B.1, INS demonstrates a much wider energy spectrum compared to RAMAN and FTIR. Furthermore, since INS can sample the complete Brillouin zone, it presents a much higher density of peaks in the whole spectrum.

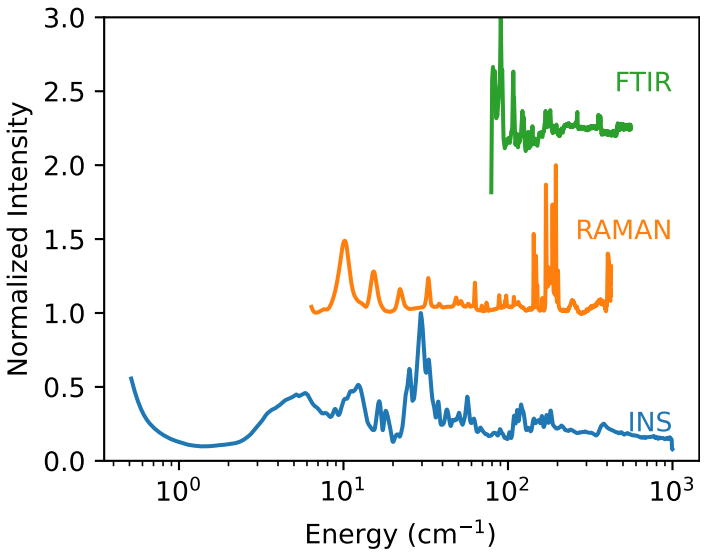

Figure B.1. Spectra comparison between INS, RAMAN and FTIR for organic electronic material (TIPS-PN). The energy axis in the log scale demonstrates the much broader energy range accomplished with INS, besides the much higher density of peaks in the whole spectrum.

B.0.5 Combined simulation and experiment approach

The overall approach for fingerprinting defects in the UiO-66 MOF with theory-guided Inelastic Neutron Scattering (INS) experiments is given in Fig. B.2. The flowchart shows the iterative method of simulating INS of a structure taken from a library of possible defect structures. Depending on the agreement with the experiment, another simulation can be done with a different configuration of defects. The library of defects was constructed considering possible connectivity defects (missing linkers and missing nodes) and/or possible chemical defects derived from the synthesis process (node ligands such as formates and acetates).

B.0.6 FCU simulation

The detailed comparison between experimental INS from the UiO-66-AA sample and simulation of the fcu model up to 5000 cm^{-1} is given in Fig. B.4

B.0.7 Correlation

In order to quantitatively characterize the degree to which each simulation agrees with the experiment, a correlation-based analysis method was employed. An experimental INS

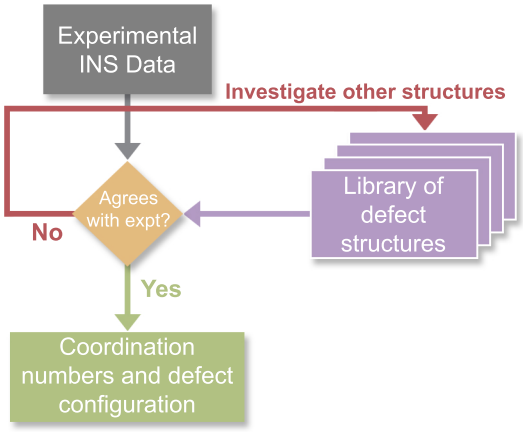

Figure B.2. Flowchart summarizing overall approach to predict INS from a library of candidate defect structures to be compared with the experimental measurements.

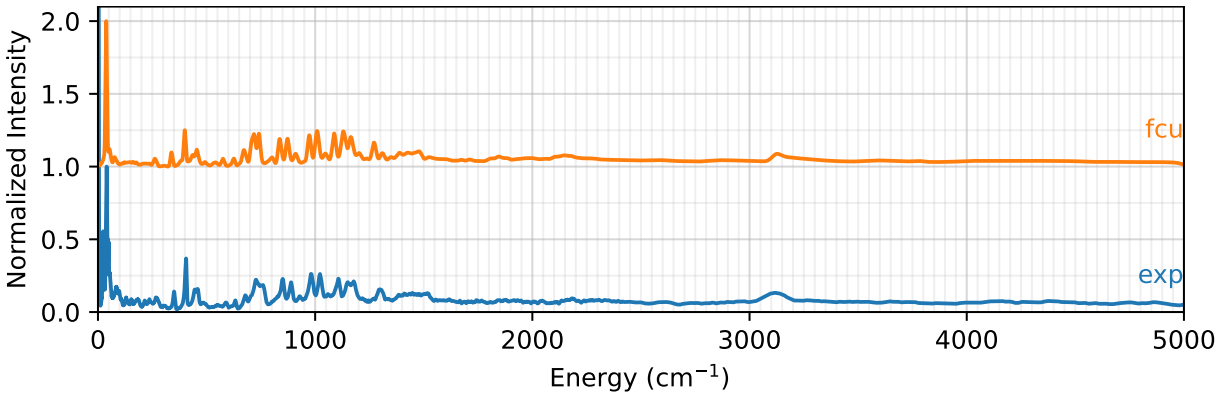

Figure B.3. INS spectra up to 5000 cm^{-1} for simulated fcu topology (orange) in comparison to experiment modulated with CH_3 (blue).

spectrum from the VISION spectrometer contains a higher density of points in the low energy and a lower density of points in the high energy. In contrast, a simulated spectrum contains equally spaced points across all energies. To account for this difference, the experimental spectrum is down-sampled by finding the nearest experimental point in energy to the regularly-spaced simulated spectrum. This process does not meaningfully change the experimental spectrum. Next, the correlation is computed between each simulated spectrum and the experimental spectrum. Correlation is used because it captures similarity in a way that accounts for peak shifts in energy and intensity unlike simple subtraction. The correlation coefficient is defined by

$$r = \frac{n\left(\sum(I_{exp}I_{sim})\right) - \left(\sum I_{exp}\right)\left(\sum I_{sim}\right)}{\sqrt{\left[n\left(\sum I_{exp}^2\right) - \left(\sum I_{exp}\right)^2\right]\left[n\left(\sum I_{sim}^2\right) - \left(\sum I_{sim}\right)^2\right]}} \tag{B.1}$$

where r is the correlation coefficient, n is the number of points, I_{exp} are the intensities of each experimental point, and I_{sim} are the intensities of each simulated point.

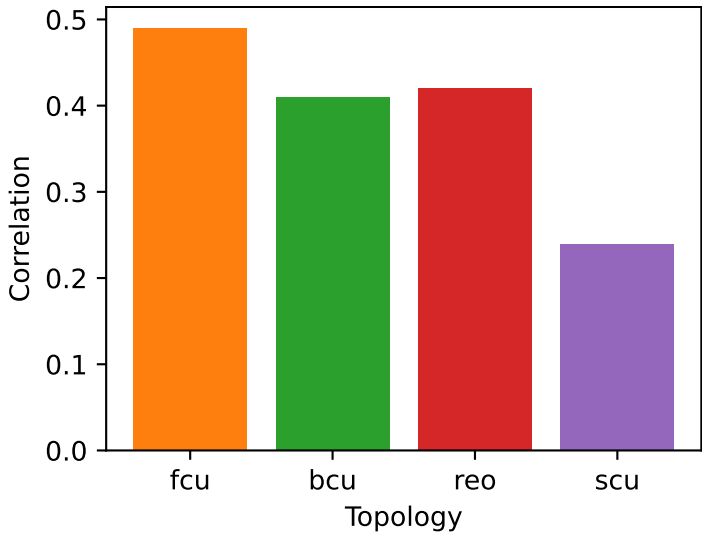

Figure B.4. Correlation between the INS experimental spectrum and the DFT simulated spectra produced by each topology.

B.0.8 Analysis of the formate contribution to the INS spectra

Incoherent INS obeys the following scattering law, which is a response function of the vibrational modes due to a transferred momentum from the neutron ($\mathbf{Q}$) at a frequency (ω) [5]:

$$\begin{aligned} S_{inc\pm1}(\mathbf{Q},\omega) = \sum_d \frac{1}{2M_d}\left\{\overline{b_d^2} - (\overline{b_d})^2\right\}\exp(-2W_d) \\ \times\frac{|(\mathbf{Q}\cdot\mathbf{e}_{ds})|^2}{\omega_s}\left(n_s + \frac{1}{2} \pm \frac{1}{2}\right)\delta(\omega \mp \omega_s), \end{aligned} \tag{B.2}$$

where ω_s is the frequency of the phonon mode s, $\mathbf{e}_{ds}$ is the polarization vector, $\overline{b_d}$, M_d, and W_d are respectively the neutron scattering length, the atomic mass, and the Debye-Waller factor. We call $\overline{b_d^2} - (\overline{b_d})^2$ as the incoherent cross-section. Therefore, the INS is given by the sum over all the atomic contributions.

In order to determine the origin of the peaks around 250 cm^{-1} and 1350 cm^{-1} of Fig. 1 of the main text, we can isolate the formate contributions to INS from all the other modes. This is possible by setting the atomic cross-section of the formate atoms to zero (no formate contributions) when calculating the INS spectrum. This was done for the bcu (Fig. B.5), reo (Fig. B.6) and scu topologies (Fig. B.7). The figures show that the mentioned peaks only appear when the contributions of formate groups are considered. Furthermore, as we increase the number of formates going from bcu and reo (4 formates per node), to scu (4/8 formates/node) the peak intensities increase.

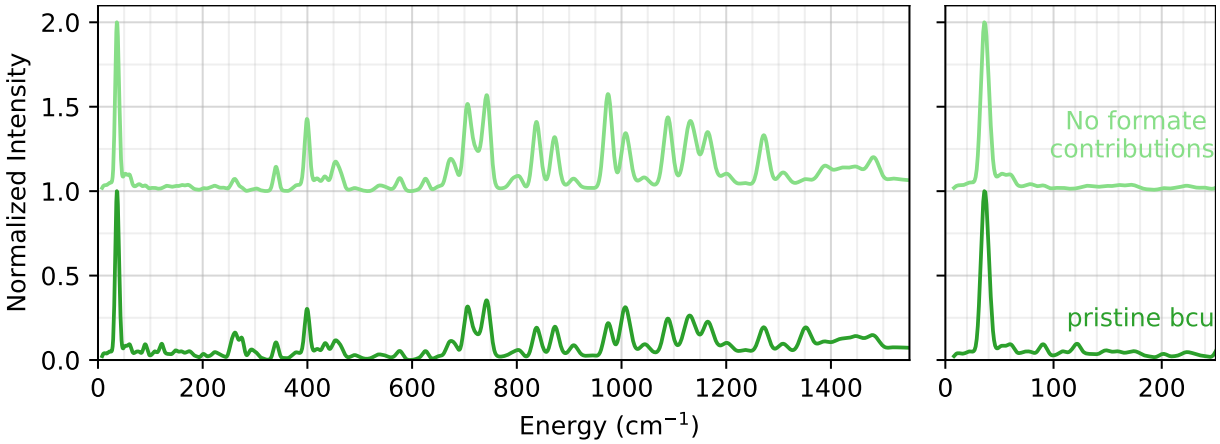

Figure B.5. INS spectrum comparison of the bcu MOF, where the defective sites are capped by formates, with (dark green) and without (light green) formate groups contributions.

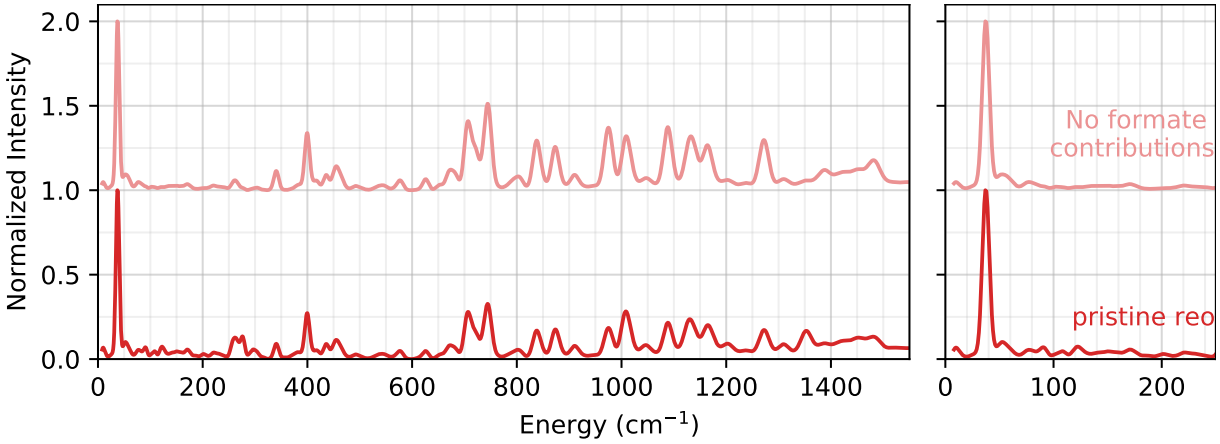

Figure B.6. INS spectrum comparison of the reo MOF, where the defective sites are capped by formates, with (dark red) and without (light red) formate groups contributions.

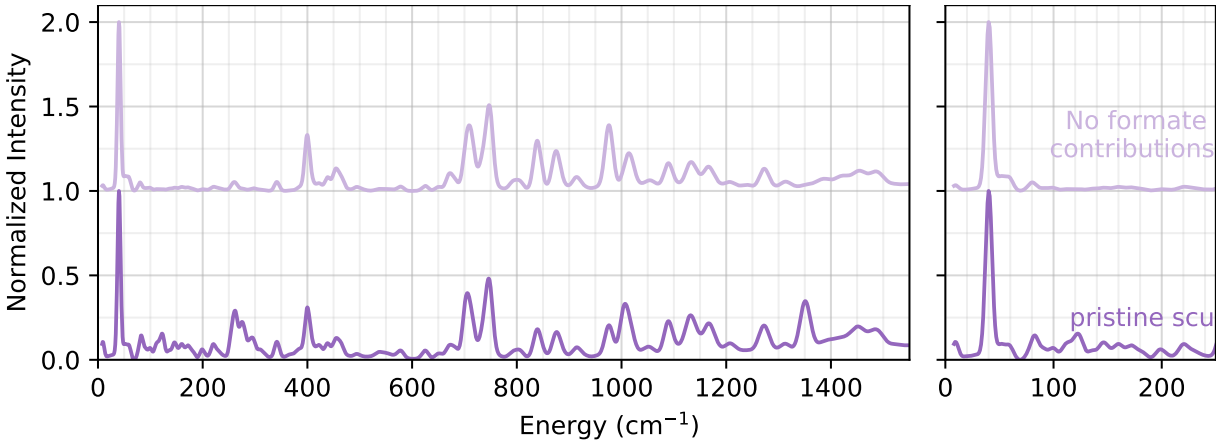

Figure B.7. INS spectrum comparison of the scu MOF, where the defective sites are capped by formates, with (dark purple) and without (light purple) formate groups contributions.

B.0.9 Mode analysis of peaks A, B, and C

The simulations of four different variations of the bcu defective topology present similar peaks in the fingerprint region to peaks A, B, and C of the experiment. The atomic motions related to the double peak a1 and a2 in the bcu topology where all defective sites are saturated with acetate groups is shown in Files *bcu-4A_a1.gif* and *bcu-4A_a2.gif*. In this case, each peak is related to the motions of one diagonal of defects. In Files *bcu-2A2F_a.gif* and *bcu-2A2F_b.gif*, the atomic motions related to peaks a and b are presented for the system that contains one diagonal of acetate groups and another with formate groups. In this case, the motions of peak a are isolated motions of acetate groups, while peak b is a combination of linkers and acetates groups in a "breathing" motion. Finally, Files *bcu-2A2F-2F2A_b1.gif*, *bcu-2A2F-2F2A_b2.gif* and *bcu-2A2F-2F2A_c.gif* describe the vibrations in the system with a unit cell containing two clusters where each is passivated with two different diagonals of acetates and formates groups. The doublet b (b1 and b2) is related to motions of neighbors acetates coupled to the framework. Furthermore, the motions derived from peak c involve all the acetates in the system coupled to the framework.

Appendix C

SI for Catching the Killer: Dynamic Disorder Design Rules for Small Molecule Organic Semiconductors

It is critical to compute the phonon modes across the entire Brillouin zone. Figure C.1 shows the variance of the transfer integral for BTBT both at a single q-point (red) and using a mesh throughout the Brillouin zone (black). While the single q-point modes are somewhat representative of the full mesh, it critically misses many features. For instance, the single q-point modes do not show any large contributions to σ^2 below 25 cm^{-1}, where many of the largest peaks lie in the full mesh. Conceptually, analyzing only a single q-point distorts how important each particular mode appears. At a different q-point, that mode may contribute signifcantly more or less to σ^2.

A spectral density type of mode analysis is more representative. Comparing the peaks in figure 4.3, it would appear that the low-energy modes are much more important than the high-energy modes. However, in figure 4.4, they appear to have similar importance. This is further explained in figure C.2. Here the same figure is zoomed into just a 2 cm^{-1} range for the largest peak and the peak around 1600 cm^{-1}. At this level of zoom, it is clear that although the low energy peaks are larger, the density of peaks is much larger for the 1600 cm^{-1}, but the higher energy peak is much denser. This indicates that the higher energy peak is more stable in energy across the Brillouin zone and that it has a

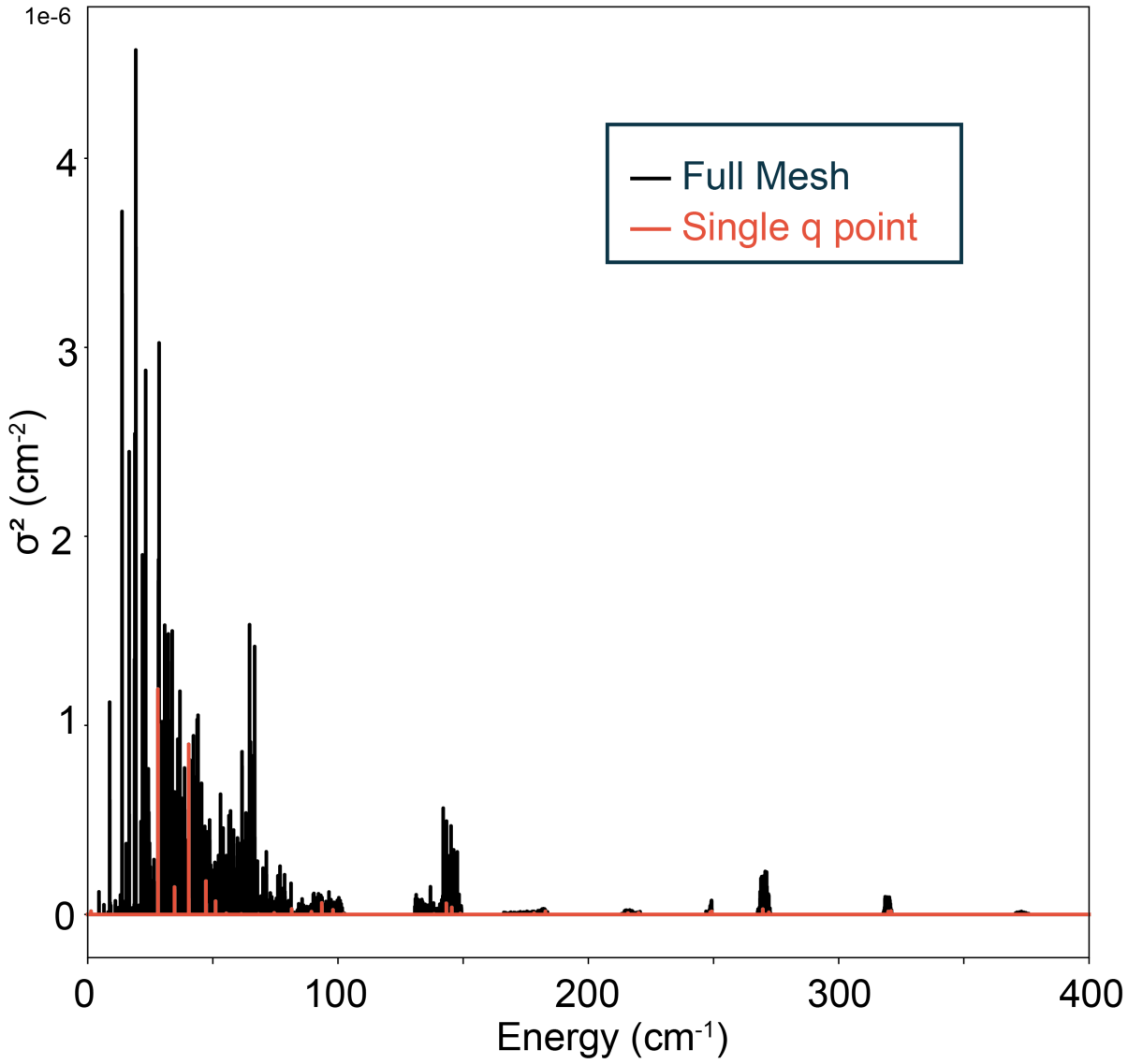

Figure C.1. The mode-wise variance of the transfer integral using a mesh over the full brillouin zone (Black) and at a single q-point (red) for BTBT.

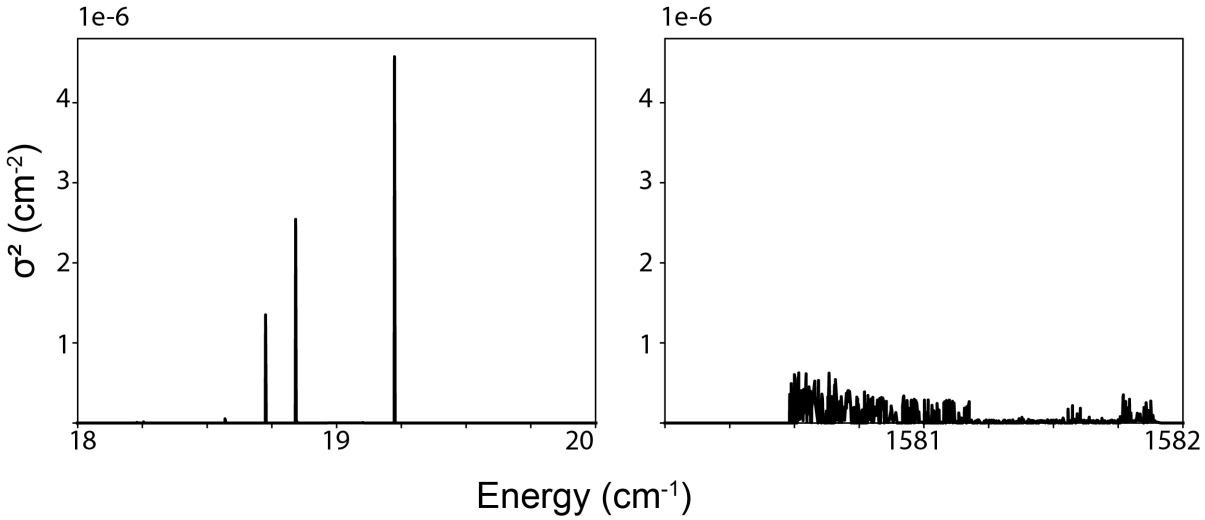

Figure C.2. A version of figure 4.3a zoomed in on the largest peak in the low energy and the peak around 1600 cm^{-1} for BTBT.

moderate impact across that zone. In contrast, the low energy peak varies in energy and intensity across the Brillouin zone. This further reinforces the importance of exploring the full Brillouin zone rather than just the gamma point.